Blending of powders for in-situ alloying of Ti-6Al-4V laser powder bed fusion

by
Benjamin Stuart Parker

Thesis presented in partial fulfilment of the requirements for the degree of Master of Engineering (Mechanical) in the Faculty of Engineering at Stellenbosch University

Supervisor: Prof. Deborah Blaine

March 2021

Declaration

By submitting this thesis electronically, I declare that the entirety of the work contained therein is my own, original work, that I am the sole author thereof (save to the extent explicitly otherwise stated), that reproduction and publication thereof by Stellenbosch University will not infringe any third party rights and that I have not previously in its entirety or in part submitted it for obtaining any qualification.

Date: March 2021

Abstract

Novel powder blending techniques for Ti-6Al-4V powder mixtures, using master-alloy (MA) and blended elemental (BE) powders as opposed to the industry standard of pre-alloyed (PA) Ti-6Al-4V powder, have been developed for laser powder bed fusion (LPBF), in particular direct metal laser sintering® (DMLS®). The quality of a LPBF component is a result of both the metal powder characteristics and the LPBF process parameters. This study is limited to the metal powder characterisation of such blends, focussing on typical powder characterisation metrics of morphology, particle size distribution (PSD), flowability, apparent and skeletal density, and the angle of repose (AoR). A relatively novel metric of spreadability is a key focus in this study as it directly represents the mechanics of the LPBF recoating process. A spreadability test rig was commissioned in this work and obtained spreadability metrics of percent coverage and spread density. Moisture accumulation on stored metal powders has an adverse effect on flowability and spreadability of metal powders and was shown to significantly improve through air drying. It was found that MA or BE powder blends have spreadability characteristics similar to PA Ti-6Al-4V, with the standard metrics of particle morphology, PSD, flowability, and AoR having the most significant correlation to spreadability. This indicates that powders that: are more spherical, have a narrow PSD span, are highly flowable, and have a low AoR, have a better spreadability.

Uittreksel

Nuwe poeiermengingstegnieke vir Ti-6Al-4V poeiermengsels, met behulp van meesterlegering (MA) en gemengde elementêre (BE) poeiers, in teenstelling met die industriestandaard van voorgelegeerde (PA) Ti-6Al-4V poeier, is ontwikkel vir laser poeier bed samesmelting (LPBF), in die besonder direkte metaal laser sintering® (DMLS®). Die kwaliteit van 'n LPBF-komponent is die gevolg van beide die metaalpoeier-eienskappe en die LPBF-prosesparameters. Hierdie studie is beperk tot die metaalpoeierkarakterisering van sulke mengsels, wat fokus op tipiese poeierkarakteriseringsmetrieke van morfologie, partikelgrootteverdeling (PSD), vloeibaarheid, effektiewe en geraamtedigtheid, en die hoek van rus (AoR). 'n Maatstaf van verspreidbaarheid, wat relatief nuut is, is 'n kernfokus in hierdie studie, aangesien dit die meganika van die LPBF-verspreidingsproses direk beïnvloed. 'n Verspreidbaarheidstoets is in hierdie werk in diens gestel en het verspreidingsstatistieke van persentasie verspreiding en verspreidingsdigtheid verkry. Vogakkumulasie op gestoorde metaalpoeiers het 'n nadelige uitwerking op die vloeibaarheid en verspreidbaarheid van metaalpoeiers, en dit blyk dat dit aansienlik verbeter deur lugdroging. Daar is gevind dat MA- of BE-poeiermengsels verspreidbaarheidseienskappe het soortgelyk aan PA Ti-6Al-4V, met die standaardmeters van partikel-morfologie, PSD, vloeibaarheid en AoR, wat die belangrikste korrelasie met verspreidbaarheid het. Dit dui daarop dat poeiers wat: meer sferies is, 'n smal PSD-span het, baie vloeibaar is en 'n lae AoR het, 'n beter verspreidbaarheid het.

Acknowledgements

I would like to show my appreciation to everyone who has been a part of this thesis. To Professor Deborah Blaine for her supervision and guidance throughout the project, to Mr Preyin Govender and Mr Gerrit ter Haar for their consultation and direct assistance with lab work, to Mr Ferdi Zietsman and his team for their timeless work on my designs, and to my friends and family who encouraged me and facilitated well needed coffee breaks.

I would also like to thank the CUT team: Mr Lekhetho Ramosena, and his supervisors, Dr Thywill Dzogbewu, and Professor Willie du Preez, for their combined effort on this project, as well as Mr Dean-Paul Kouprianoff and the CRPM for supplying the recoater blade used in the spreadability test rig.

I would lastly like to thank The Boeing Company for supplying the metal powders through the National Aerospace Centre at the University of Witwatersrand.

Table of Contents

List of Figures

Page

List of Tables

Page

Nomenclature

A	Area
AD	Apparent density
Al	Aluminium
AM	Additive manufacturing
AoR	Angle of repose
BCC	Body centred cubic
BE	Blended elemental
CAF	Central Analytical Facilities
CIF	Crystallographic information file
CP	Commercially pure
CUT	Central University of Technology
CRPM	Centre for Rapid Prototyping and Manufacturing
DED	Directed energy deposition
DEM	Discrete Element Method
DMLS®	Direct metal laser sintering®
DPI	Dots per inch
EB	Electron beam
EDS	Energy-dispersive spectroscopy
ELI	Extra low interstitial
FCC	Face centred cubic
FDM	Fused deposition modelling
FESEM	Field emission scanning electron microscope
FR	Flow rate
FR_C	Carney flow rate
FR_H	Hall flow rate
h	Height
H	Hydrogen
HCP	Hexagonal close packed
HDH	Hydride-dehydride

HIP	Hot isostatic pressing
ICP-OES	Inductively Coupled Plasma - Optical Emission Spectrometry
LLS	Laser light scanner
LPBF	Laser powder bed fusion
m	Mass
MA	Master-alloy
MAM	Metal Additive Manufacturing
MIM	Metal injection moulding
MSDS	Medical safety datasheet
NAC	National Aerospace Centre
NECSA	Nuclear Energy Corporation of South Africa
O	Oxygen
OM	Optical microscope
ρ	Density
PA	Pre-alloyed
PBF	Powder bed fusion
PCB	Printed circuit board
PM	Powder metallurgy
PSD	Particle size distribution
PSU	Power supply unit
r	Radius
SEM	Scanning electron microscope
SU	Stellenbosch University
t	Thickness
Ti	Titanium
V	Volume
V	Vanadium
WDS	Wavelength-dispersive spectroscopy
XCT	X-ray computed tomography
XRD	X-ray Diffraction

1 Introduction

This project involves blending different combinations of titanium, aluminium, vanadium and Al-V master-alloy (MA) powders for *in-situ* alloying of Ti-6Al-4V for metal additive manufacturing (MAM), in particular laser powder bed fusion (LPBF). This thesis is in partial fulfilment of the author's master's degree in Mechanical Engineering through Stellenbosch University (SU). This thesis: introduces the topic and identifies the objectives, motivation and scope of the research; reviews current and relevant literature; outlines the research methodology followed; presents and provides a discussion of the results; presents a techno-economic analysis; and provides conclusions and recommendations for future work.

1.1 Background

Titanium alloys have proven to be greatly advantageous in structural engineering due to their high strength to weight ratio, good corrosion resistance, and biocompatibility [1]–[3]. Additive manufacturing (AM) of titanium alloys allows for near-net manufacturing, which significantly reduces material wastage as opposed to standard subtractive manufacturing techniques [4], [5].

LPBF, specifically direct metal laser sintering® (DMLS®) is a MAM technique used to produce three-dimensional components layer-by-layer, through melting powdered metal with a high-power laser. This technique allows for the fabrication of highly complex components with very little post processing required. This is particularly advantageous in the aerospace and biomedical industries, where expensive alloys, such as Ti-6Al-4V, are widely used.

The quality of the DMLS® build is highly dependent on both the characteristics of the metal powder as well as the DMLS® process parameters. Extensive research has been conducted on the effects of the critical powder characteristics [5]–[7] and the DMLS® process parameters, such as laser power, scan speed, and hatch distance [1], [8]–[10]. These studies showcase how the powder characteristics and DMLS® process parameters affect the material and mechanical properties of the final component [1], [9]–[13]. The majority of research in this field has focussed on pre-alloyed (PA) powders with only a few studies investigating the use of MA or elemental powder blends in LPBF [14]–[16].

This thesis aims to provide insight into an alternative powder blending technique, that will allow for customized alloy development and potentially reduce the

overall cost of DMLS® Ti-6AL-4V production by providing framework for blending of powder mixtures for *in-situ* alloying in LPBF. This method makes use of MA and elemental powder blends of Ti-6Al-4V for direct use in DMLS®, as opposed to typical PA powders.

1.2 Aim

The aim of this research is to develop a technically and economically feasible powder blend of Ti-6Al-4V for *in-situ* alloying with DMLS®. The suitability of the powder blend is assessed in terms of its powder characteristics.

1.3 Hypothesis

It is hypothesized that MA and elemental powder blends of Ti-6Al-4V can be utilised for *in-situ* alloying in DMLS®, with powder blend characteristics comparable to the industry standard of PA Ti-6Al-4V powder.

1.4 Objectives

The objectives of the project are as follows:

1. To characterise as-received powders in terms of their chemical and physical properties.
2. To design, characterise, and evaluate two powder blends.
3. To conduct a techno-economic analysis on the suitability of powder blending in LPBF.

1.5 Motivation

Titanium alloys, particularly Ti-6Al-4V, have proven useful in the biomedical and aerospace industries, due to their biocompatibility, high strength to weight ratio, and corrosion resistance. DMLS® allows for complex geometry to be manufactured along with minimal material wastage as opposed to subtractive manufacturing. However, the cost of producing DMLS® Ti-6Al-4V traditionally, using PA Ti-6Al-4V, is significantly more expensive than its wrought counterpart. Producing DMLS® Ti-6Al-4V using MA or elemental powder blending is a potential way to reduce the cost of DMLS® Ti-6Al-4V fabrication as well as providing the framework for easily varied alloying compositions for future alloy development.

1.6 Scope and imitations

This project ran parallel to a complementary project through the Centre for Rapid Prototyping and Manufacturing (CRPM) at Central University of Technology (CUT), Free State. The metal powers were supplied by Boeing through the National Aerospace Centre (NAC) at the University of Witwatersrand. The combined research project focussed on the feasibility of MA and elemental powder blending for DMLS® of Ti-6AL-4V. The Ti-6Al-4V powder blends were designed, mixed, and characterised at SU and the powder blends were sent to CUT to evaluate their performance in AM. The focus of this study was on the Ti-6Al-4V grade 5 alloy as the development of the project specification originated from the aerospace industry.

This study focussed on: the characterisation of raw powders; powder blending; characterisation of the powder blends; and conducting a techno-economic analysis on the suitability of this technology in LPBF. LPBF was selected as in-situ alloying has not yet been adequately established using this technology and LPBF technology is readily accessible in South Africa. In contrast, DED is inaccessible to the research groups involved in this project. Additionally, a novel spreadability device was designed, built, and used to evaluate the powder blends. The CUT project focussed on producing and characterising single tracks and single layers and the ideal process parameters of the blend were determined. The optimised process parameters were then used to produce small parts and determine their microstructural and mechanical properties.

All builds were performed at CRPM on their EOSINT M280, and the results do not form part of the scope of this study and have therefore been omitted. To observe the initial results of the combined study, please refer to the RAPDASA 2019 collaborative paper [16]. Due to limited access to efficient oxygen analysis in South Africa, this parameter was largely excluded from this study.

1.7 Thesis Outline

The overall outline of this thesis is provided in this section. In Section 2 the relevant literature covering the work of this study is presented. This includes the topics of metal powder production; powder metallurgy (PM); AM, specifically, LPBF of the Ti-6Al-4V alloy; powder blending; powder and material characterisation techniques; and the powder characterisation technique of spreadability.

Section 3 demonstrates the methodology followed throughout the project. This includes all experimental procedures and equipment used. Section 4 presents the results of the project and provides a discussion on their significance. Section 5 provides a techno-economic analysis of the work and its relevance in industry. Section 6 concludes the work, identifies whether the objectives were met and makes recommendations for future work. Where possible the overall structure of each section was kept consistent for simplicity.

2 Literature Review

The following literature that is of significance to this project has been reviewed in this section. The topics of importance are: metal powder production; PM; powder and material characterisation techniques; AM for DMLS® of Ti-6Al-4V, in particular elemental powder blending; and the powder characterisation technique of spreadability.

2.1 Metal Powder Production

PM is the study of producing materials or components from fine metal powders rather than classical ingot metallurgy. Conventional ingot metallurgy includes melting metal in a furnace and casting the molten metal into ingots, which can be worked and machined by traditional forming and subtractive manufacturing techniques.

Metal powders are used in AM methods and are typically produced using various atomisation processes. These processes include gas, water and plasma atomisation. Other processes include the hydride-dehydride (HDH) and the aluminothermic reduction process. Each method has advantages and disadvantages in terms of cost, time, particle size, shape, quality, and material suitability, which are key aspects to consider when purchasing powder for use in AM. An overview of these methods is presented in Table 1.

Table 1: Overview of metal powder production processes [6], [17], [18]

Process	Particle Shape	Particle Size Range (µm)	Common Materials	Cost (1=low)
Water atomisation	Irregular	0-500	Non-reactive	2
Gas atomisation	Spherical	0-500	Ti, Al, Ni, Fe, Co	3
Plasma atomisation	Highly spherical	0-200	Ti alloys	4
HDH	Irregular	45-500	Ti alloys	1
Aluminothermic Reduction	Irregular	0-500	Fe, Ti, V, Al, Al-alloys	1

2.1.1 Atomisation Processes

Water, gas and plasma atomisation processes have similar working principles to produce extremely fine metal powders, typically <100 µm. These methods consist

of three main stages: melting, atomisation, and solidification and cooling [19]. The key difference between the processes is the medium that atomises the powder.

The **water atomisation** technique, seen in Figure 1a, feeds molten metal through a nozzle into a chamber where it is met by high velocity jets of water which break up the molten metal and rapidly solidify the droplets into fine (typically <200 µm) powder particles. These powder particles are collected at the bottom of the chamber, and the water and powder are separated through various drying methods. This technique produces irregular shaped particles as the water immediately quenches and solidifies the molten droplets, before they are able to form spheres [20], [21] and is typically used to manufacture iron-based powders [19]. The powder particle size is affected by the water pressure, velocity, stream angle, and stream diameter as well as the molten metal density, viscosity and surface tension [19].

The **gas atomisation** process displayed in Figure 1b, is similar to that of water atomisation whereby molten metal is fed through a nozzle but is instead met by a number of high velocity gas nozzles. The jets of gas break up the molten metal and rapidly solidify the droplets into fine (typically <80 µm) powder particles [19]–[22]. The droplets remain molten for long enough to form spheres before they solidify, which is favourable in AM. Many metals have adverse reactions to certain gases which is why inert gases are favoured by this process. However, the process commonly leads to gas pore entrapment [17], [23], [24], which can contribute to an increase in the final part porosity.

The **plasma atomisation** technique illustrated in Figure 1c, feeds a spool of metal wire directly into the path of multiple plasma torches in a chamber. These torches immediately melt and atomise (break into droplets) the wire, after which the molten droplets form spheres before solidifying. The result is highly spherical powder particles that are collected at the bottom of the chamber [21], [22], [25], and this method is the most expensive of the three. Similarly, **plasma spheroidization** may be employed to convert irregular to highly spherical shaped powder particles [26], [27].

2.1.2 Hydride-Dehydride Process

The HDH process is typically used to produce metal fines from contaminated scrap titanium metal. The overview of the process is the following: scrap metal titanium is heated in a furnace with an H_2 controlled atmosphere; brittle TiH_2 forms that is

then milled to produce fine powder; the powder is then dehydrogenated by placing the powder at an elevated temperature , around 700 °C [28], [29], under high vacuum, converting the hydride powder back to titanium.

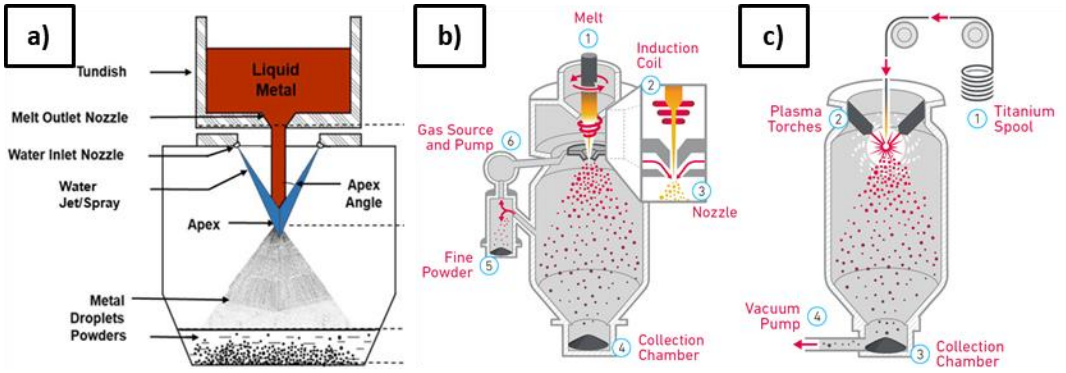

Figure 1: Metal powder production techniques of a) water atomisation [30], b) gas atomisation [25], and c) plasma atomisation [25]

2.1.3 Aluminothermic Reduction

The production of pure vanadium is difficult as it is easily contaminated by other elements [31]. The aluminothermic reduction can be employed and is a highly exothermic reaction given as [32]:

$$3V_2O_5 + 10\text{Al} \rightarrow 6\text{V} + 5Al_2O_3 \qquad (2.1).$$

The vanadium can be further refined by electron beam melting with the addition of aluminium to assist in the removal of oxygen [33]. To produce the aluminium-vanadium MA, excess Al is added to the reaction [34]. The Al ratio as well as the reaction temperature govern the formation of various intermetallics [35]. The aluminium-vanadium MA is ball milled and sieved to obtain the correct particle size.

2.2 Powder Metallurgy

PM involves fusing fine metal powders together again by a range of pressing, sintering and forming techniques [36]. PM offers the advantages of reduced cost and manufacturing complexity. Cost is primarily reduced by decreasing the number of machining steps required, while simultaneously reducing material wastage. An additional benefit is the ability to easily produce components with varying alloying compositions, especially of metals that have high melting points

[36]. The conventional PM processes include press-and-sinter, metal injection moulding (MIM), and hot isostatic pressing (HIP), and are briefly explained in the following subsections. The PM industry focus has, however, shifted to AM, covered in Section 2.3.

2.2.1 Press-and-Sinter

In the typical press-and-sinter approach, powdered metal is compacted using a uniaxial or isostatic compaction method to form a “green” dense compact. This compact is then sintered (particles chemically bonded together by thermally activated solid state diffusion) in a furnace with a controlled atmosphere [37].

2.2.2 Metal Injection Moulding

The MIM process involves combining fine metal powder with a binder (such as polymers and paraffin wax) to create a feedstock which is heated and injected into a die to form a “green” dense compact. The binder is then removed using various thermal processes and the component is sintered to high density (>95 % of wrought) in a furnace with a controlled atmosphere [19], [38]. The MIM process is capable of producing parts in large quantities, with complex geometries and with mechanical properties similar to its wrought counterpart.

2.2.3 Hot Isostatic Pressing

The HIP process involves subjecting a mould or component to high pressure and temperature using an inert gas. The process can be applied directly to an encapsulated powder, known as direct HIP, or to a cast or pre-sintered part, known as post-HIP [39]. The resulting components are extremely dense. HIP is frequently applied to sintered and AM components to eliminate residual porosity, especially for aerospace and biomedical applications [38].

2.3 Additive Manufacturing

AM is a process of manufacturing whereby components are built-up into near-net shape geometries as opposed to traditional subtractive methods. AM can be employed with polymer, ceramic and metal materials, however, will be limited to metal and, more specifically, Ti-6Al-4V for this study. Two main technologies have emerged in MAM. The first is powder bed fusion (PBF) and the second is directed energy deposition (DED).

PBF is a process where fine metal powder is spread over a flat build surface in a thin layer and precisely melted with a specific heat source. A fresh powder layer is then deposited on top of the first and precisely melted again, with this melted region fusing the previous layers melted region. This process is repeated in a layer-by-layer fashion until the component is completed [14], [40].

The heat source is specific to the machine, with either a high-powered laser beam or an electron beam being commonly used. The powder distribution method employs an assortment of blades and rollers, with various material and cross-sectional profiles, that spread the powder across the bed. The specific heat source and blade/roller combination largely boils down to each manufacturer's preference. Although the processes may be the same, due to certain intellectual property restrictions, a range of process names have been created and these are clarified in Section 2.3.1.

In the DED process, either powdered or solid wire feedstock is fed through a nozzle and melted by either an electron or high-powered laser beam. The principal movement of the machine is typically like that of a 5-axis milling machine with the deposition nozzle functioning similarly to a typical nozzle of a fused deposition modelling (FDM) polymer-based printer. The nozzle deposits molten metal which rapidly solidifies and is built up in a layer-by-layer fashion. It is important that in both the PBF and DED processes, the build environment is flooded with a non-reactive gas, creating a controlled process atmosphere to prevent oxidisation or explosive reactions of volatile metals, such as argon for titanium alloys.

An added benefit of some of the DED machines is their ability to feed different alloys into the main melting nozzle through several different material hoppers. This feature enables the direct use of in-situ alloying, which has been established by FormAlloy's Alloy Development Feeder [41]. Considering this technology has already been established in industry, the in-situ alloying of LPBF is still in its infancy and requires attention.

The main advantage of AM is the ability to create complex near-net shape geometries with reduced material wastage. Components can be created as single complex parts, as opposed to traditional methods of welding and riveting simpler parts [42] or subtractive machining a larger block, which leads to a decrease in fabrication time and an increase in material wastage [1].

2.3.1 Overview of MAM Technologies

Different MAM process names and associated leading manufacturers are summarised in Table 2. The table is limited to well-known process names and manufacturers. For the duration of the CUT study, all prints were produced using an EOSINT M280 machine. The scope of this project was therefore limited to the LPBF category, specifically DMLS®.

Table 2: Metal additive manufacturing processes and associated manufacturers

Metal Additive Manufacturing processes			
Powder Bed Fusion (PBF)		Directed Energy Deposition (DED)	
Laser PBF (LPBF)	Manufacturer/s	Laser Beam	Manufacturer/s
DMLS®[1]	EOS[2], Germany	LENS®[3]	Optomec, USA - NM
LaserCUSING® - DMLM[4]	Concept Laser, Germany	DMD®[5]	DM3D Technology, USA - MI
SLM®[6]	SLM Solutions, Germany	LMD[7]	Trumpf, Germany
LBM[8]	AddUp, France	DED[9]	BeAM, France
LMF[10]	1. Sisma, Italy 2. Trumpf, Germany	LDW[11]	DMG MORI, Japan
Laser melting	Renishaw, UK	DMP[12]	3D Systems, USA - SC
Electron Beam PBF (EB-PBF)	Manufacturer/s	Electron Beam	Manufacturer/s
EBM®[13]	Arcam, Sweden	EBAM®[14]	Sciaky, USA - IL

[1] Direct metal laser sintering; [2] Electro Optical Systems; [3] Laser-engineered net shaping; [4]Direct metal laser melting; [5] Direct metal deposition; [6] Selective laser melting; [7] Laser metal deposition; [8] Laser beam melting; [9] Directed energy deposition; [10] Laser metal fusion; [11] Laser deposition welding; [12] Direct metal printing; [13] Electron beam melting; [14] Electron beam AM

2.3.2 Ti-6Al-4V Additive Manufacturing

The Ti-6Al-4V alloy is highly sought-after in the aerospace, biomedical, automotive, and marine industries, due to its unique characteristics of high strength to weight ratio, good corrosion resistance, and biocompatibility [1]–[3]. Due to its high strength, low elastic modulus and low thermal conductivity, Ti-6Al-4V is a difficult alloy to machine which makes it undesirable for traditional subtractive manufacturing processes [1]. The two commonly used grades in the AM industry are Ti-6Al-4V (grade 5) and Ti-6Al-4V extra low interstitial (ELI) (grade

23). The grade 23 alloy has lower iron and oxygen content which leads to an improved ductility and fatigue life, with a reduced strength. The grade 23 alloy is primarily used for surgical implants in the biomedical industry [43], therefore the focus of this study was selected as the grade 5 alloy, as it is relevant to the aerospace industry.

2.4 Laser Powder Bed Fusion

A schematic of the LPBF process is illustrated in Figure 2. The specifics of the process vary between manufacturers, but the overall principle remains the same. Powder is spread, from a dispenser platform, using a recoater blade in a thin layer over a build platform and excess powder is collected in the collector bin. A high-powered laser or electron beam then selectively melts the first cross-sectional layer of the component. The build platform is then moved downwards, and another thin powder layer is spread over the build plate. This process is repeated until the component is complete [7].

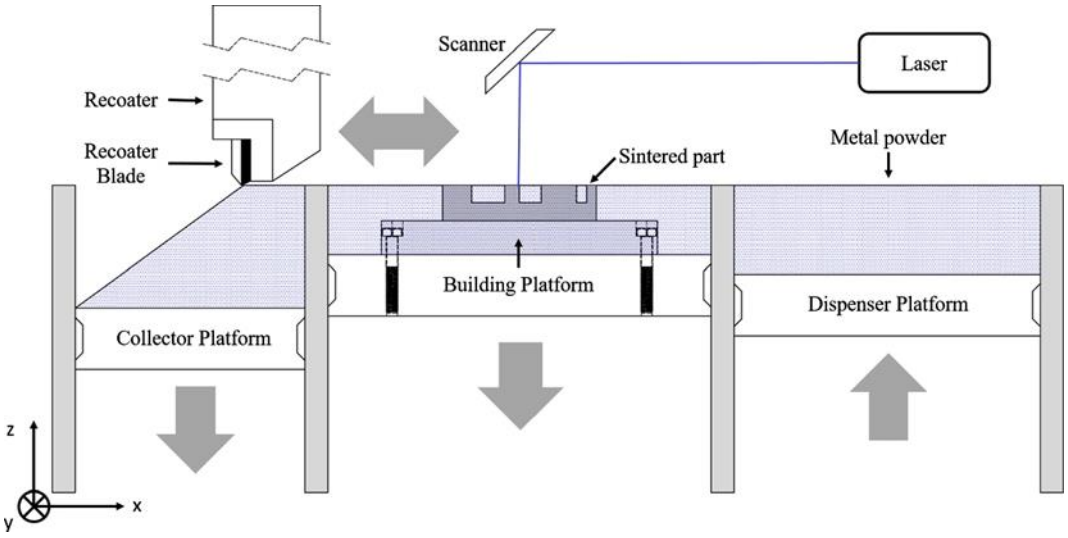

Figure 2: LPBF schematic [44]

2.4.1 Process Parameters

There are several process parameters in a LPBF printer which can be adjusted to improve the quality of the 3D printed component. The main parameters are scan velocity, laser power, layer thickness, and hatch spacing. These, among others have been illustrated in Figure 3. Numerous studies have investigated the effects of process parameters on the material and mechanical properties of the final

component. These include the effects on microstructure, porosity, surface roughness, residual stresses, hardness, tensile properties, and fatigue life [1], [9]–[13].

2.4.2 Recoating Mechanisms

Each manufacturer has developed their own recoating systems. These are either roller or scraper systems made from various materials. A roller system is a cylindrical device which rotates as it spreads powder, whereas a scraper system remains fixed and has a manufacturer specific profile [45], [46].

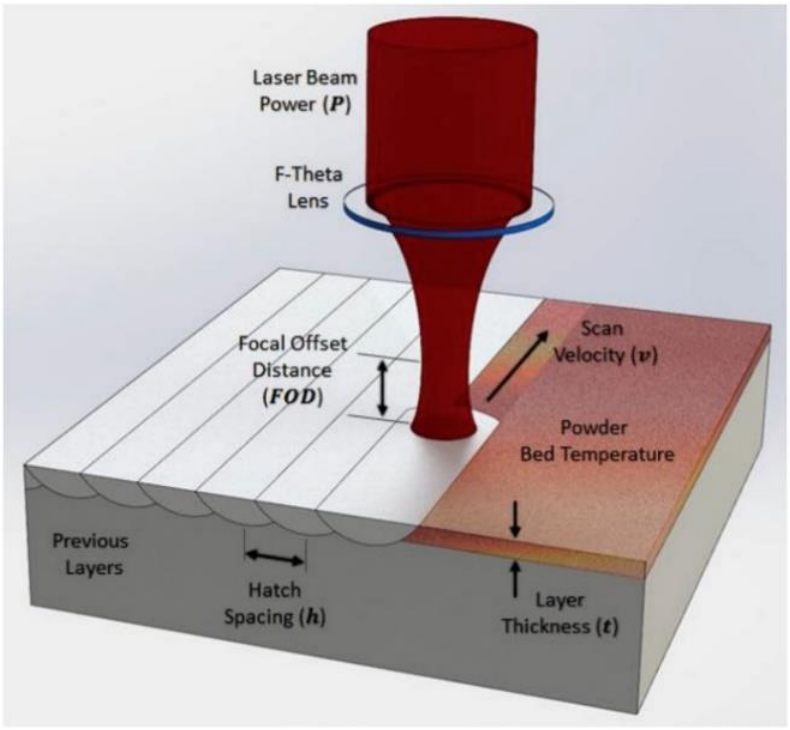

Figure 3: LPBF process parameters [1]

These systems are comprised of either soft or hard materials. Soft materials are typically polymers, such as silicone nitrile butadiene rubber, but can also be comprised of a carbon fibre brush. Hard materials include ceramics, high-speed and tool steels [47]. Hard recoaters are rigid and provide an even powder layer thickness with superior wear resistance but are typically more expensive than their soft material counterparts. The main benefit of soft recoaters is their cost and ability to deflect given a built defect [47].

2.5 Powder Blending

Powder blending is a field that has attracted little attention in AM. Powders used in AM are typically purchased PA and hence there is no need to mix or blend different powders together. It has been well documented that a high part quality can be achieved from readily available PA powders [48]. The major downfall of PA powders is the lack of flexibility to modify the alloying content, as well as the limited range of PA powders available for AM. If an AM manufacturer wants to produce an alloy for which there is not a commercially available AM powder, they would need to engage with powder manufacturers to make a custom batch of powder or create their own.

Powder blending using MA or elemental powders can be employed to facilitate the creation of powder blends with easily modifiable alloying weight percentages of different powders. Powder blending is a complex mechanical process which is affected by differences in morphology and cohesive nature of individual powders as well as the blending device, speed and time [49]. Powder blending is used extensively in conventional PM techniques mentioned in Section 2.2. In these industries, powder blending offers a major cost benefit over commissioning custom PA powders from powder manufacturers.

The cost of the raw materials was shown to be reduced by ~60 % by using blended powder for MIM of Ti-6Al-4V [50]. However, this is highly dependent on the supplier and quality of metal powder. Using elemental or MA powder blending of Ti-6Al-4V has been successful in achieving comparable results to its PA counterpart in the PM fields of: MIM [3], [50], sintering [2], [51], [52], and HIP [53], [54].

2.6 Powder Characterisation Techniques

In the LPBF process, the quality of the final component is a combination of the machines process parameters and the quality of the powder feedstock. There are several powder characterisation metrics that are widely used in the field of PM. These metrics primarily identify the size, shape, density, and flow properties of the powder. Understanding these properties and how they affect the suitability of a powder for use in AM, more specifically LPBF, is critical. An overview of each powder characterisation technique of importance will be discussed in this section.

2.6.1 Chemical Analysis

A chemical analysis is typically performed to determine the main and trace elemental composition of a material, covered in Section 2.8.1. The chemical composition specifications of grade 5 and grade 23 Ti-6Al-4V are shown in Table 3. In this study, only metal powders of the primary alloy elements, Ti, Al and V, or Al-V MA will be mixed together. Nevertheless, the trace element specifications must be met in the final blend, so it is important that the individual elemental or MA powders meet these limits.

Table 3: Chemical properties of various Ti-6Al-4V alloys

Element (%)	Al	V	Fe	C	O	N	H	Ti
Ti-6Al-4V (grade 5)[1]	5.5 - 6.75	3.5 - 4.5	<0.4	<0.08	<0.2	<0.05	<0.015	Bal.
Ti-6Al-4V ELI (grade 23)[2]	5.5 – 6.5	3.5 - 4.5	≤0.25	<0.08	≤0.13	≤0.05	≤0.015	Bal.

[1][55]; [2][43]

2.6.2 Powder Sampling

Powder sampling is important as it must be an accurate representation of the powder batch. There are industrial powder sampling machines, used by powder manufacturers, that avoid sampling bias [21]. One major concern when sampling powders results from powder settling during shipping; small vibrations over time will cause larger particles to rest on top and smaller particles to move to the bottom. It is therefore recommended to tumble a powder batch prior to sampling [21].

2.6.3 Powder Crystal Structure

The crystallographic structure of a material is measured using x-ray diffraction (XRD), details of which can be found in Section 2.8.4. XRD software is used to compare the XRD data to various published crystallographic information files (CIFs). Peaks from the data are matched and identified to obtain the crystallographic structures present in the material [6]. It should be noted that the wrought/cast Ti-6Al-4V alloy consists of an α+β microstructure, with α having a hexagonal close packed (HCP) crystal structure and β having a body centred cubic (BCC) crystal structure [56]. When the Ti-6Al-4V alloy is produced in processes involving rapid cooling rates, such as gas/plasma atomisation or laser powder

fusion processes, the microstructure consists purely of martensitic α' with an HCP crystal structure [53].

2.6.4 Powder Microstructure

To analyse the microstructure of powder particles, loose powder must be mounted in castable epoxy and prepared for metallographic analysis using various grinding, polishing and etching procedures [57]. This process is challenging and requires care as the small powder particles easily pull out of the epoxy during grinding. It is important to remove any bubbles from the epoxy when casting as this will accelerate the powder removal during grinding. Standard sample preparation procedures may be used but typically with reduced force and time due to the low metal surface area of the powder particles [57].

The prepared samples can be analysed using an optical microscope (OM) or a scanning electron microscope (SEM), details can be found in Section 2.8.2 and 2.8.3, respectively. The microstructure of plasma atomised PA Ti-6Al-4V powder typically consists of acicular α' martensite [24], [53], [58], seen in Figure 4a. Powder porosity, due to entrapped gas pores of gas atomised powders, may also be identified using this method [17], [22], [24], Figure 4b.

2.6.5 Morphology

The morphology (shape and size) of the powder particles is typically identified using a SEM. The SEM is the favoured tool as it is capable of capturing high resolution images of the 3-dimensional shape of powder particles at high magnification. This enables the user to clearly identify the morphology and surface topology of the powder particles.

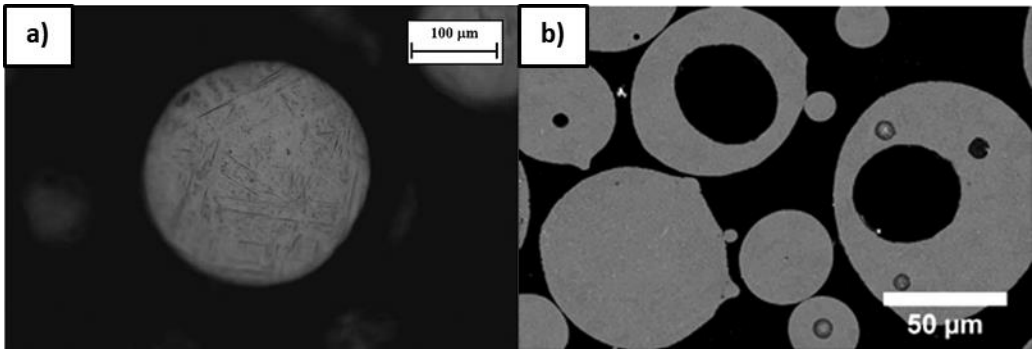

Figure 4: Powder microstructure of a) plasma atomised PA Ti-6Al-4V [53] and b) gas atomised [17] MAR-M-247 powder

The morphology of the powder particles is largely dependent on the powder production method used as well as the manufacturer. Powder morphology can vary from spherical, usually produced via atomisation techniques, to irregular, usually produced through milling techniques. Although quantitative two-dimensional size data may be extracted from the SEM images, this method is typically used as a qualitative metric.

A range of powder particle morphologies are shown in Figure 5. The gas atomised CP Ti and plasma atomised PA Ti-6Al-4V, Figure 5a and Figure 5b, respectively, have a highly spherical morphology. The milled 35Al-65V MA, Figure 5c, has an irregular angular morphology, and the water atomised 316L stainless steel powder, Figure 5d, has an irregular morphology. A powder with a more spherical shape has a higher flowability [5], [6], [19], [59]–[61] and a higher packing density [5], [7], [18], ultimately leading to a better print quality [7], [30]. This has been the preferred characteristic in AM for these reasons.

2.6.6 Particle Size and Particle Size Distribution

Particle size measurement of powders is used to determine the dimensions of each powder particle, with particles of a similar size batched together to determine a particle size distribution (PSD) for the total powder batch. There are four techniques commonly accepted when analysing the powder particle size, summarised in Table 4. Each technique has certain advantages and limitations in terms of accuracy, processing time and cost.

Table 4: Overview of PSD techniques [6], [21], [23]

Process	Particle Size Range	Fraction Type	Relative Cost (1 = lowest)	Relative Time (1 = fastest)
Sieving analysis	>25 µm	Mass	1	1
Image analysis	0-500 µm	2D volume	2	3
Laser diffraction	0-200 µm	*3D volume[1]	3	2
XCT analysis	0-500 µm	3D volume	4	4

[1]Psuedo 3D volume

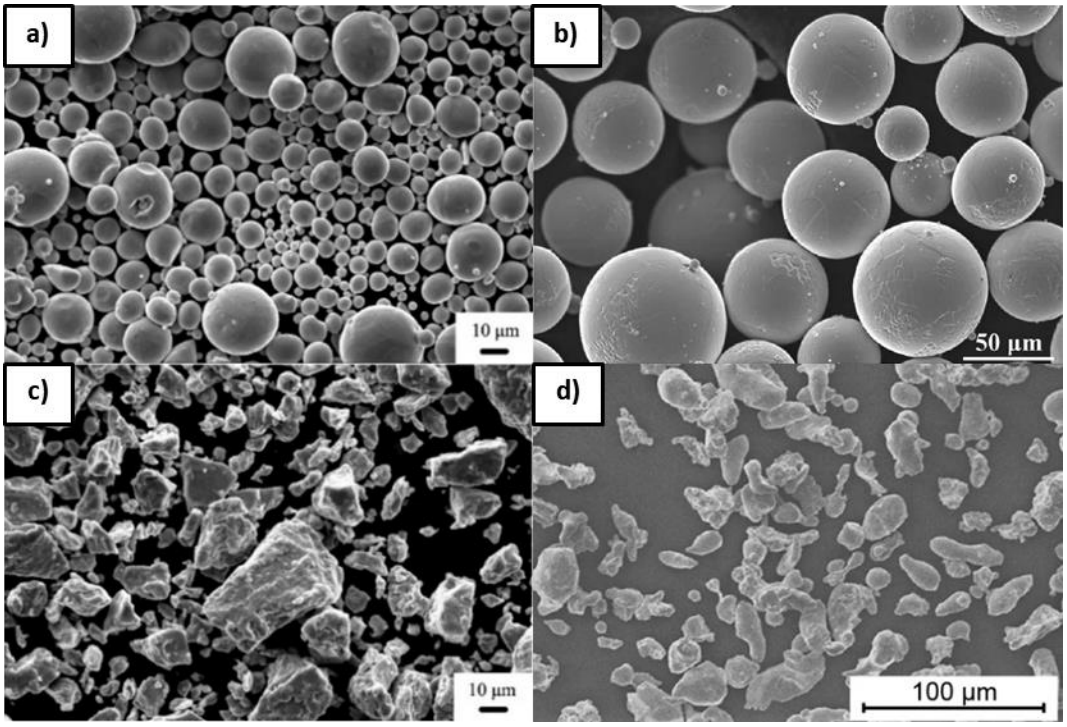

Figure 5: Powder particle morphologies of a) gas atomised commercially pure Ti powder [50], b) plasma atomised PA Ti-6Al-4V [22], c) milled 35Al-65V MA [50], d) water atomised 316L Stainless Steel powder [62]

Sieving analysis is a sizing technique used to measure larger particles with a few sieves having varying mesh sizes [63]. The mesh is created with a square grid of evenly spaced wires. The sieves are designated using the number of wires per linear inch [21], with a higher mesh designation number corresponding to a smaller gap opening. For example, the mesh designation of 325 corresponds to a hole opening of 45 µm. For a powder particle to pass through a 325 mesh, it must have a diameter or cross-sectional profile less than 45 µm.

To obtain a PSD from this method, sieves are stacked sequentially on a vibrating platform and a set mass of powder is passed through the top sieve having the largest hole opening. Each powder particle continues to flow through each sieve until it is deemed too large to pass, where it remains. The collective mass of powder from each sieve is categorised as a size between the sieve above it and the sieve it rests on. A PSD can now be obtained with the mass fraction of the individual sieve and the total [63]. The resolution of the PSD is determined by the adjacent sieves and corresponding mesh sizes [6], which is typically a low resolution of about 10 µm. It must be noted that sieves smaller than 45 µm do exist, however they are typically impractical to use as they are difficult and

expensive to manufacture and cause agglomeration of particles which prevents them from passing through. Due to the size of higher quality AM powders being <45 µm, this technique is limiting and is typically only used for larger particles.

Image analysis determines the size of the particles using mainly either OM or SEM. With OM, the powder is typically mounted in resin and through various grinding and polishing procedures, the cross-section of the powder particles is revealed. The cross-sectional dimensions and subsequent PSD of the powder particles may be obtained manually using relevant OM software or automatically through OM software packages or self-coded algorithms. With SEM, the loose powder is mounted on double-sided carbon tape and an image is generated from a single viewing direction. This image can be processed in a similar way to the OM technique with relevant SEM software. These imaging techniques are time consuming and require extensive processing to analyse a sufficient number of particles [6].

Laser diffraction is a particle sizing technique where particles are usually immersed in a fluid medium, and a laser, perpendicular to the flow stream, is directed at the flowing particles. The particles obstruct the light and create a scattering pattern on a detector, usually a charged-coupled device (CCD). A schematic of this technique can be seen in Figure 6. An appropriate mathematical model is applied to the data, either Mie or Fraunhofer theory. The Mie theory is preferred for smaller particles and requires the input of the refractive index of both the fluid medium and the sample. One of the main limitations of this technique is that it assumes particles to be spherical [21], [23]. This means that the PSD of highly spherical particles produced through gas and plasma atomisation processes will be accurate whereas the PSD of irregular shaped particles produced through water atomisation or milling processes may be inaccurately represented through this technique.

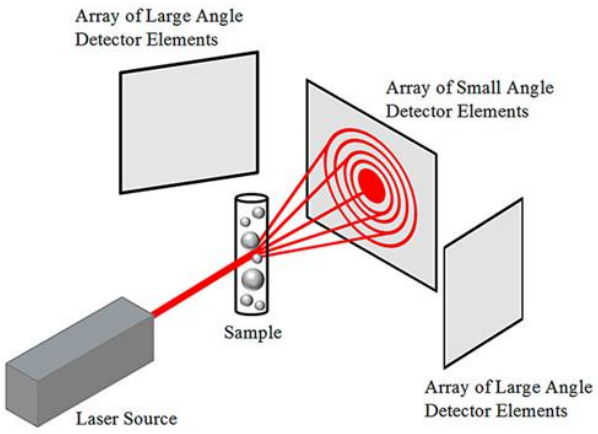

Figure 6: Laser diffraction schematic [6]

X-ray computed tomography (XCT) analysis is the most comprehensive of the techniques. The principle of an XCT scanning machine is that a sample is mounted on a rotating stage and x-rays are directed at the sample. A detector on the far-side of the sample picks up the x-rays that were able to penetrate the sample and converts this to a grayscale value. A set number of projection images are captured at incremental rotations of the stage, until a full 360-degree rotation is completed. The depth of each projection image is known as the resolution of the scan. A three-dimensional volume is then reconstructed through dedicated software [64]. The full volume of each particle in the analysis region is captured. Particles can then be batched into groups with similar particle volumes and a PSD can be generated. Challenges with this technique are the achievable resolution as well as obtaining high contrast images of materials with a low density and low atomic number.

The PSD is typically reported as a graph of: volume frequency percent vs. particle diameter; cumulative volume finer percent vs. particle diameter; or the D_{90}, D_{50}, and D_{10} values corresponding to the maximum particle size of 90 %, 50 %, and 10 % of the particles. Powders with a span greater that 1.5 typically exhibit poor flow, whereas those with a span less than 1.5 have better flow properties [5]. The span is reported as [65]

$$\text{Span} = \frac{D_{90} - D_{10}}{D_{50}} \qquad (2.2).$$

2.6.7 Powder Density

Density as a characteristic is a straightforward ratio of an object's mass to its volume. However, the naming scheme of different densities can vary drastically

from discipline to discipline. There are several density parameters used frequently in PM: theoretical, skeletal, packing, apparent, tapped, and relative density.

Theoretical density is the mass of a perfectly solid sample over its exact volume, corresponding to the handbook density [21] and sometimes referred to as true density. **Skeletal density** is the mass of a number of powder particles over their solid volume including any internal pores. This is sometimes referred to as the pycnometer density [66] and is measured by placing powder of known mass in a crucible of known volume and filling it with pressurised nitrogen or helium. The ideal gas law is employed to calculate the volume of the powder particles including closed off pores [21].

Packing density is based on the settling density of a number of powder particles. Powders particles typically undergo random packing, which means the packing structure has no repeated arrangement [67]. The maximum packing density is achieved when small particles fill the space between the larger particles, Figure 7.

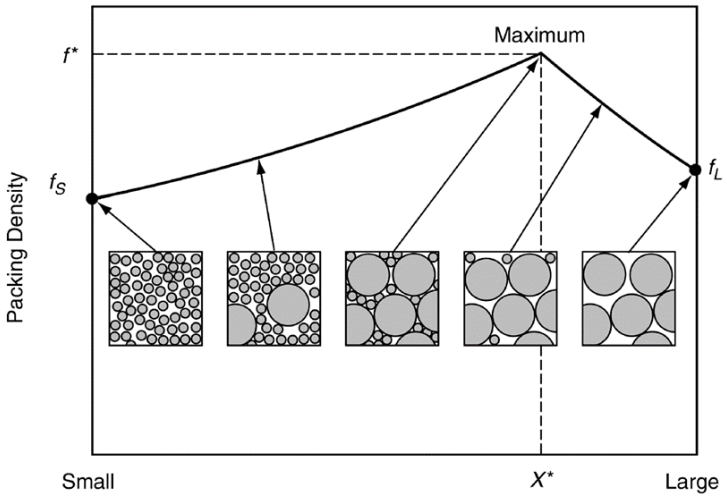

Figure 7: Powder packing density [67]

Apparent density (AD) is essentially the packing density of loose powder funnelled into a crucible of known volume without any vibration. The mass of the added powder is then easily determined. **Tapped density** is when a powder sample of known mass is poured into a measuring cylinder and vibrated until no change in volume is identified [68]. The final volume is used in the density calculation. **Relative density** is the normalised density given as the ratio of a particular density and true density [59].

2.6.8 Flowability

The flowability of a powder is determined by passing powder of set mass through a funnel with a small orifice and determining its flow rate (FR). This metric was developed for die filling in traditional PM [19], where powder is funnelled from a feed shoe into a die cavity. The Hall flowmeter is typically used to determine this metric, which has a small orifice of 2.54 mm, and tends to only accommodate coarser and free-flowing powders to pass through uninterrupted. In this test, 50 g of powder is passed through the funnel and the FR is determined. Powders which are unable to pass through the funnel, are considered “no flow” powders [69]. To obtain a quantitative metric for the flowability of such powders, the Carney flowmeter with a with a larger orifice of 5.08 mm, may be employed [70], which determines the FR of 200 g of powder through the funnel.

Powders with a spherical shape tend to flow better [5], [6], [60], [61], [7], [11], [18], [26], [27], [40], [45], [59] due to reduced mechanical interlocking and surface friction. The same can be said about powders with a fewer number of fine particles [5], [6], [59]–[61], [71]–[73], [7], [11], [17], [18], [26], [27], [40], [45] due to reduced cohesive forces, inter-particle friction, and van der Waals forces. Moisture or humidity also inhibits the flowability of powders [6], [18], [59], [73] due to capillary forces and liquid bridging, which has led some researchers to dry powders prior to flowability testing [59], [60].

There is a trade-off between flowability and powder bed density. A larger number of fine particles is said to increase the powder bed density with the reduction in flowability [5], [6], [40], [59], which is illustrated in Figure 8. The flowability of a powder has been widely accepted as a powder characterisation metric in AM and more specifically LPBF [7], [45], [59], [60], [74]; however, this metric fails to mimic the recoating process of a LPBF machine [19], [45], [59], [61]. This will be covered in Section 2.7.

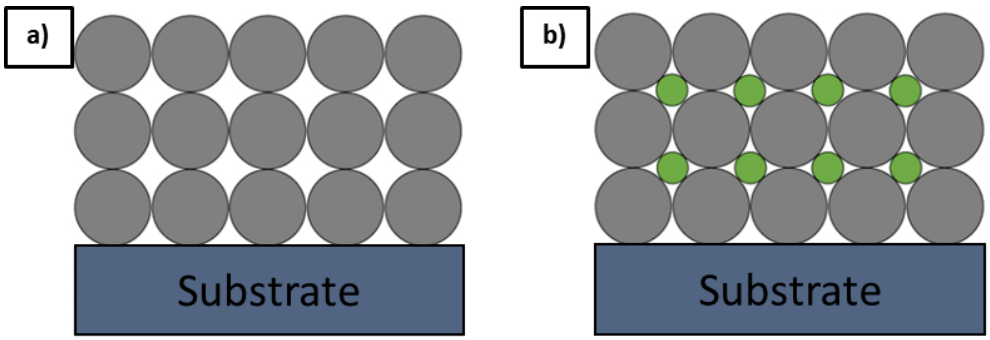

Figure 8: Powder bed packing [59] adapted with a) lower density and shear force required (optimised flowability) and b) higher density and shear force (optimised powder bed density)

2.6.9 Angle of Repose

The angle of repose (AoR) is the angle at which a heap of powder rests prior to collapsing under the force of gravity, due to inter-particle friction. There are a few ways to determine this parameter with the two most popular being the fixed funnel method and the rotating cylinder/drum method [75], shown in Figure 9.

In the fixed funnel method, a powder sample is poured from a set height through a funnel onto a flat surface, Figure 9a. The height and average diameter of the powder heap may be measured manually or optically using a camera. The arctan of the ratio of the height and average radius may be used to calculate the AoR [75]–[77]. In the rotating cylinder/drum method, a powder sample is placed in a drum with transparent sides, Figure 9b. Typically, a light source is positioned at the far side of the drum and the drum is rotated at a fixed speed. The maximum angle formed is known as the dynamic AoR [75] and the angle is measured using a camera and imaging software [60], [77].

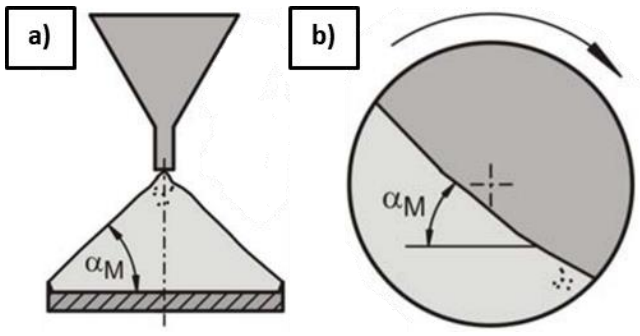

Figure 9: AoR methods [78] of the a) fixed funnel and b) rotating drum method

2.7 Spreadability

In LPBF processes, the ability of a powder to be uniformly distributed over the build plate i.e. the spreadability of the powder, is essential to ensure a high quality and pore-free part [19], [45], [59], [61]. Typical powder characterisation techniques in industry include particle morphology, PSD, AD and flowability. Although these metrics do have value when characterising the suitability of a powder in AM, as they fail to mimic the actual spreading mechanism used in LPBF processes [19], [45], [59], [61].

2.7.1 Discrete Element Method

The discrete element method (DEM) is a numerical simulation technique first developed by Cundall and Strack [79] in a study of granular assemblies. This tool allows for the physical behaviour of numerous particles to be predicted. Discrete bodies interact with neighbouring particles through various contact laws, and position, velocity and acceleration of each particle can be determined in three-dimensional space. The DEM has been employed in numerous industries, such as the, chemical, ceramic, pharmaceutical, agricultural, food, geological, and metal industries. The DEM has seen particular interest in several studies in the field of AM [80]–[89] and, notably, for Ti-6Al-4V [90]–[94] focussing primarily on the powder layer spreading process.

One of the main drawbacks of using the DEM is generating the 3D shapes of the powder particles. Highly spherical powders are better predicted but irregular powders prove to be difficult. When generating the 3D models of irregular shaped powder particles, a select few particles are imaged using either OM, SEM, or XCT and form the base models for the simulation database. These particles are simplistic models of the realistic particles as retaining surface details would lead to infeasible large scale DEM simulations [89]. Several studies have investigated the flow properties of irregular shaped particles using the multi-sphere approach, whereby the shape of the powder particles is approximated using overlapping spheres [80], [82], [83], [89].

2.7.2 Custom Spreadability Rigs

A limited number of physical spreadability test rigs have been developed in published literature. The simplest being developed by Ahmed *et al.* [95], whereby powder is poured onto a small cardboard stencil with a rectangular cut-out, Figure 10a, resting on fine emery paper. The carboard stencil is removed, leaving behind

a powder heap, Figure 10b. The heap is subsequently spread by hand using a machined spreader of known height, Figure 10c.

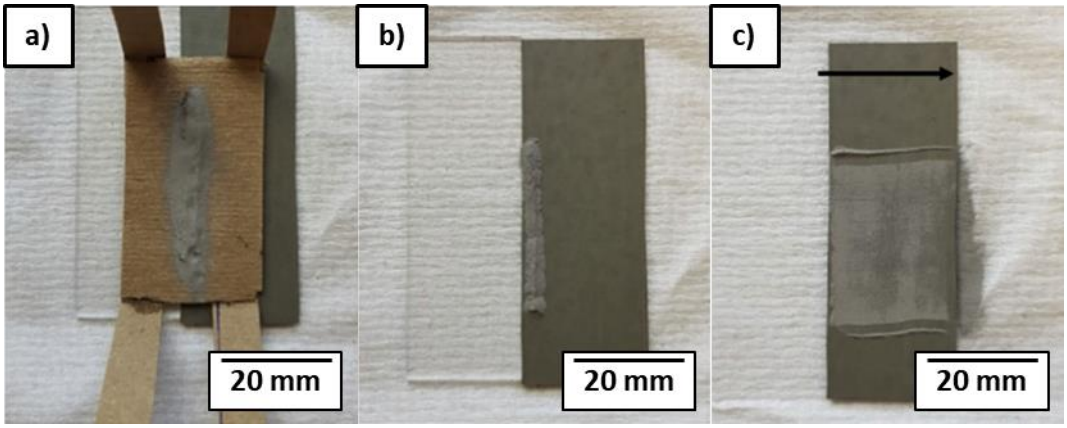

Figure 10: Custom spreadability experimental setup of a) a simple cardboard stencil, b) remaining powder heap, c) manual powder spread on emery paper [95]

Another manual spreading device developed by Cordova *et al.* [59] can be seen in Figure 11a. Powder is poured into a machined device with an applicator of known height and manually spread on a long metal strip (approximately 900 mm). The machined device accommodated two powder funnel variations ahead of the spreading applicator, one being a sloped funnel towards the applicator, and another being open with no powder funnelling.

The most comprehensive study on powder spreadability was conducted by Snow, Martukanitz and Joshi [45], and can be seen in Figure 11b. The rig has an automated 3D gantry resembling an FDM printer and a design based off the recoating process of an EOS M280. The rig has a manually adjustable aluminium build plate, and an automated variable speed spreading system that can accommodate a range of recoating blades. The rig can also accommodate two sensing devices. The first being a camera mounted above the build plate to take optical images of the spread layer, and the second being a portable microscope placed on the side of the recoater blade used to capture video footage of the powder heap ahead of the recoater.

The final design, seen in Figure 11c, is a modified version of a film applicator typically used to test the coverage performance of paint [74]. The rig makes use of fine sandpaper (P120) placed on the default glass plate. The rig has a manually adjustable plate and an automated variable speed spreading mechanism.

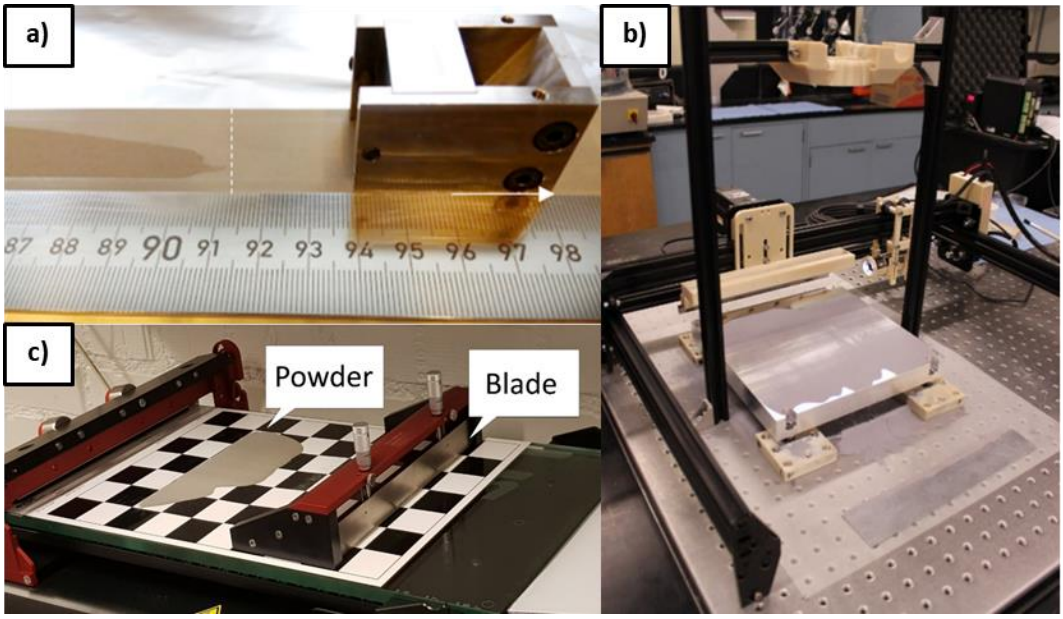

Figure 11: Custom spreadability experimental setup of a) a machined manual spreadability applicator [59], b) an automated spreadability test rig [45], c) a modified film applicator [74]

2.7.3 Spreadability Metrics

Several spreadability metrics have been developed from the processes developed in Section 2.7.2, among others, and these metrics are discussed in this section.

Percent coverage, developed by Snow, Martukanitz and Joshi [45], is the coverage of a powder spread layer on a build plate, of set mass

$$m = \frac{At}{\rho_a} \tag{2.3}$$

where *A* is the area of the build plate, *t* is the layer height, and ρ_a is the apparent density of the powder. Once the powder has been spread, the area of interest is cropped and converted to a binary image in MATLAB using Otsu's method [96], shown in Figure 12. It was reported that the percent coverage was the ratio of white pixels to black pixels as a percentage [45], however this was assumed to be incorrect as the true ratio should be the number of white pixels to total pixels as a percentage. Brisenmark and Lindström [74] obtained a similar parameter using the open source software ImageJ for image processing.

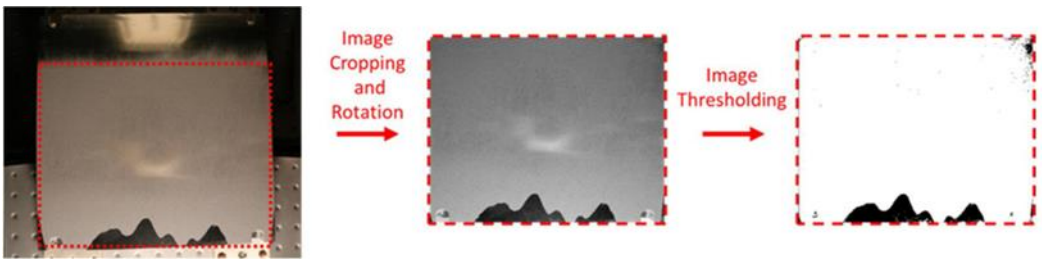

Figure 12: Image processing from an overhead image to determine the percent coverage [45]

The **spread density** of a powder is essentially the AD of the powder particles in a spread powder layer on a build plate. Several studies have analysed this parameter, often being referred to as the powder bed density [71], apparent powder layer density [59], powder spread density [60], packing density of the powder layer [84]. These studies aim at achieving the same parameter through different techniques, as summarised in the next paragraphs.

The powder bed density was determined by placing a disk on the build plate of a LPBF printer and spreading three powder layers. The powder bed density was calculated as [71]

$$\rho_{PB} = \frac{m_{PB}}{V_{PB}} \tag{2.4}$$

$$V_{PB} = A_{PB}t \tag{2.5}$$

where m_{PB} is the mass of the powder resting plate and V_{PB} is the total volume created by the area of the plate, A_{PB}, and the layer height, t.

The apparent powder layer density [59] was determined using the simple test rig of Figure 11a and described in Section 2.7.2. This parameter was calculated similarly to Equation (2.4). The powder spread density, determined by Muñiz-Lerma *et al.* [60], was calculated by XCT scanning a single powder spread layer on a custom CT test holder. The powder layer was deposited on the test holder using the doctor blade technique. The spread density was calculated as the ratio of total powder volume and the total scanned volume as a percentage.

The packing density of the powder layer [84] was investigated by partially sintering small squares on a single powder layer in a LPBF printer. The surrounding powder was brushed away and the remaining partially sintered small squares were weighed, and the density was calculated similarly to Equation (2.4). Spread

uniformity [95], was determined using SEM images of the powder layer and analysed in terms of the size and frequency of the voids present in a powder layer. Image processing was performed using a combination of ImageJ and MATLAB.

The **dynamic AoR** is the angle the powder front, ahead of the recoater blade, makes with the build plate. This parameter was measured using a spreading mechanism and *in-situ* XCT imaging [97]. Snow, Martukanitz and Joshi [45] obtained a similar parameter using a portable microscope as described in Section 2.7.2, but referred to it as the **avalanching angle**.

2.7.4 Spreading Defects

The majority of spreading defects are caused by irregular shaped particles, moisture, and oxide layers. An illustration of the effect of an irregular shaped powder particle, seen in Figure 13b, indicates how a poorly orientated powder particle can cause areas of jamming beneath the recoating blade.

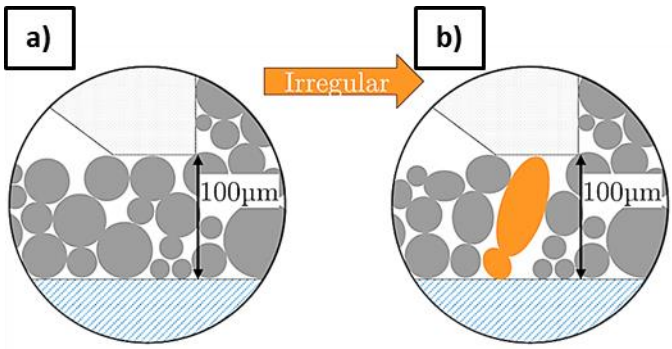

Figure 13: Powder spreading side view [59] of a) spherical particles and b) an elongated particle causing jamming

When powder particles come into contact with each other, they are subject to electrostatic forces, van der Waals forces, and capillary forces [18], [93]. Moisture has been shown to inhibit the flowability of powders [60], [75], [76] mainly from the influence of capillary forces [59], [98] and natural oxide layers [5].

An illustration of the effect of moisture and oxide layers on spreading can be seen in Figure 14. Moisture pickup can cause powder particles to form liquid bridges between each other which causes agglomeration, Figure 14b. This moisture can lead to thicker oxide layers forming on powder particles resulting from air drying. Aluminium alloys are particularly susceptible the formation of these oxide layers and was seen to improve spreadability [59].

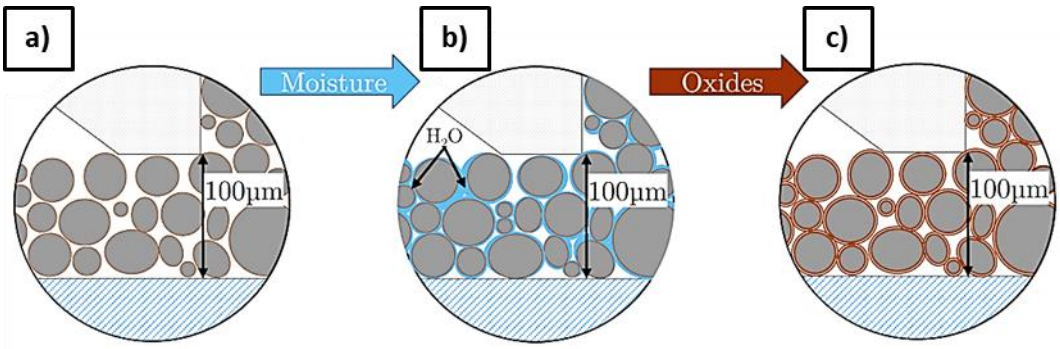

Figure 14: Powder spreading side view [59] adapted of a) natural oxide layers on metal powder particles b) liquid bridges between powder particles and c) thick oxide layers

2.8 Material Characterisation Techniques

2.8.1 Chemical Properties

The chemical properties of a material include analysis of the quantities of trace elements that are present. In AM, this is an important consideration as final components must meet certain chemical composition specifications. A key consideration is the amount of oxygen present in the powder before use in LPBF.

Inductively coupled plasma - optical emission spectrometry (ICP-OES) is a trace element detection method. The technique involves plasma energy being supplied to a typically liquid sample, exciting the component elements. Solid samples that may be vaporised, i.e. metal powders, may also be analysed using this method. These excited atoms return to a low energy position, releasing emission rays, and the corresponding photon wavelength is measured. Based on the position of the photon rays and the rays' intensity, the element type and content can be determined, respectively [99].

ELTRA is a German company which produces elemental analysers. Their oxygen/nitrogen/hydrogen determinator is particularly useful when analysing samples for these elements. This method uses full combustion of a sample to measure the combustion gas content with infrared absorption and thermal conductivity [100]. The method is capable of analysing a wide variety of materials including ceramics, metals and inorganic materials. There are two analysis options: fractional analysis used to identify oxygen and nitrogen; and hot extraction analysis to identify hydrogen [100].

2.8.2 Optical Microscopy

The OM typically consists of three separate systems, namely the: illuminating system; specimen stage; and imaging system [101]. The illuminating system ensures the specimen is well lit in the field of view, the sample rests on the specimen stage, which has three translational degrees of freedom, and the imaging system enables a magnified and sharp image of the sample to be captured by an imaging device [101]. A schematic of an OM is seen in Figure 15a.

Optical microscopy is primarily used for identifying surface morphologies and crystalline phases in a material. For metallographic analysis, the light source does not pass through the sample, but is rather reflected off the surface of the polished specimen to obtain the surface topology and features of the specimen. Optical microscopes have a zoom capability is dependent on the magnification of both the eyepiece and the objective lens. These two magnifications are multiplied together to obtain the total magnification, which is usually up to x1000, but higher magnifications are attainable, with the typical resolution is about 1 µm [102].

2.8.3 Scanning Electron Microscopy with Spectroscopy

The SEM utilises a focussed beam of electrons to bombard a specimen and produce signals, which are received by various detectors. Backscattered and secondary electrons are typically detected, as well as characteristic x-rays. High energy backscattered electrons result from an elastic interaction between the electrons and the sample and originate from deeper in the sample. In contrast, low energy secondary electrons result from an inelastic interaction between the electrons and the sample and provide details of the surface of the sample [103].

Characteristic x-rays are detected using energy-dispersive spectroscopy (EDS) or wavelength-dispersive spectroscopy (WDS). EDS collects excited photons and the chemical composition of a region can be determined, whereas WDS obtains the intensity of the x-rays in terms of their wavelength [101].

The SEM is comprised of a microscope column, signal detectors, hardware and software collection devices and recording systems, and typically have a resolution of up to 0.09 µm [102]. A diagram of the SEM indicating the electron beam and various emitted electrons can be seen in Figure 15b.

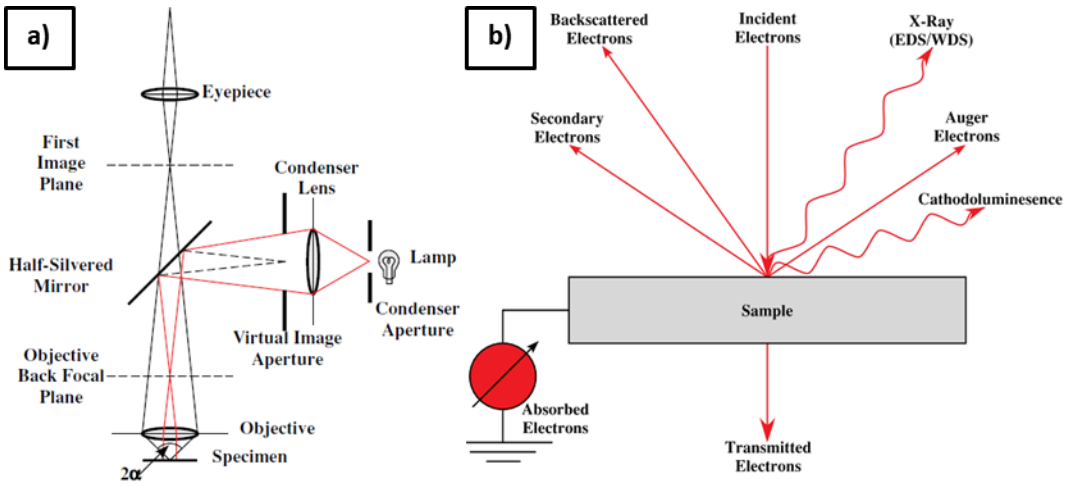

Figure 15: a) OM schematic [101] and b) SEM diagram [101]

2.8.4 X-ray Diffraction

XRD utilises the principle that x-rays are either scattered or absorbed by an object. The reaction is fully elastic when scattering occurs which means the wavelength remains unchanged [101]. The working principle of an XRD machine is that an x-ray source strikes a sample and the scattered x-rays are read by a collector, which is shown in Figure 16a. The x-ray source *T* strikes the sample *S*, which is collected by collector *C* [102]. Either the sample or the attached source and collector can be rotated about the origin axis.

The diffraction angle 2θ can be recorded along with the beam intensity and plotted similarly to Figure 16b. The combination of the diffraction angle (according to Bragg's law) and the intensity of the peaks can be compared with an existing CIF to identify the crystalline phases present in the sample [101].

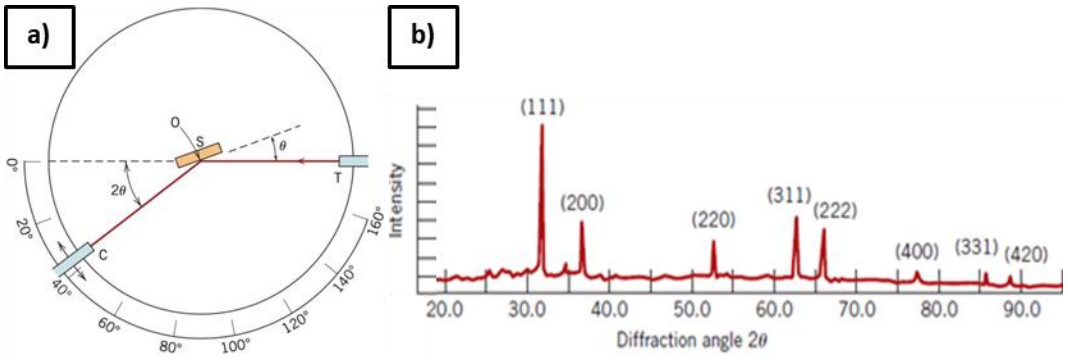

Figure 16: XRD a) schematic [102] and b) diffraction spectrum of powdered lead [102]

3 Methodology

The methodology followed in this study is outlined in this section. It is important to reiterate that this project was carried out in conjunction with a master's project at CUT. The process flowchart of the combined projects can be seen in Figure 17, with the focus for this specific project emphasised by the highlighted blocks.

While the primary aim of the projects was to investigate the development of metal powder blends for LPBF, this project specifically focussed on the blending and characterisation of the metal powders and blends, after which the powder blends were delivered to CUT, Bloemfontein, for evaluation of the powder blend suitability for AM. The methodological approach was to build on current literature and research findings to design a set of experiments that will evaluate the suitability of metal powder blends, as opposed to PA powders, for LPBF of Ti-6Al-4V.

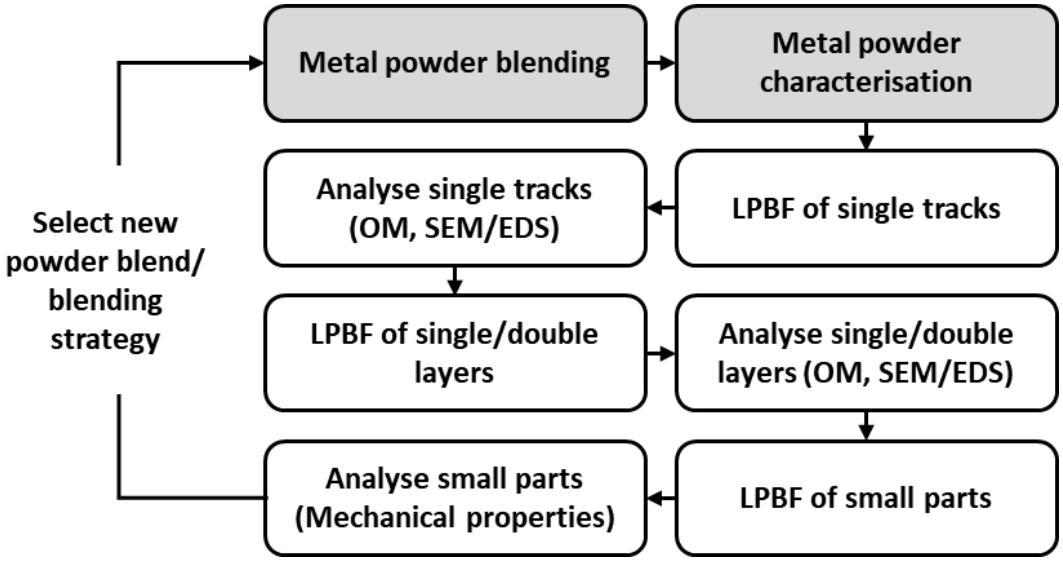

Figure 17: Flowchart of the development of a novel powder blend for use in LPBF processes, with the highlighted tasks that are the focus of this study

3.1 Raw Powder Specifications

The specifications of the raw powders used throughout this project are shown in Table 5. The powders used in the project are: PA Ti-6Al-4V, commercially pure (CP) Ti, 60Al-40V MA, and elemental Al and V.

Table 5: Supplied powder specifications

Powder	Size Spec (µm)	Production Method	Supplier	Date Supplied
PA Ti-6Al-4V (grade 5)	10-45	Plasma-atomised	AP&C (Canada)	2017/07
CP Ti (grade 1)	10-45	Plasma-atomised	AP&C (Canada)	2017/07
MA (60Al-40V)	<45[1]	Aluminothermic reduction	Reading Alloys (PA, USA)	2017/05
Al (grade 2)	<45	Gas-atomised	Valimet (CA, USA)	2017/09
V	<45	Aluminothermic reduction	LabChem (SA) Alfa Aesar (Global)	2020/03

[1] Equivalent to -325 mesh

3.2 Powder Blending

Two novel Ti-6Al-4V powder blends were investigated in this project, namely:

1. CP Ti-10 MA blend
2. CP Ti-6Al-4V elemental blend

The MA blend is referred to as Blend 1 MA and the blended elemental (BE) blend is referred to as Blend 2 BE for the duration of the thesis. The powders were weighed out using weighing paper and an A&D FX 1200i precision scale. The powder blends were mixed using a 3D Turbula®-like mixer, driven by a SEW-Eurodrive motor and Movitrac controller. Prior to mixing, the powders were dried in air at 120 °C for four hours using a Gallenkamp Hot Box Oven Size One, to remove any moisture present in the powder from storage. The reasons for this were covered in Section 2.7.4.

Blend 1 MA was mixed in two batches of 600 g and 750 g, respectively. They were both mixed in a 640 ml plastic container with a seal and a screw top lid. According to the measured AD of the powder, the container was 41 % full for the first batch and 52 % full for the second batch. Each batch was blended at a speed of 250 rpm for 15 minutes. 200 g was sampled from the first batch and 150 g from the second batch for powder characterisation tests. The remaining batches of 400 g and 600 g were sent to CUT for further LPBF processing.

Blend 2 BE was mixed in three 600 g batches using a 640 ml plastic container with a seal and a screw top lid. Each container was filled with argon prior to mixing as

the vanadium powder oxidises rapidly out of an inert atmosphere. According to the measured AD of the powder, the container was 40% full. Each batch was blended at a speed of 200 rpm for 20 minutes. 100 g from each batch was sampled for powder characterisation tests and the remaining 500 g from each batch (total of 1.5 kg) was combined into a single larger container and shipped to CUT for further LPBF processing. Table 6 provides a summary of the powder blending details.

Table 6: Powder blending summary

Powder Blend	Batch No.	Mass (g)	Container Size (cm^3)	Speed (rpm)	Time (min)	Sampled Mass (g)	Final Mass (g)	Shipped Date
Blend 1	1	600	640	250	15	200	400	09/2019
MA	2	750	640	250	15	150	600	11/2019
Blend 2 BE	1	600	640	200	20	100	1500 combi-ned	08/2020
	2	600	640	200	20	100		
	3	600	640	200	20	100		

3.3 Powder Characterisation

A summary of the powder characteristics that were evaluated, along with the relevant testing methods and apparatus, are presented in Table 7. The details of each measurement are presented in the subsequent sections.

Table 7: Powder characterisation test details

Powder Characteristic	Process	Equipment
Chemical analysis	1. ICP-OES 2. O_2 and N_2 combustion	1. SPECTRO ARCOS ICP-OES 2. ELTRA ONH-2000
Crystallographic structure	XRD	Bruker D2 Phaser
Powder microstructure	OM	1. Buehler Grinder/Polisher 2. Grinding paper and polishing equipment 3. Olympus GX51 (Inverted metallurgical light microscope)
Particle morphology	SEM/EDS	Zeiss Merlin FESEM with an EDS detector

Particle size distribution	1. Laser diffraction 2. XCT scanning	1. Saturn DigiSizer 5200 V1.12 2. Nanotom S nanoCT
Theoretical density	As specified by supplier	None
Skeletal density	ASTM B923 [104]	1. Kern ABT 120-5DM precision scale 2. Quantachrome Instruments - Ultrapyc 1200e Automatic Gas Pycnometer
Apparent density and flowability	1. Free-flowing powders: [105], [69] 2. Non-free-flowing powders: [106], [70]	1. Hall flowmeter 2. Carney flowmeter 3. A&D FX 1200i precision scale
Angle of repose	Angle of repose measurement	1. Hall flowmeter 2. Carney flowmeter 3. Camera: Canon EOS 750D 4. Lens: Canon 50 mm 5. Tripod: Manfrotto 290 dual 6. Microsoft PowerPoint
Powder blending quality	ASTM B923 [104]	1. Kern ABT 120-5DM precision scale 2. Quantachrome Instruments - Ultrapyc 1200e Automatic Gas Pycnometer
Spreadability	-	Custom designed spreadability test rig
Percent coverage	Digital image analysis	1. A&D FX 1200i precision scale 2. Camera: Canon EOS 750D 3. Lens: Canon 50 mm 4. Tripod: Manfrotto 290 dual 5. MATLAB
Spread density	Mass and volume measurement	1. A&D FX 1200i precision scale 2. Camera: Canon EOS 750D 3. Lens: Canon 50 mm 4. Tripod: Manfrotto 290 dual
Elemental distribution	SEM/EDS	1. Custom stub holder 2. SEM pin stub 3. Double sided carbon tape

3.3.1 Chemical Analysis

The chemical analysis of the powders was obtained using ICP-OES, with the O and N content measured using the gas fusion technique by ELTRA. More information on each process can be found in Section 2.8.1. The testing was subcontracted to the Nuclear Energy Corporation of South Africa (NECSA) and they completed the analysis using a SPECTRO ARCOS ICP-OES and an ELTRA ONH-2000. The analysis was conducted on the CP Ti and MA powders and the reports can be found in Appendix D.1. The chemical properties of the PA Ti-6Al-4V, Al and V powders were reported from the relevant supplier.

3.3.2 Powder Crystal Structure

The crystallographic structure of the individual loose powders was obtained using XRD and MAUD software [107]. MAUD software was used to fit the relevant CIF to the raw XRD data. The CIFs were gathered from various online databases, namely, the Materials Project database [108], the Crystallographic Open Database [109]–[114], and AtomWork [115]. The XRD testing was conducted on a Bruker D2 Phaser fitted with a copper anode by Dr Loots in the Department of Chemistry and Polymer Science at SU.

3.3.3 Powder Microstructure

The loose powders were cold mounted in clear epoxy, using Struers EpoFix resin and hardener system [116], [117]. The resin and hardener, in a 25:3 weight ratio measured using an A&D FX 1200i precision scale, was mixed thoroughly by hand with a small plastic mixing stick for two minutes in a Struers Fixiform cylindrical mount form. Then a small amount of loose powder was added to the mixture, which was mixed for a further three minutes to ensure that the powder particles were fully dispersed in the resin. This is important to prevent powder particles from being pulled out of the resin during the grinding or polishing procedures [57]. The powder-epoxy mixture was then placed in a Buehler Cast n' Vac 1000 vacuum chamber and a low vacuum was pulled for two minutes to remove any bubbles in the mixture. The mount was left to cure for 24 hours before being removed from the form.

Relevant grinding, polishing and etching procedures were followed to reveal the powder microstructure. A Buehler 2-Speed Grinder-Polisher, fitted with a Vector Power Head, was used for both grinding and polishing procedures. An inverted metallurgical light microscope (Olympus GX51) was used to observe the

microstructure and the digital imaging software, Streamline 1.8 (Olympus), was used to capture images.

The grinding and polishing steps used for each powder can be seen in Table 28, Appendix A.1. The procedures were loosely based on Struers sample preparation procedures for PA Ti-6Al-4V and CP Ti [118], and Al, MA, and V [119]. It was noted that small bubbles formed on the surface of the cured epoxy along the walls of the mount. As this would provide an uneven surface for the piston of the grinding machine, the top surface of the sample was first ground using #500 SiC grit paper until it was plane. OM images were taken of all the polished samples, before and after etching, and samples were etched according to Table 8.

Table 8: Etching procedure for OM of loose powders

Powder	Etchant Name	Etchant Mixture	Immersion/Swabbing	Time [s]
CP Ti Ti-6Al-4V	Kroll's Reagent	92 ml distilled water 6 ml Nitric acid 2 ml Hydrofluoric acid	Swabbing	7
Al MA V	Keller's Reagent	190 ml distilled water 5 ml Nitric acid 2 ml Hydrochloric acid 2 ml Hydrofluoric acid	Immersion	20

3.3.4 Morphology and Elemental Analysis

The morphology of the powder was observed using a Zeiss Merlin field emission SEM (FESEM) with an EDS detector. Loose powder was poured onto double sided carbon tape stuck on an aluminium stub. Excess powder was blown off with a small handheld blowing device and subsequently carbon coated before being placed on the SEM mount. The typical SEM settings used to observe the powders are seen in Table 9.

Table 9: SEM settings

EHT[1] (kV)	Current (pA)	Detector	Working Distance (mm)	Brightness (%)	Contrast (%)
Imaging: 2-3	100	InLens & SE2	±5-6	±50	±30
EDS: 18-20	1400	BSD[2]	9.5	±50	±30

[1]Electron high tension; [2]Backscattered electron detector

The SEM images were captured at the Central Analytical Facilities (CAF) lab in the Geology Department at SU. The combination of the InLens and SE2 detectors allow for the detection of two types of secondary electrons (SE1 and SE2). The images of the CP Ti, MA, and Blend 1 MA were captured by the author in August 2019 and the remaining images were obtained by the lab analyst, Ms Alicia Botes, due to the COVID 19 restrictions, in September 2020. EDS maps were obtained by Ms Alicia Botes on the PA Ti-6Al-4V and the two blends to differentiate the individual elements more clearly. The BSD allows for the detection of backscattered electrons.

3.3.5 Particle Size Distribution – Laser Diffraction

The PSD was determined using laser diffraction for all the powders. The laser diffraction was conducted with a Micromeritics Saturn DigiSizer 5200 V1.12 by Mrs Hanlie Botha at the Process Engineering Department at SU. This particle sizing device uses the laser diffraction analysis technique to determine the volume frequency of the powder particles and the data was processed using the Mie theory model. All powders were analysed with three tests being averaged and with three standard deviations as the error.

The powders were suspended in distilled water with a flow rate of 12 l/min and sonicated for 60 s before measurement. A refractive index of 2.22 was use for CP Ti, PA Ti-6Al-4V and the blends; 1.741 for the MA; 1.488 for the Al; and 2.36 for the V. The resulting plots of volume frequency percent vs. particle diameter and cumulative finer volume percent vs. particle diameter for all powders were determined. Additionally, the D10, D50, and D90 distribution points as well as the span and average particle size of the powders was reported. One downside to laser diffraction is that it assumes the powder particles to be spherical and may lead to an inaccurate PSD of irregular shaped powders [21]. This is illustrated by an irregular shaped powder particle measured in two different orientations, Figure 18, obtaining significantly different particle diameters.

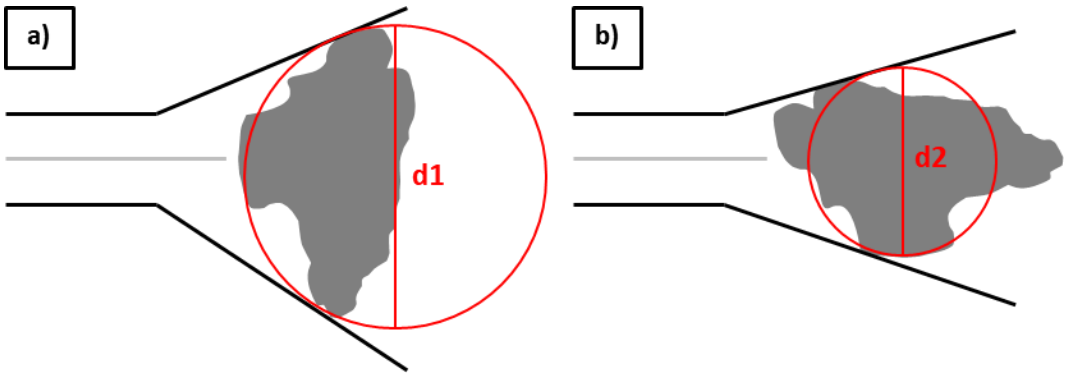

Figure 18: Laser diffraction schematic of an irregular powder particle in the a) vertical orientation and b) rotated 90 ° anticlockwise

3.3.6 Particle Size Distribution – X-ray Computed Tomography

XCT scanning was performed on the vanadium powder. Due to the irregular nature of the powder, it is assumed that XCT scanning would obtain a different PSD to laser diffraction. Due to the expensive nature of XCT scanning, it was decided that only one powder would be analysed. The vanadium powder was chosen as the particle shape was irregular and would result in high contrast scans.

The vanadium powder sample was prepared in a powder-epoxy mixture in a plastic tube having an internal and external diameter of approximately 1.5 and 2.5 mm, respectively. Loose vanadium powder was mixed with Struers EpoFix resin and hardener system [116], [117] to create the powder-epoxy mixture. It is suggested by Garbonzi and Hrabe [23] that the volume fraction of powder in the mixture must not exceed 10 % to minimize powder particles from touching each other and obtain clear XCT scans. The powder-epoxy composite was mixed in weight percent using an A&D FX 1200i precision scale and a summary of the converted volume fraction can be seen in Table 10. The volume fraction of vanadium powder in the mixture was 7.4 %.

Table 10: Powder-epoxy mixing ratio and converted volume fraction

Medium	Density (g/cm^3)	Mass (g)	Mass Ratio	Volume Fraction (%)
Epofix Resin	1.11-1.14[1]	4	50	81.2
Epofix Hardener	0.94-0.98[2]	0.48	6	11.4
V Powder	6.11	2	25	7.4

[1] [116]; [2] [117]

The composite was mixed by hand for five minutes in a small container ensuring that the powder particles were well dispersed in the resin. The mixture was placed in a Buehler Cast n' Vac 1000 for two minutes to remove any bubbles in the mixture. A plastic 3 ml pipette was used to draw the mixture up and deposit it into the plastic tube, which was open at both ends. Once the mixture had exited tube, it was plugged with Prestik at the exit and left upright to cure overnight. The cured sample can be seen in Figure 19.

The XCT scanning was conducted through the CAF CT Scanning Facility at SU [64] by Ms Tshibalanganda on their Nanotom S nanoCT scanner. The scan settings are summarised in Table 11. A set of 2700 projections were captured in one full rotation of the sample, with images having 2304 x 2304 pixels. A total of 93,857 particles were identified through XCT scanning. A dataset containing the number of particles of a certain volume was exported using Volume Graphics VGStudio Max 3.4.

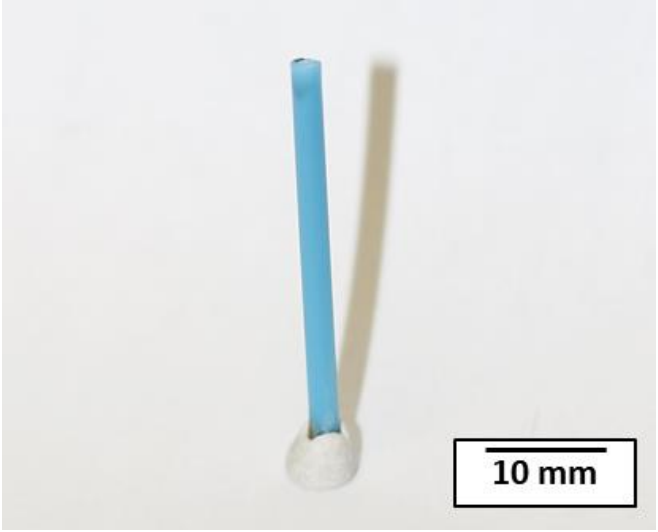

Figure 19: XCT scan sample of a powder-epoxy mixture mounted in a plastic tube

Table 11: XCT scan settings

Voltage (kV)	Current (µA)	Voxel Size (µm)	Field of View (mm)	Scan Time (hrs)
100	135	2	4.61	3

While the PSD's generated using laser diffraction and XCT scanning are both volume based, there is an important distinction that should be considered when comparing the data from the respective methods. As seen in Figure 18, laser

diffraction calculates the particle size based on the diffracted angle, assuming that the particle is spherical. In comparison, XCT scanning measures a true volume of each powder particle, and then determines an effective diameter of a spherical particle, D_E, with the same volume is calculated, based on the following relationship to the XCT volume:

$$V_{XCT} = \frac{\pi}{6} {D_E}^3 \quad (3.1).$$

The resulting plots of volume frequency percent vs. effective particle diameter and cumulative finer volume percent vs. effective particle diameter for the vanadium powder were determined from both data sets and directly compared.

3.3.7 Theoretical Density

The theoretical density is the density of the solid loose powder particles and is comparable to the full density of the solid material. The values for the as-received powders were obtained from the relevant material safety datasheet (MSDS) from the suppliers. The theoretical density for the blends was calculated using the rule of mixtures using volume fractions of the powders.

3.3.8 Skeletal Density

The skeletal density is defined as [120]

$$\rho_{sk} = \frac{m}{V_{solid} + V_{ep}} \quad (3.2)$$

where m is the mass of the powder, V_{solid} is the solid volume, and V_{ep} is the entrapped pore volume.

The mass was measured using a Kern ABT 120-5DM precision scale (0.1 mg accuracy) and the density was measured on a Quantachrome Instruments - Ultrapyc 1200e Automatic Gas Pycnometer according to ASTM B923 [104]. The pycnometer was calibrated before testing and the calibration report can be found in Appendix A.2. The pycnometer analysis parameters were kept constant for all tests, seen in

Table 12. One sample of each powder was tested with five runs and three being averaged, with the standard sample error being reported.

Table 12: Pycnometer settings

Cell Size	Target Pressure	Gas	Equilibrium Time	Flow Purge	Max Runs	Runs Averaged	Deviation Requested
Small	16 psig	N_2	Auto	1 min	5	3	0.005 %

3.3.9 Apparent Density

The AD of a metal powder is known as the ratio of the powder mass and its apparent volume. This is an indication of the packing density of the powder. It is measured using ASTM B212 [105] for free-flowing powders and ASTM B417 [106] for non-free-flowing powders.

The tests were initially conducted on the raw powders off the storage shelf without oven drying. It was noticed that the powders had poor flow characteristics and upon investigation, it was found that powders are typically oven dried prior to LPBF, as moisture tends build up on powders when stored for longer periods of time. The AD was subsequently tested on the powders that had been oven dried at 120 °C for four hours using a Gallenkamp Hot Box Oven Size One. It is known that oxidation only occurs for all powders above 200 °C [121]–[123]. Two to three tests were conducted per sample and averaged, with the standard sample error being reported. The relative AD is calculated as

$$\rho_{rel} = \frac{\rho_{app}}{\rho_{sk}} * 100\ \% \tag{3.3}$$

where ρ_{app} is the apparent density and ρ_{sk} is the skeletal density. This allows for a comparison of the packing of different powders, with a higher relative AD value indicates a denser packing. The relative AD is typically 30-60 % [21].

3.3.10 Flowability

The flowability of a powder was determined using static flow methods presented in 2.6.8. The standard Hall flowmeter for free-flowing powders was used according to ASTM B213 [69] to measure the Hall flow rate (FR_H). The Carney flowmeter for non-free-flowing powders was used according to ASTM B964 [70] to measure the Carney flow rate (FR_C). For the same reasons discussed in Section 3.3.9, all tests were performed with oven dried powder at 120 °C for four hours using a Gallenkamp Hot Box Oven Size One. Two to three runs were conducted per sample and averaged, with the standard sample error being reported.

An additional test was performed on the CP Ti powder to determine the effect of drying time on flowability. Three flowability tests were performed on samples taken from different regions of the container every hour until four hours of drying was completed. The samples were returned to the container after testing for further drying. The three tests were averaged, and the standard sample error was reported.

3.3.11 Angle of Repose

The static AoR, α, was determined using the fixed funnel method [75], illustrated in Figure 20a. The powder was passed through an appropriate funnel (either Hall or Carney) onto a flat cylindrical surface. Powders that were unable to flow freely through the relevant funnel were assisted by lightly tapping the funnel.

The AoR of the powder heap can be determined using a suitable image analysis tool, such as Microsoft PowerPoint, and Equation (3.4), illustrated in Figure 20b. A powder with a lower AoR has better flowability and is termed very free flowing, free flowing, fair to passable flow, cohesive, and very cohesive if the AoR is <30°, 30-38°, 38-45°, 45-55°, >50° respectively [124]. The AoR is calculated as

$$AoR = \tan^{-1}\left(\frac{h}{r}\right) \tag{3.4}$$

where h is the perpendicular height of the powder heap and r is the radius of the powder heap. A Canon EOS 750D camera was mounted on a tripod (Manfrotto 290 dual) level to the powder heap. The camera was fitted with a Canon 50 mm lens and was set to capture high resolution images of 72 dpi and a size of 6000 x 4000 pixels.

For the same reasons discussed in Section 3.3.9, all tests were performed with oven dried powder at 120 °C for four hours using a Gallenkamp Hot Box Oven Size One. The powder was seen to have a slightly different gradient on the left and right side, consequently, two best fit lines were plotted by eye on the image in Microsoft PowerPoint and the gradient of each line was calculated, according to Equation (3.4), and averaged with the standard sample error being reported.

3.3.12 Powder Blending Quality

Various strategies were investigated to determine whether the powder blends were mixed thoroughly enough. In Blend 1 MA, the flowability, AD and AoR were measured at incremental mixing times and for Blend 2 BE, the AD was measured.

With each blend, a roughly 50 g sample was removed from the mixing container at each time increment for testing. Once it had been tested, it was returned to the container for further mixing.

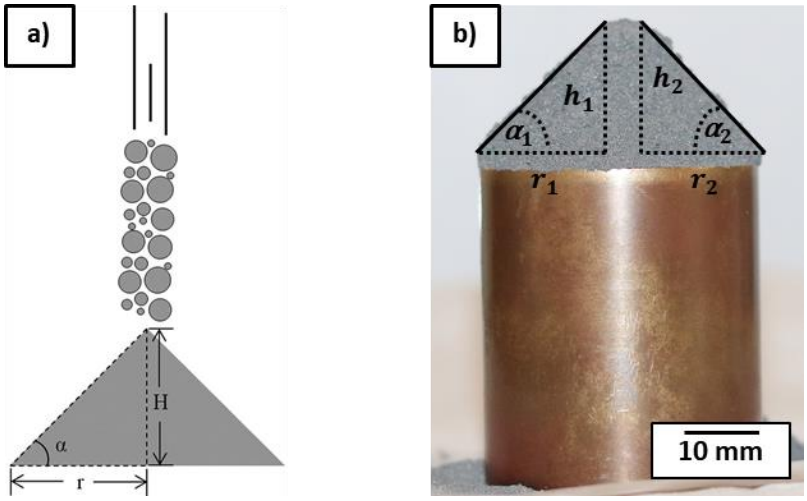

Figure 20: AoR measurement a) an illustration of the static AoR [6], and b) a schematic with the variables used in Equation (3.4)

An additional skeletal density test was performed on the final Blend 2 BE powder. Five ~10 g samples were taken from different regions in the powder blend. These values were averaged with the standard sample error being reported. In theory, the pycnometer is sensitive to slight changes in density. If the blend was adequately blended, i.e. equal distribution of the constituent powders, there would only be minor differences in the skeletal density of each sample. If an area were less dense, it would be rich with Al, and if it were denser, it would be V rich.

3.4 Spreadability Testing

A spreadability test rig was designed to mimic the recoating process of the EOSINT M280 as simply as possible. The rig layout, control and functioning are described in this section, along with the associated spreadability metrics of percent coverage, spread density and elemental distribution of spread powder.

A labelled photo of the final manufactured rig is presented in Figure 21, with the labelled CAD assembly illustrated in Figure 58 and included in Appendix C.3. The labelled photo of the 3D printed control box, which houses the majority of the electrical components is presented in Figure 23. The corresponding numbers in these images are represented in Table 13 and Table 14.

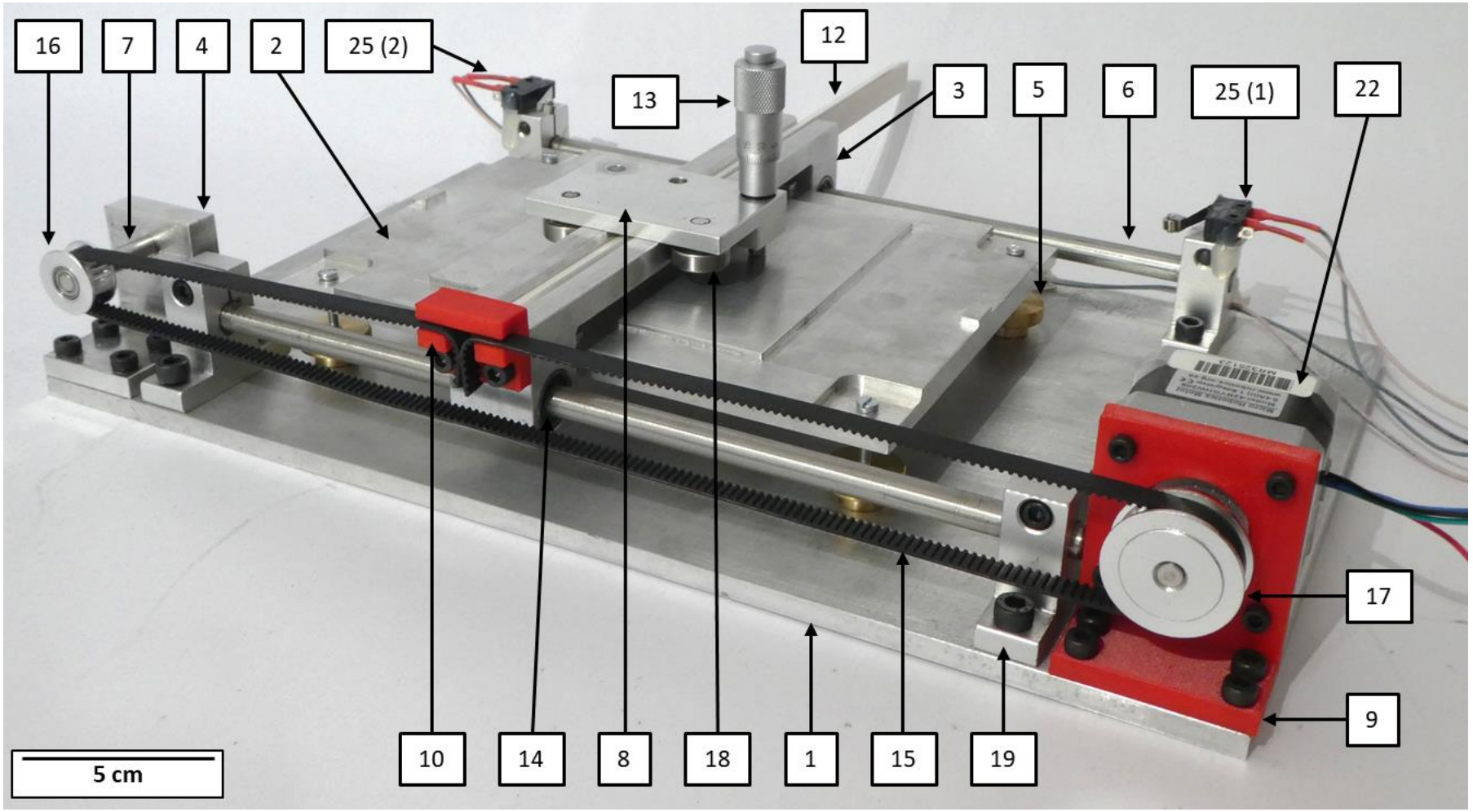

Figure 21: Labelled manufactured spreadability test rig

3.4.1 Rig Layout – Mechanical Components

The rig is a simple two-dimensional gantry comprised of predominantly aluminium and 3D printed components, having a drive system similar to that of a typical FDM 3D printer. The details of the mechanical components are summarised in Table 13.

Table 13: Summary of spreadability test rig mechanical components

Name	Qty.	Material	Supplier	Details
1. Support plate	1	Al - M82	Non-ferrous Metal Works, Cape Town	Raw material bought-out and machined at M&M workshop
2. Build plate	1			
3. Crossbeam	1			
4. Pulley mount block	1			
5. Levelling knob	4	Brass	M&M workshop, SU	Manufactured at M&M workshop
6. Guide rod	2	SS		
7. Pulley mount rod	1	SS		
8. Micrometer mount	1	Al		
9. Motor mount	1	PLA	Materials Engineering, SU	3D printed
10. Timing belt tensioner	1			
11. Electronics control box	1			
12. Recoater blade	1	Ceramic	CUT	EOSINT M280 recoater blade
13. Micrometer	1	-	RS Components, JHB	RS PRO, length: 13 mm
14. Linear bearing	2	-	Micro Robotics, Stellenbosch	LM8U, ID[4]: 8 mm
15. Timing belt	1 m	PU[3]		GT2, width: 6 mm
16. Idler pulley	1	-		GT2, bore: 5 mm
17. Timing pulley	1	-		GT2, 36T, bore: 5mm
18. Bearing	3	-		Size: 5x16x5
19. Support shaft	4	Al		SK8: 8 mm shaft

[1]Stainless steel; [2]Polylactic acid; [3]Polyurethane; [4]Inner diameter

The recoater blade of an EOSINT M280, supplied by CUT and seen in Figure 22, is mounted on a crossbeam and is driven by stepper motor and a timing belt along two guide rods. Two linear bearings have been press fit into the crossbeam to

allow low friction movement along the guide rods. The build platform has a raised 10 x 10 cm^2 area, and its height is manually adjusted using four levelling screws. The surface roughness, Ra, of the build platform was measured as 1.14 µm using a Mahr MarSurf PS 10. A total of eight measurements were taken, four parallel and four perpendicular to the spread direction.

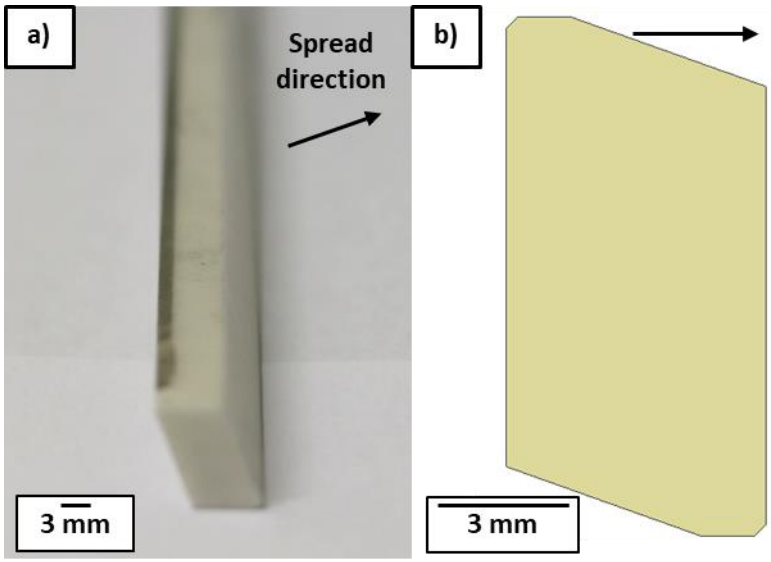

Figure 22: Spreadability test rig a) EOSINT recoater blade, b) recoater blade cross-section

3.4.2 Rig Layout – Electrical Components

The schematic of the 3D printed control box, which houses the majority of the electrical components can be seen in Figure 23. The control box was designed to cover the electrical components and minimise their interaction with the metal powders. The associated wiring diagram can be found in Appendix C.4 and the details of the electrical components are summarised in Table 14.

The Arduino microcontroller, powered by a 2-pin wall plug (12 V 2 A), integrates all the electrical components through a prototyping board. A prototyping board is essentially a flat breadboard with holes and conductive copper strips that can be soldered. It is used as the next step in the electrical prototyping process after a standard breadboard but before the use of a printed circuit board (PCB).

A stepper motor rotates with a fixed number of increments known as steps, which can be finely controlled to obtain a required rotational velocity. The stepper motor selected is similar to that used in typical FDM 3D printers with a 1.8 °/step (200

steps per rotation) and 0.28 Nm rating. It requires an external power source which is provided by the power supply unit (PSU). The PSU converts 220-240 V AC mains to 12 V 3 A DC power, through a stepper motor driver.

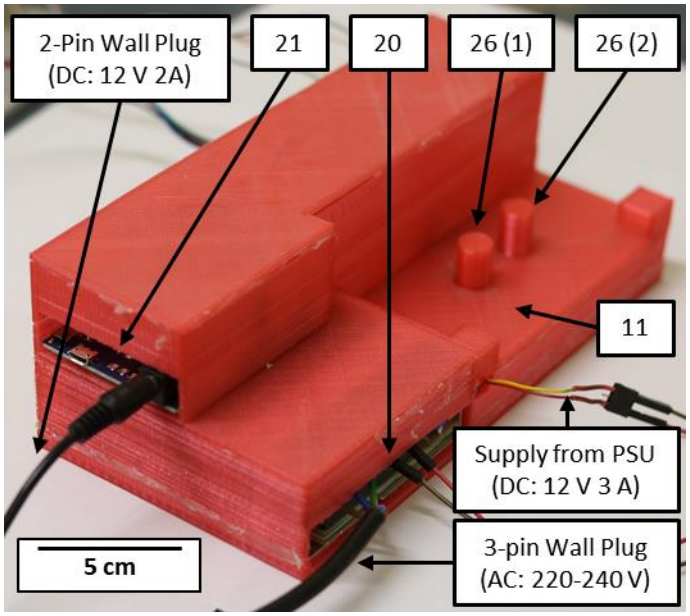

Figure 23: Spreadability test rig control box containing electrical components

Table 14: Summary of spreadability test rig electrical components

Name	Qty.	Supplier	Specification
20. Power supply unit	1	Micro Robotics, Stellenbosch	LRS Compact, 12 V 3 A 35 W
21. Arduino	1		Uno R3
22. Stepper motor	1		NEMA17, 1.8 deg/step, 0.28 Nm
23. Stepper motor driver	1		1 A - Pololu Original
24. Protoboard	1		Protoboard universal
25. Limit Switch	2		Roller lever, SPDT, 5 A
26. Button	2		Mini push button: 4-pin
27. Transistor	1	E&E department, SU	1000 µF
28. Resistors	4		10 kΩ

A stepper motor driver is used to easily interact with a stepper motor and it also protects the motor and microcontroller from overloading. A 1 A stepper motor driver is sufficient as the stepper motor is rated at 400 mA. The stepper motor driver can easily micro-step the motor for smoother operation, and the micro-step

resolutions available are full, half, quarter, eighth, and sixteenth. Details of the stepper motor driver and the micro-stepping can be found in Appendix C.5 The limit switches are simple snap action roller levers which have been glued onto the guide rod support shafts so that they are triggered by the crossbeam at the far ends of the rig. These are used as automatic end stops at the limits of the rigs motion.

3.4.3 Rig Control and Functioning

The rig is electronically controlled through an Arduino Uno microcontroller and a two-button setup, seen in Figure 23. When button 1 is pressed, the crossbeam, which is housing the recoater blade, is moved backwards at 150 mm/s to the motor side of the rig until the crossbeam triggers the limit switch 1, Figure 21. Similarly, when button 2 is pressed, the crossbeam moves forward at 150 mm/s until limit switch 2 is triggered. When the limit switch is triggered, the crossbeam moves a few millimetres in the opposite direction at 50 mm/s to release the limit switch. This was done to ensure that neither of the limit switches were triggered while the crossbeam was at rest. The build plate can be easily removed while the crossbeam is in the starting position (after pressing button 1) to allow for the easy removal of metal powder from the build plate.

The stepper motor driver was set to run in a quarter step resolution, which provides 800 steps per rotation, as each step, of the rated 200 steps, is divided into four separate steps. To set the linear velocity of the recoater blade, the rotational velocity of the motor must be adjusted to obtain the required linear velocity. The rotational velocity of the motor is governed by a delay, in microseconds, per rotational step in the Arduino code, Section C.1, named the “delay_speed.” Knowing the number of steps per rotation as well as the pitch and number of teeth of the timing belt pulley, the value for the “delay_speed” can be easily obtained. The linear spreading velocity was set as 150 mm/s, which translates to a “delay_speed” of 300 µs, and the calculation is shown in Section C.2.

The test rig was initially designed to be levelled using the manual levelling screws and a micrometer fixed to the top of the crossbeam. During testing the micrometer was deemed unsuitable as it only has a resolution of 10 µm and was difficult to determine whether it was in contact with the build plate. The alternative levelling strategy was to utilise a feeler gauge. A feeler gauge is a measuring tool used to measure small gaps between two objects.

The levelling procedure is as follows:

1. Ensure the rig is switched off. Notes: the stepper motor has a holding torque while powered and will prevent the crossbeam from being moved.
2. Move the crossbeam by hand to the starting edge of the 10 x 10 cm^2 build plate. Notes: ensure that there is clearance between the recoater blade and the build plate to avoid contact.
3. Place the appropriate feeler gauge between the recoater and the build plate.
4. Carefully raise the build plate by rotating the two levelling screws on the starting edge of the build plate. Each screw must be adjusted incrementally while checking the gap with the feeler gauge. Notes: The feeler gauge must be able to move freely but have a very slight resistance.
5. Steps 2-5 must be repeated for the far side of the build plate using the remaining two levelling screws.

3.4.4 Percent Coverage

The percent coverage [45] of the powders over the build plate was characterised using a custom designed spreadability test rig in a manner similar to that presented in 2.7.3. The design and functionality of the custom designed rig is outlined in Section 3.4. To determine the percent coverage, a specified mass of powder is deposited along the starting edge of the build platform. The minimum mass of powder, m, that is required is calculated according to Equation (2.3), using the full area of the build plate as the maximum achievable spread area and the layer thickness that was set for the test. The recoater blade is moved over the build plate at the set layer height and at a set recoater speed, and the percent coverage is determined by quantitatively analysing the powder coverage the build plate from an overhead image.

The experimental setup can be seen in Figure 24. A Canon EOS 750D camera was mounted on a Manfrotto 290 dual tripod facing downwards and directly overhead the build plate of the spreadability test rig. The screen of the camera was angled perpendicular to the camera viewing angle for the ease of image reviewing by the operator. The camera was fitted with a Canon 50 mm lens and was set to capture high resolution images of 72 dpi and a size of 6000 x 4000 pixels.

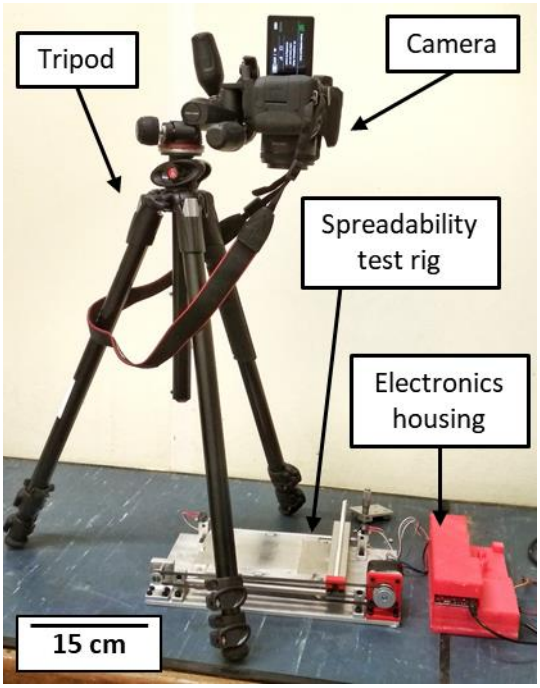

Figure 24: Spreadability experimental setup

The sequential stages of the image analysis are shown in Figure 25. The raised square 10 x 10 cm^2 build plate free of powder is shown in Figure 25a. The bed is levelled, and the layer height is set using a feeler gauge while the rig is unplugged. The rig is then plugged in and set to the starting position. Powder of mass, m, is deposited by hand using weighing paper, as evenly as possible, on the starting edge of the build plate, Figure 25b. The recoater blade is moved across the build plate at the set layer height and the speed that has been coded in the Arduino, Appendix C.1. This variable is named "delay_speed" and translates to a recoater speed of 150 mm/s, which all tests were conducted at. 150 mm/s was selected as this is the typical recoater speed used at the CRPM on their EOS M280 machine. Furthermore, to reduce the experimental matrix, it was decided that the recoater speed would remain fixed while maintaining the layer height as the independent variable. An image of the powder spread over the build plate is then captured, Figure 25c.

The image processing was completed using MATLAB and the Windows Photos application. The MATLAB code used for the image processing can be found in Appendix C.6. The image was first converted to grayscale in MATLAB and resaved, Figure 25d, then cropped and rotated using the Windows Photos application and resaved, Figure 25e. This image was finally converted to a binary image, Figure 25f,

in MATLAB. The image thresholding was image specific, with most cases using a global image threshold through Otsu's method [96]. When a poor fit was observed, local adaptive image thresholding was employed. The sensitivity of this threshold was adjusted through trial and error until a good fit was observed. The percent coverage is calculated as

$$\% \text{ Coverage} = \frac{N_{black}}{N_{total}} * 100\ \% \tag{3.5}$$

where N_{black} is the number of black pixels and N_{total} is the number of total pixels in the binary image.

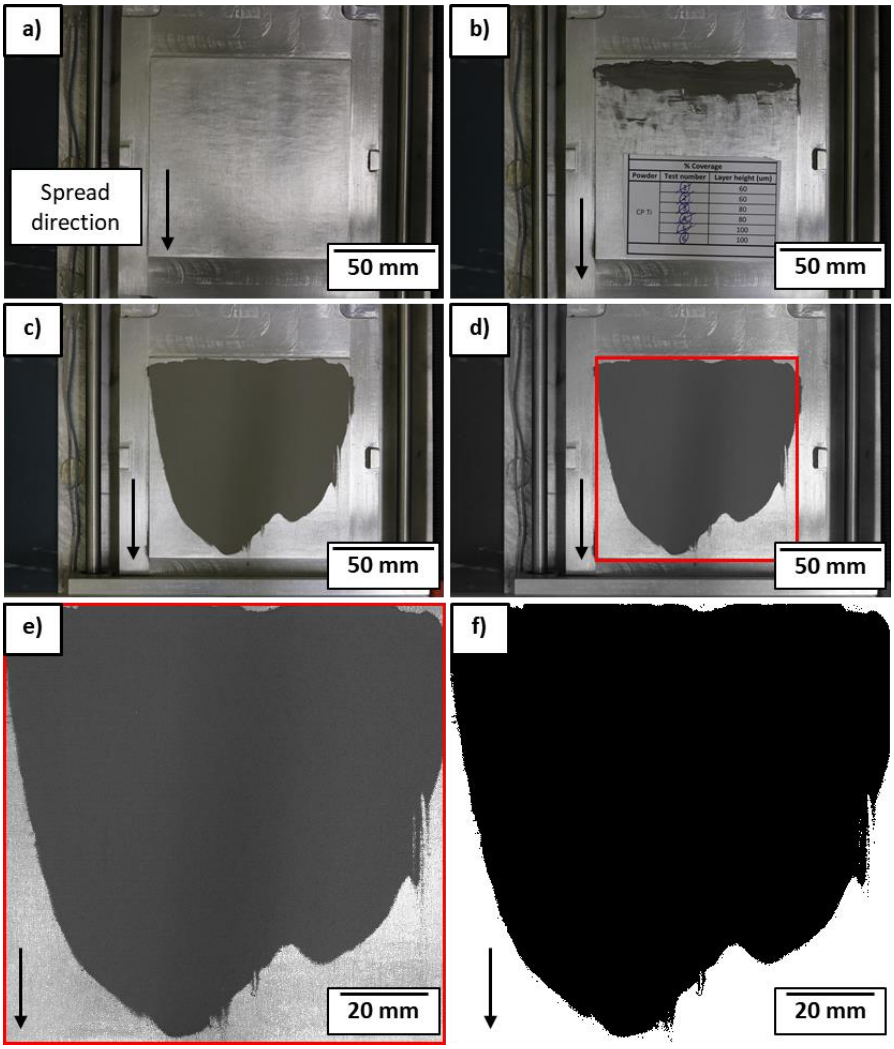

Figure 25: Sequential analysis of percent coverage showing the a) clean build plate, b) manually deposited powder, c) spread powder layer, d) converted grayscale image, e) cropped and rotated image, f) binary converted image

Two tests were conducted per powder and averaged, with the standard sample error being reported. The tests were conducted on all the powders, with no oven drying. Some powders performed particularly poorly, and it was decided to test the effect of powder drying. Subsequent testing was performed on three powders, namely, the PA Ti-6Al-4V, Blend 1 MA, and Blend 2 BE. These powders were dried at 120 °C for four hours using a Gallenkamp Hot Box Oven Size One prior to testing.

3.4.5 Spread Density

The spread density was determined by placing powder in excess of mass, m, at the start of the build platform. This was about double the mass calculated according to the minimum mass parameters, defined in 3.4.4. The recoater blade was moved over the build plate, spreading the powder at a set layer height and at a set recoater speed over the build plate. The same levelling process and recoater speed was used when obtaining the percent coverage. Due to the excess powder, it is assumed that there should be close to 100 % coverage of the build plate.

The build plate was designed to be easily removed at the four levelling points. So that the excess powder that had fallen off the side of the raised build plate, seen in Figure 26a, could be brushed away while the powder remaining on the build pate, seen in Figure 26b, could then be brushed onto a scale and weighed. The spread density, ρ_s, is the density of the powder in the spread volume, assuming 100 % coverage, calculated as

$$\rho_s = \frac{m_s}{At} \tag{3.6}$$

where A and t are defined similarly to 3.4.4, and m_s is the mass of the powder that remained on the build plate. The tests were conducted on all the powders without being dried (directly off the storage shelf). Two tests were conducted per powder and averaged, with the standard sample error being reported. The spread density was converted to a relative spread density, normalised to the skeletal density, to be compared with the relative AD.

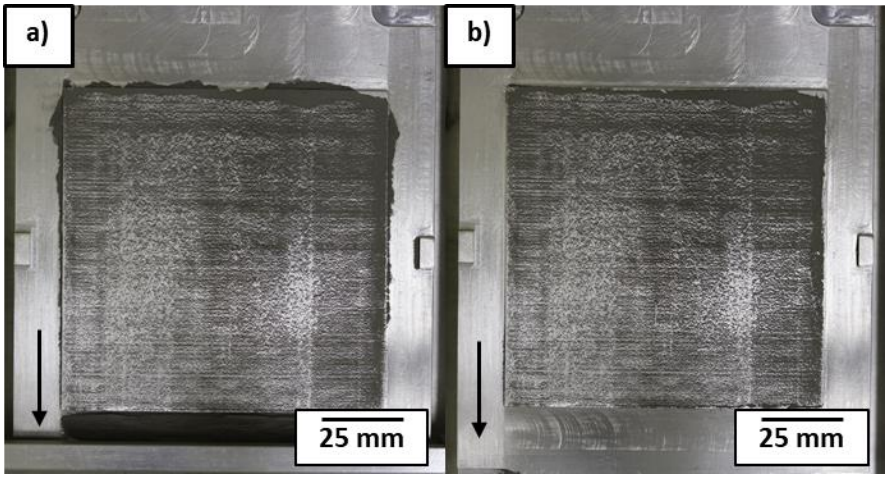

Figure 26: Spread density measurement with a) excess powder and b) excess powder removed

3.4.6 Elemental Distribution of Spread Powder

SEM/EDS analysis was used to quantitatively determine the distribution of the individual powders in the powder blends once they had been spread on the build plate. The aim of this was to determine the weight percent of powders in the blends and whether the alloying elements were well distributed on the build plate once spread. A single layer of powder was spread with a layer thickness of 100 µm using the spreadability test rig. An aluminium pin stub with double sided carbon tape was mounted in a custom stub holder, with a grub screw to hold it in place, and pressed perpendicularly onto the powder layer. This was repeated at three locations for both Blend 1 MA and Blend 2 BE, as seen in Figure 27.

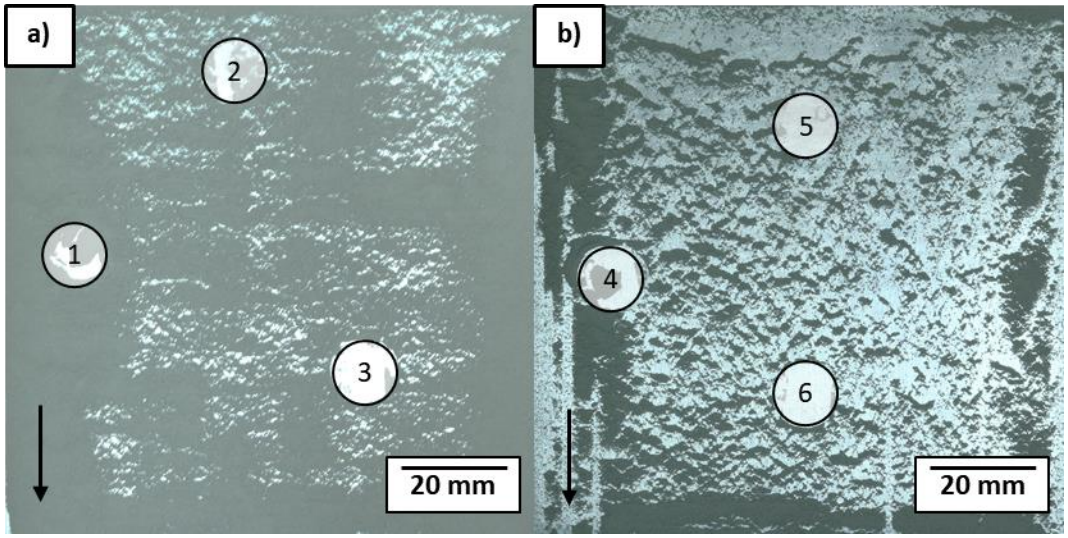

Figure 27: Powder blending distribution at three locations of a single spread layer of 100 µm of a) Blend 1 MA, b) Blend 2 BE

3.5 Direct Metal Laser Sintering

As mentioned earlier in the report, the DMLS® of the blends was conducted at CUT by an MTech (Mechanical Engineering) student, Mr. Ramosena. The powder blends were sent to CUT from SU for printing on their EOSINT M280 DMLS® printer. DMLS® machines come loaded with pre-set process parameters for specific powders, as a result from fine tuning by the manufacturer. When considering novel blends, their own set of process parameters must be determined. This is typically done by printing an array of single tracks with varying process parameters of scanning speed and laser power, resulting in varying linear energy density. These tracks are produced by depositing a single powder layer on the substrate and laser etching short individual lines.

The single tracks are then analysed geometrically using an OM to determine the track penetration depth, width, height, and continuity. The track width and continuity are determined from an overhead image of the tracks and the track height and penetration depth are measured by analysing a wire-cut cross-section of the single tracks. An initial study was performed by Ramosena *et al.* [16] on the powder characteristics and single tracks of Blend 1 MA. Based on these findings, the process is iterated by fine tuning the process parameters with each step. This is a three-stage process of single tracks, single/double layers, and small 3D parts.

4 Results and Discussion

The results and discussion of all testing, conducted according to the procedures set out in Section 3, are reported in this section. Additional results have been placed in the appendix due to space limitations.

4.1 Chemical Analysis

The chemical analysis of the individual powders is presented in Table 15. Both Blend 1 MA and Blend 2 BE are within the grade 5 Ti-6Al-4V chemical composition requirements of Table 3.

Table 15: Chemical analysis of individual loose powders

	Element (wt %)					Calculated (wt %)	
	PA Ti-6Al-4V[1]	CP Ti	MA	Al[2]	V[3]	Blend 1 MA	Blend 2 BE
Al	5.9	<0.1	54.8	99.8	9 (ppm)	5.57	6.08
V	3.9	<0.1	43.4	-	>99.99	4.43	4.09
Fe	0.03	0.12	0.64	0.1	<10 (ppm)	0.17	0.11
C	0.08	-	-	-	-	-	-
O	0.16	165 (ppm)	0.18	-	-	0.03	<0.01
N	0.01	381 (ppm)	21 (ppm)	-	-	345 (ppm)	<0.01
H	<0.01	-	-	-	-	-	-
Ti	89.71	99.3	<0.1	-	<10 (ppm)	89.38	89.59
Other	-	-	-	0.1	<381 (ppm)		<0.11

[1]AP&C; [2]Valimet; [3]Alfa Aesar

4.2 Powder Crystal Structure

The powder crystal structure and the origin of the CIFs are summarised in Table 16. The XRD patterns and the dimensions of the unit cells are seen in Figure 29 and Figure 28, respectively. The PA Ti-6Al-4V consisted purely of HCP α' martensite phase. Both α and α' phases are indistinguishable by XRD as they both consist of HCP structures and have the same unit cell dimensions [125], however, it was concluded that α' martensite phase was present due to the high cooling rate of the plasma atomisation process.

The CP Ti consisted purely of HCP alpha Ti phase, the MA consisted of both monoclinic Al_8V_5 and tetragonal Al_3V, the Al was comprised of pure face centred cubic (FCC) Al, and the V consisted purely of BCC V. These results indicate that all the powders contained the phases that were expected according to their as-supplied specifications.

Table 16: Powder crystal structure and CIF origin

Powder	Crystal Structure	CIF Origin
PA Ti-6Al-4V	HCP	AtomWork[1]
CP Ti	HCP	COD[2]
60Al-40V MA	monoclinic Al_8V_5 and tetragonal Al_3V	Materials Project[3]
Al	FCC	COD
V	BCC	COD

[1][115]; [2]Crystallographic Open Database [109]–[114]; [3][108]

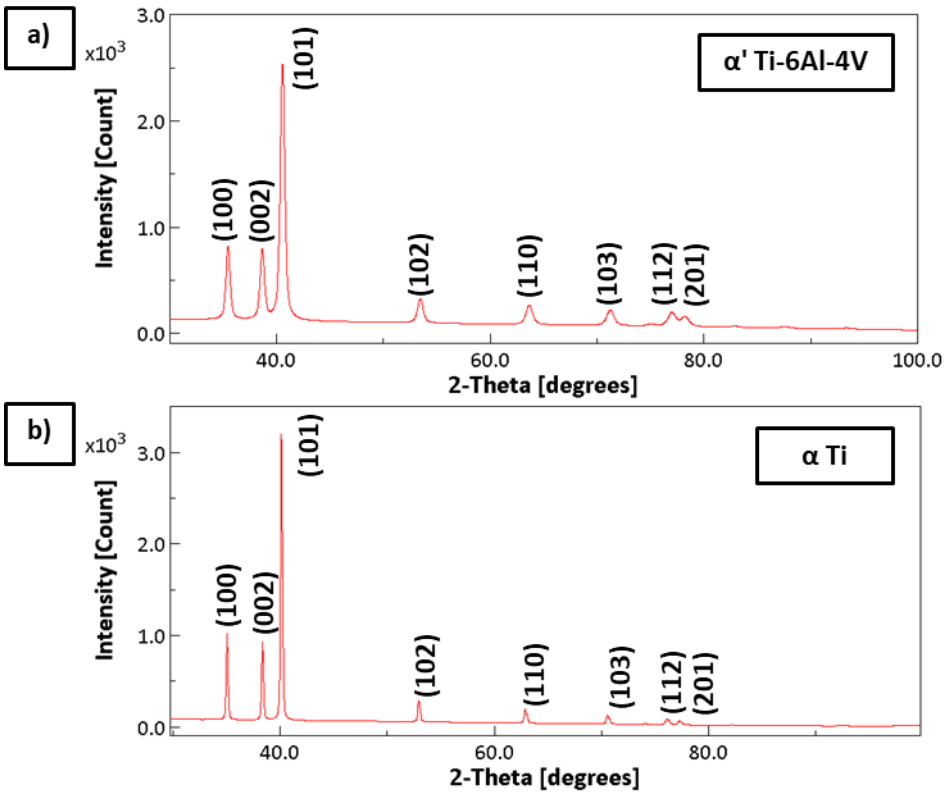

Figure 28: XRD patterns of a) PA Ti-6Al-4V and b) CP Ti powder

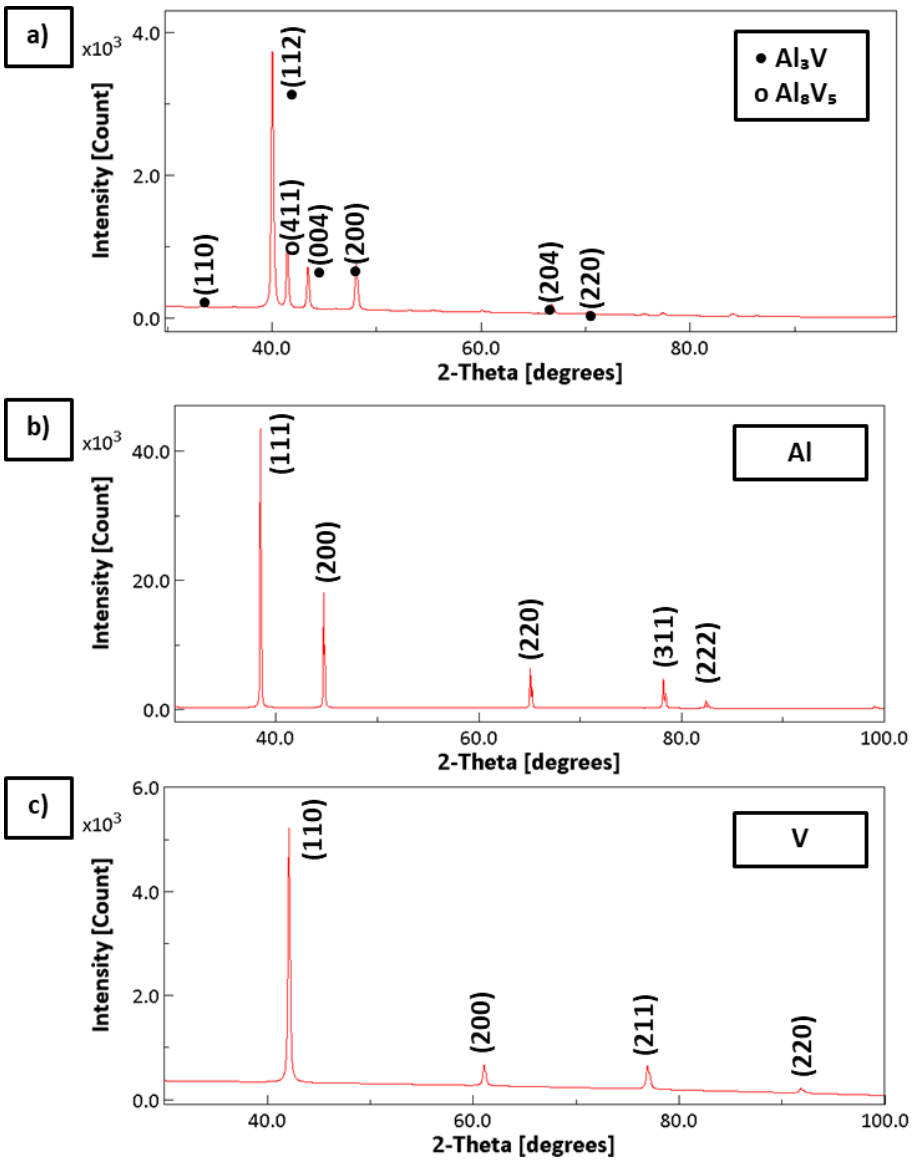

Figure 29: XRD patterns of a) MA, b) Al, and c) V powder

4.3 Powder Microstructure

The powder microstructures of the raw powders are presented in Figure 30. Cross-sectional images were taken of the powder particles before and after etching. An entrapped pore in a PA Ti-6Al-4V powder particle can be seen in Figure 30a and the powder consisted of an acicular α' martensitic structure, Figure 30b. The CP Ti was seen to have longitudinal grains, Figure 30d, the MA had a unidirectional dendritic microstructure, Figure 30f, and the microstructure of the Al and V was difficult to identify due to a poor etching procedure and limitations of the OM, which may have been rectified by SEM imaging.

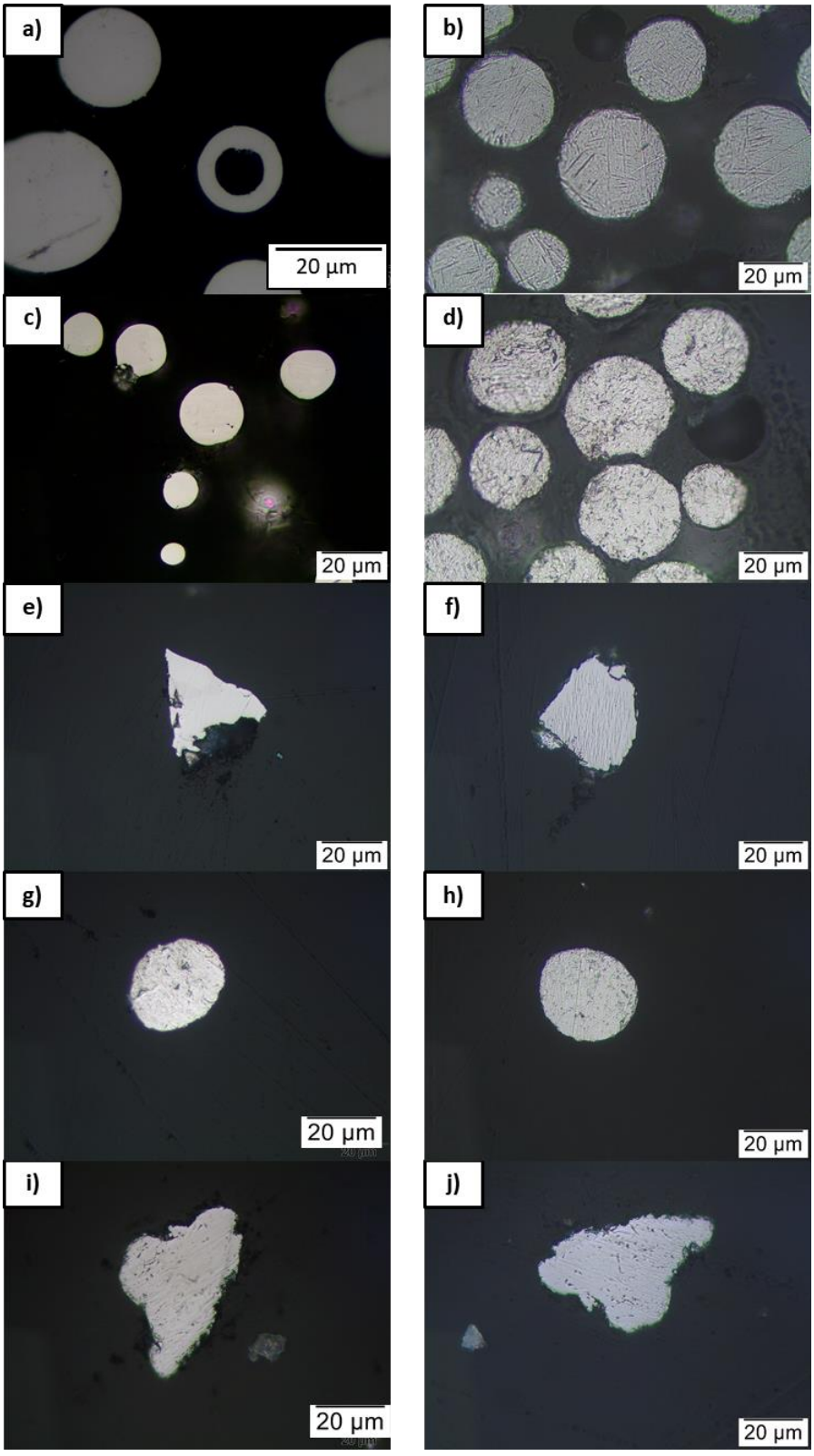

Figure 30: Powder microstructure of unetched (left) and etched (right) of a-b) PA Ti-6Al-4V, c-d) CP Ti, and e-f) MA powder g-h) Al and i-j) V powder

4.4 Morphology and Elemental Distribution

The powder morphology of the powders are presented in Figure 49 to Figure 55, Appendix B.1, and the shape of each powder is listed in Table 17. The PA Ti-6Al-4V and CP Ti powder, Figure 49 and Figure 50 respectively, are highly spherical with small sub-grains present on the surface, and with very few other surface irregularities. These features are characteristic of the plasma atomisation process and are considered high quality for use in AM.

Table 17: Powder morphology

Powder		Shape
Raw Powders	PA Ti-6Al-4V	Highly spherical
	CP Ti	Highly spherical
	MA	Sharp irregular angular
	Al	Irregular spherical
	V	Round irregular angular
Blend 1 MA	CP Ti-10 MA	Spherical and sharp irregular angular
Blend 2 BE	CP Ti-6Al-4V	Spherical, irregular spherical, and round irregular angular

The MA powder, Figure 51, had an irregular angular structure with very sharp edges. There was a significant presence of sub-micron particles which were likely to have flaked off during the ball-milling process. The shape and presence of sub-micron powder particles makes this powder unfavourable for standalone use in AM. The gas-atomised Al, Figure 52, consisted of primarily nearly spherical particles with a rough textured surface. There was a significant presence of irregular and elongated particles as well as sub-micron particles. The V powder, Figure 53, had a shape somewhat similar to that of the MA, having an irregular angular shape but with rounded edges.

The Blend 1 MA, Figure 54, displays a well homogenised distribution of MA and CP Ti powder particles. The main point to highlight is that there was no clumping of the MA particles and almost all the individual particles were surrounded by CP Ti particles. At high magnification, Figure 54c indicates the presence of fine MA agglomerates on the surface of a CP Ti particle due to electrostatic forces and weak van der Waals forces present during the powder blending process [18]. This can also be attributed to the brittle nature of the MA which may have led to additional flaking during the blending process. Blend 2 BE, Figure 55, displays

elemental CP Ti, Al and V powder being well distributed. The CP Ti is clearly differentiated from the Al and V powder particles, but the Al and V have somewhat similar morphologies and it is not necessarily clear which is which. To identify the particles and distribution clearly, subsequent EDS maps were processed.

EDS maps of the PA Ti-6Al-4V, and the two blends are presented in Figure 31 and Figure 32, respectively. The advantage of an EDS map is that qualitative images of the distribution of the individual elements can be seen clearly by having different colours as well as individual elemental maps. Quantitative data may also be obtained to indicate the elemental composition in the mapped area, in weight percent. Due to the standard mounting procedure for SEM/EDS of powders, covered in Section 3.3.4, quantitative data has been excluded from this section due to disruption of the powders mainly due to the pouring and blowing off of loose powders.

These EDS maps showcase the differences between PA, MA, and elemental powder particles. Figure 31 clearly shows individual PA Ti-6Al-4V powder particles, indicated by the combination of all three elements superimposed on each other in one particle. Figure 32a-d show the MA powder blend where pure Ti powder particles are clearly distinguished from the MA powder particles (showing a combination Al and V in the maps). Figure 32e-h shows the BE powder blend where the particles of three separate pure elemental powders, Ti, Al and V, are clearly distinguished.

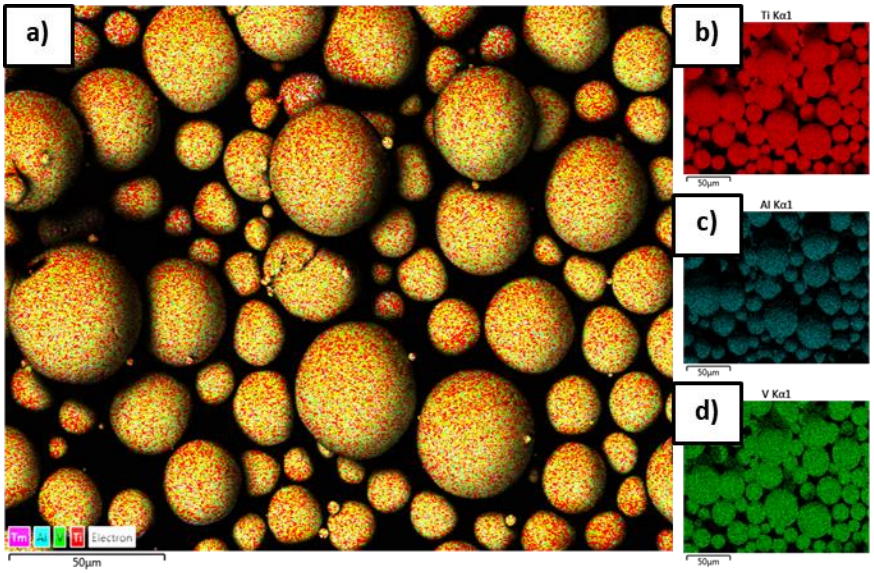

Figure 31: EDS map of a) PA Ti-6Al-4V with individual elements b) Ti, c) Al, d) V

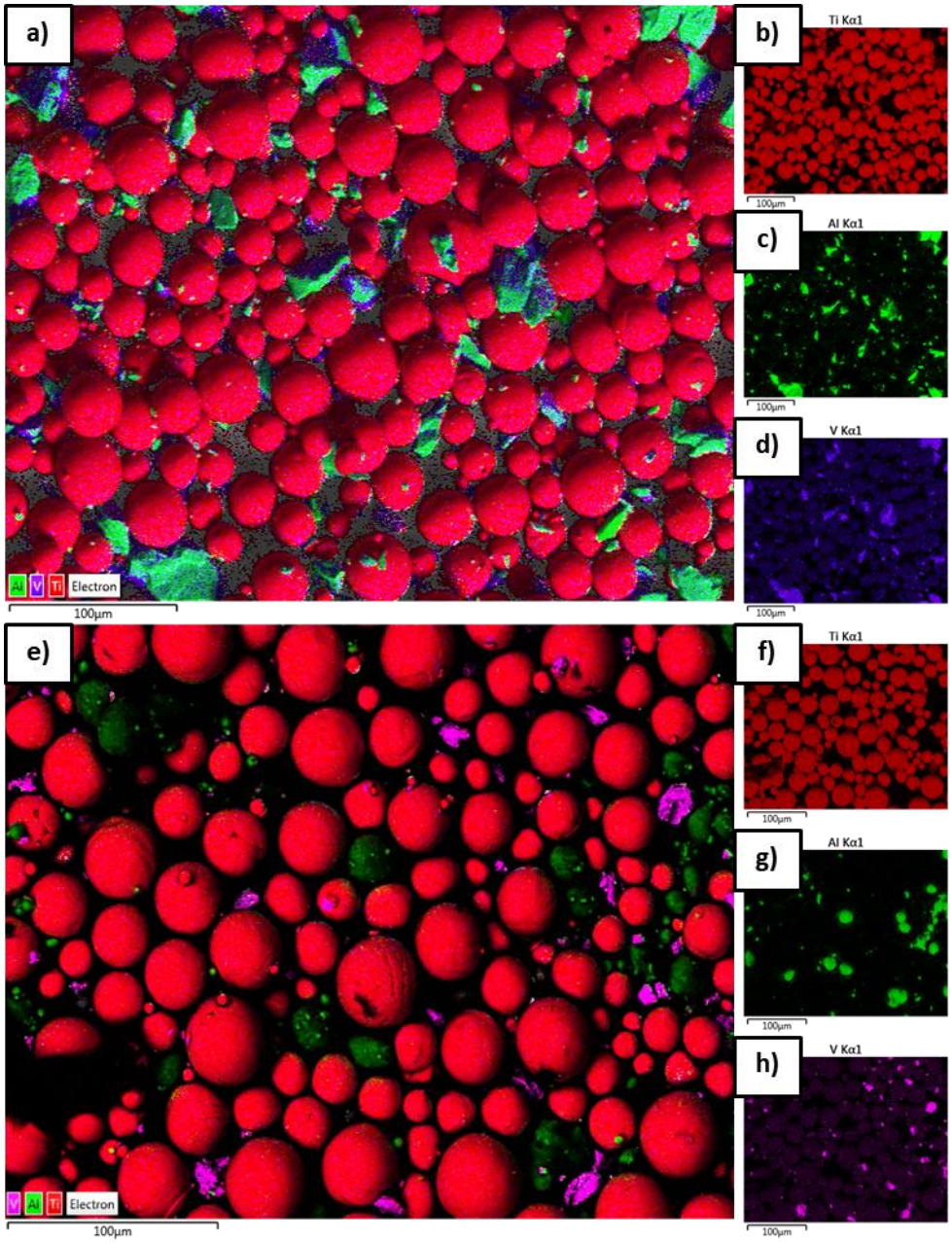

Figure 32: EDS map of a) Blend 1 MA and e) Blend 2 BE with individual elements b, f) Ti, c,g) Al, and d, h) V

4.5 Particle Size Distribution

The PSD of all the powders was determined using laser diffraction. XCT scanning was performed solely on the V powder and the results of both testing methods have been outlined in this section.

4.5.1 Laser Diffraction

The PSD of the loose powders by volume percent versus particle diameter using laser diffraction, can be seen in Figure 33. The CP Ti, PA Ti-6Al-4V powder and the powder blends have a typical Gaussian distribution. The MA and Al powders have a broad unimodal distribution, and the V powder has a broad bimodal distribution.

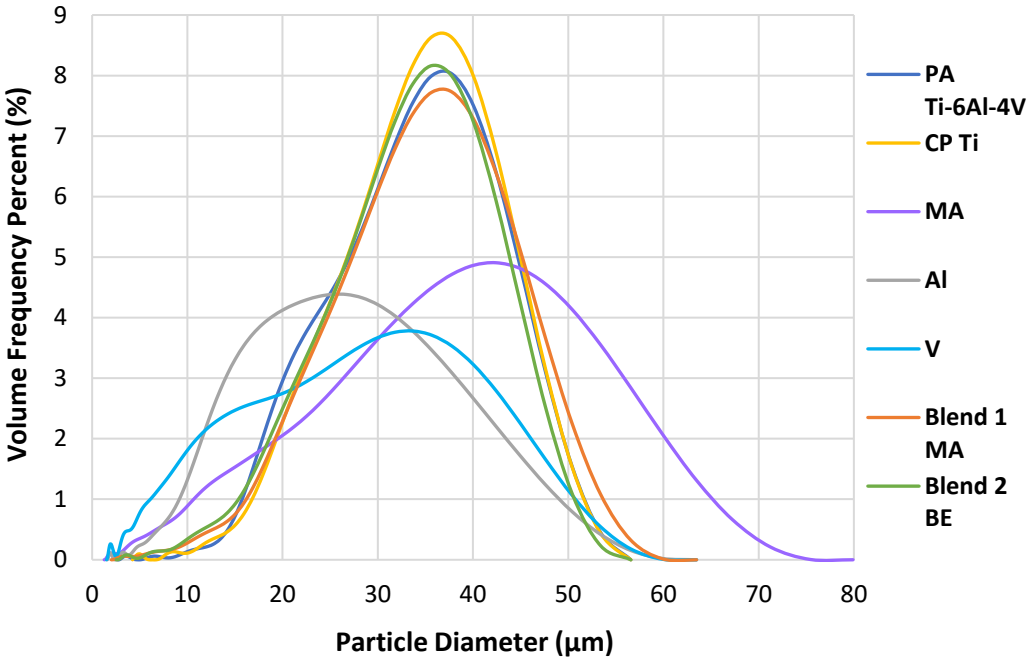

Figure 33: Volume frequency percent of loose powders using laser diffraction

The cumulative finer volume percent versus particle diameter of loose powders, can be seen in Figure 34. It is clear from this that the Al and V powders have a large number of smaller particles and the MA powder has a large number of both smaller and larger particles.

The distribution points of D10, D50 and D90, as well as the span and average particle size of the loose powders is shown in Table 18. All powders have a D90 less than 45 µm, except the MA powder, which had a D90 of 52.4 µm. The MA, Al and V powders had larger span values with the CP Ti having the lowest span value. Low span values are a sign of a narrow volume frequency percent curve, Figure 33, and a steep gradient of the cumulative finer volume percent curve, Figure 34. The demand in industry is for powders having a PSD in the 15-45 µm range [61].

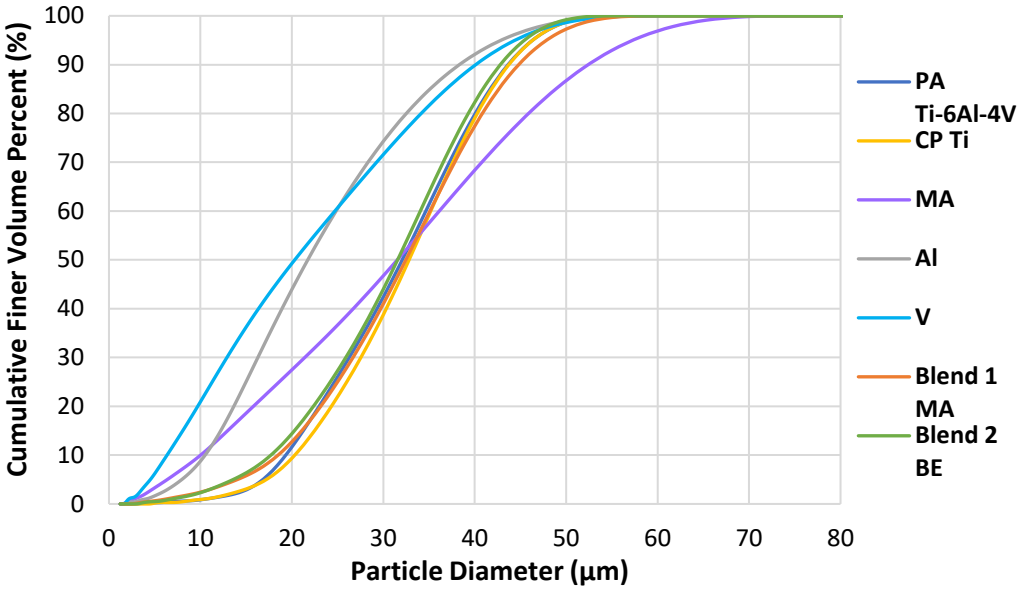

Figure 34: Cumulative finer volume percent of loose powders using laser diffraction

Table 18: Cumulative volume percent finer and average particle size of the loose powders

Powder	D10 (µm)	D50 (µm)	D90 (µm)	Span	Average Particle Size (µm)
PA Ti-6Al-4V	19.33	32.07	43.64	0.76	31.66 ± 0.05
CP Ti	20.32	32.81	43.72	0.71	32.31 ± 0.03
MA	10.02	31.53	52.40	1.34	31.38 ± 0.09
Al	10.51	21.74	38.32	1.28	23.18 ± 0.16
V	6.35	20.31	40.10	1.66	21.99 ± 0.16
Blend 1 MA	18.49	32.47	44.79	0.81	31.91 ± 0.02
Blend 2 BE	17.71	31.56	42.80	0.79	30.77 ± 0.02

4.5.2 X-ray Computed Tomography Scanning

The XCT scanning images can be seen in Appendix E. An isometric view of a single slice of the sample, with a colour bar indicating the relevant powder particle size, generated in Volume Graphics myVGL software, is seen in Figure 72. A 3D volume representation of the sample, colour coded similarly, at various magnifications is depicted in Figure 73.

The graph of the comparison of the volume frequency percent between laser diffraction and XCT scanning of the vanadium powder can be seen in Figure 35. The laser diffraction resulted in a broad bimodal distribution with the XCT scanning

resulting in a narrower multimodal distribution. The laser diffraction identified all particles having a diameter less than 64 µm, whereas the XCT scanning resulted in all particles having an effective particle diameter of less than 48 µm.

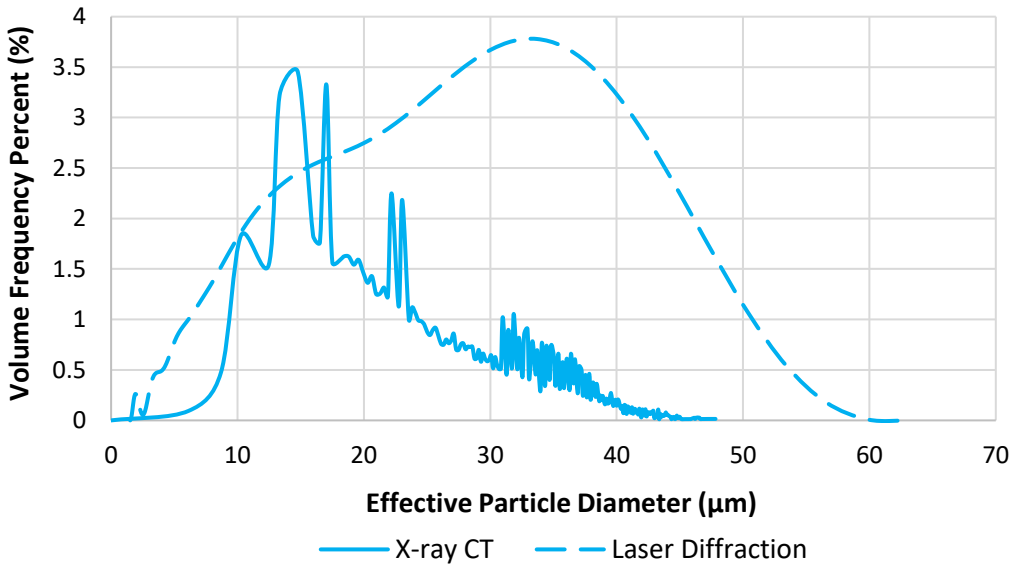

Figure 35: Volume frequency percent of V powder measured using laser diffraction and XCT scanning

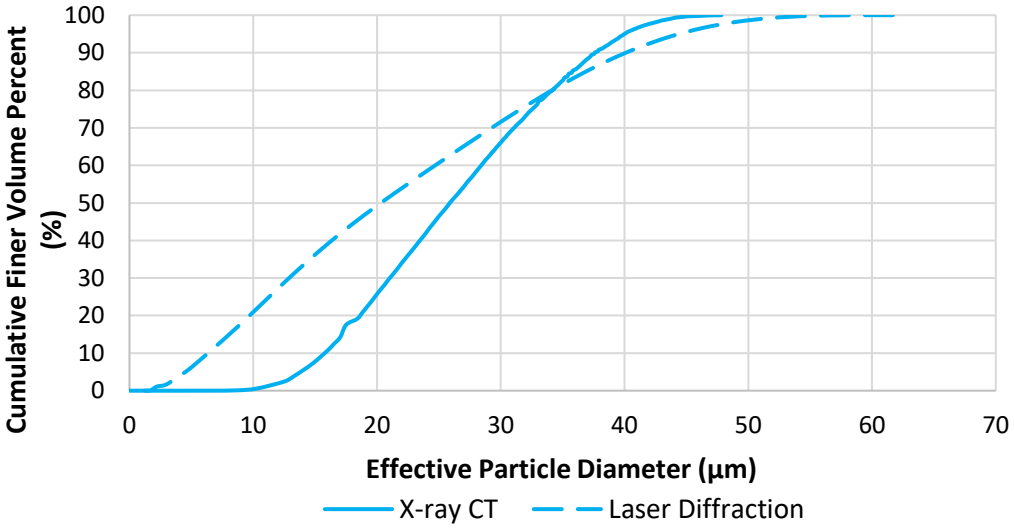

Figure 36: Cumulative finer volume percent of V powder measured using laser diffraction and XCT scanning

The cumulative finer volume percent of the two methods can be seen in Figure 36. The distribution points of D10, D50 and D90, as well as the span and average

particle size of the loose powders is shown in Table 19. Both methods obtained a similar average particle size but the span XCT scanning was half that of laser diffraction.

Table 19: Cumulative volume percent finer and average particle size of V powder using different PSD methods

Method	D10 (µm)	D50 (µm)	D90 (µm)	Span	Average Particle Size (µm)
Laser diffraction	6.35	20.31	40.10	1.66	21.99 ± 0.16
XCT scanning	15.77	25.89	37.61	0.84	20.00

Figure 37 indicates the number of vanadium powder particles with a given sphericity determined through XCT scanning. The powder particles have a low sphericity with the average sphericity being 0.62. This supports the explanation of the laser diffraction measurement errors described above.

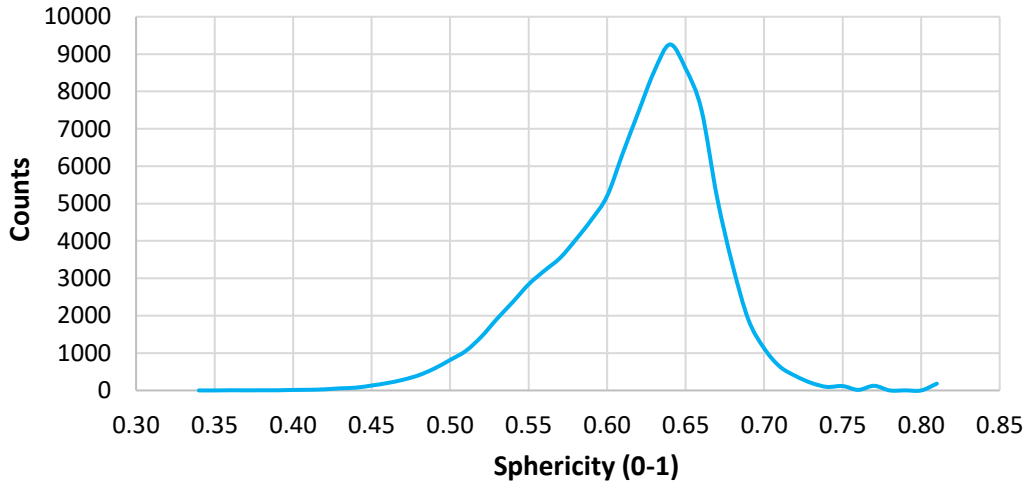

Figure 37: Sphericity of V powder particles from XCT scanning

From these results, laser diffraction has overestimated the particle sizes of the vanadium powder on average. This is likely due to the error induced by laser diffraction assuming particles to be spherical. This is illustrated in Figure 18 where, firstly, the same powder particle can be determined as larger or smaller when viewed in different orientations. Secondly, Figure 18a illustrates that irregular particles may be assumed to have a much larger particle diameter and subsequent particle volume. Thirdly, only the outline of the particle shape will be considered, which disregards surface voids or irregularities.

4.6 Theoretical Density

The theoretical density of the raw powders is reported in Table 20. The MA is given as a range by the supplier as each powder particle may have a variable ratio of aluminium and vanadium, out of the 60Al-40V specification. This range translates to the range calculated in Blend 1 MA. Blend 2 BE has a calculated value slightly below that of the PA Ti-6Al-4V.

Table 20: Theoretical density of raw powders

Powder		Theoretical Density (g/cm^3)	Source	Supplier
Raw Powders	PA Ti-6Al-4V	4.43	MSDS	AP & C
	CP Ti	4.5	MSDS	AP & C
	MA	3.94 - 5.61	MSDS	Reading Alloys
	Al	2.7	MSDS	Valimet
	V	6.11	MSDS	Alfa Aesar
Blend 1 MA	CP Ti-10 MA	4.44 – 4.59	Calc.	Blended at SU
Blend 2 BE	CP Ti-6Al-4V	4.37	Calc.	Blended at SU

4.7 Skeletal Density

The skeletal densities of the powders are reported in Table 21. The skeletal density of the PA Ti-6Al-4V, CP Ti, and Al powders were almost identical to the theoretical densities specified. The MA powder was found to be lower than the theoretical density, with the V and Blend 2 BE powder being higher. The Blend 1 MA was in the expected range of the theoretical density.

Table 21: Skeletal density results of loose powders

Powder		Mass (g)	Volume (cm^3)	Skeletal Density (g/cm^3)
Raw Powders	PA Ti-6Al-4V	9.17	2.07 ± 0.00	4.43 ± 0.00
	CP Ti	10.95	2.42 ± 0.00	4.53 ± 0.00
	MA	3.05	0.81 ± 0.00	3.75 ± 0.01
	Al	4.01	1.47 ± 0.01	2.73 ± 0.02
	V	3.82	0.60 ± 0.00	6.37 ± 0.01
Blend 1 MA	CP Ti-10 MA	7.03	1.58 ± 0.0	4.45 ± 0.00
Blend 2 BE	CP Ti-6Al-4V	7.19	1.62 ± 0.00	4.44 ± 0.00

4.8 Apparent Density

The apparent densities of the dried loose powders as well as their relative apparent densities are reported in Table 22.

Table 22: Apparent density of dried loose powders

Powder		AD (g/cm^3)	Relative AD (%)
Raw Powders	PA Ti-6Al-4V	2.44 ± 0.01	55.1 ± 0.00
	CP Ti	2.56 ± 0.00	56.5 ± 0.00
	MA	1.26 ± 0.00	33.6 ± 0.00
	Al	1.08 ± 0.01	39.6 ± 0.01
	V	2.02 ± 0.04	31.7 ± 0.01
Blend 1 MA	CP Ti-10 MA	2.26 ± 0.03	50.8 ± 0.01
Blend 2 BE	CP Ti-6Al-4V	2.32 ± 0.03	52.3 ± 0.01

The relative AD of the CP Ti and PA Ti-6Al-4V powders are highest, indicating the densest packing out of all the powders. This is expected as the powder particles are highly spherical and uniform in nature which is favourable to better packing [7], [22]. The MA, Al, and V powders had a low relative density which can be attributed to their irregular shapes. Irregular shapes typically cluster which prevents all voids from being filled [5]. Had the tapped densities been determined for these irregular shaped powders, their relative densities are likely to have improved considerably. Both Blend 1 MA and Blend 2 BE had slightly lower apparent densities when compared to the PA Ti-6Al-4V, this is likely due to the interparticle friction from the irregular shaped alloying powders in the blends.

4.9 Flowability

The FR_H and the FR_C of the dried loose powders are reported in Table 23.

The CP Ti was the only powder able to flow through the Hall flowmeter and it has been reported that powders with a good flowability typically have a FR_H of less than 35 s/50g [7], [22], [72]. The MA, Al, and V powder exhibited poor flowability as they were unable to flow through either funnel. The PA Ti-6Al-4V and the blends successfully flowed through the Carney flowmeter with Blend 2 BE flowing the quickest and Blend 1 MA flowing the slowest of the three. Blend 1 MA is likely to have a poorer flowability due to the highly irregular shaped MA particles.

Table 23: Flowability of dried loose powders

Powder		FR_H (s/50 g)	FR_C (s/200 g)
Raw Powders	PA Ti-6Al-4V	No flow	68.91 ± 3.35
	CP Ti	31.82 ± 0.38	N/A
	MA	No flow	No flow
	Al	No flow	No flow
	V	No flow	No flow
Blend 1 MA	CP Ti-10 MA	No flow	110.38 ± 2.90
Blend 2 BE	CP Ti-6Al-4V	No flow	31.24 ± 2.25

It is difficult to predict whether the PA powder or Blend 2 BE would have better flowability. The CP Ti, with the best flow characteristics, dominated the flow characteristics of Blend 2 BE, regardless of the irregular shaped Al and V powders, and had a quicker flowrate when compared to the PA power. This was counter intuitive as the PA powder had an almost identical PSD and morphology to the CP Ti powder.

The relationship between flowability and drying time of CP Ti powder is shown in Figure 38. It is clear that the flowability of the CP Ti powder improves with drying time and approaches a constant value after two hours of drying. The drying time is dependent on the amount of powder in the container, with larger amounts of powder requiring longer drying times. It was decided that four hours was sufficient for the volume of powder being dried in subsequent tests.

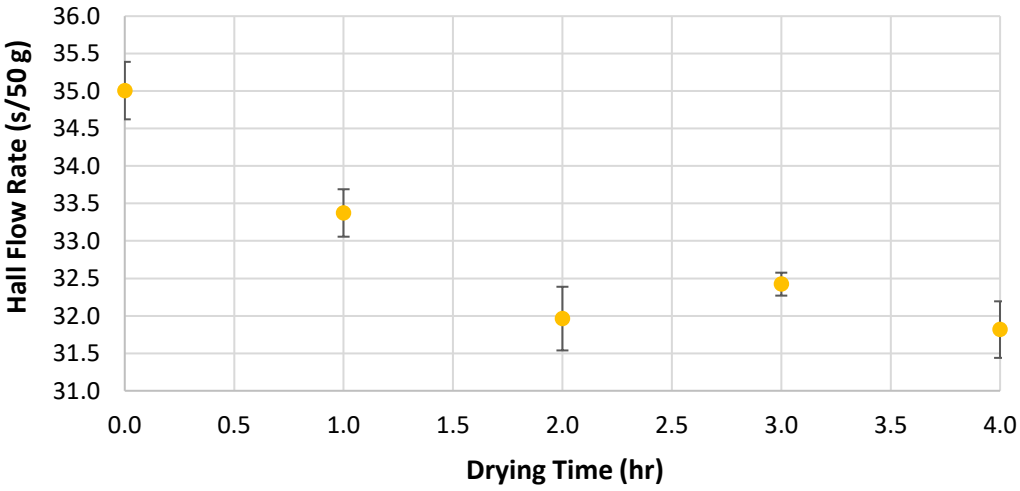

Figure 38: The Hall flow rate of CP Ti powder at incremental drying time. Error bars indicating standard sample error

4.10 Angle of Repose

The static AoR measurements of the dried loose powders can be seen in Table 24. An illustration of how the AoR was obtained using the PA Ti-6Al-4V powder is presented in Figure 39, and the remaining powders presented in Appendix B.2.

Table 24: Angle of repose measurements of dried loose powders

Powder		AoR (°)	Flow classification [124]
Raw Powders	PA Ti-6Al-4V	39.2 ± 1.2	Fair to passable flow
	CP Ti	28.2 ± 0.1	Very free flowing
	MA	46.5 ± 0.7	Cohesive
	Al	39.5 ± 0.6	Fair to passable flow
	V	48.6 ± 0.1	Cohesive
Blend 1 MA	CP Ti-10 MA	39.5 ± 1.8	Fair to passable flow
Blend 2 BE	CP Ti-6Al-4V	34.4 ± 0.4	Free flowing

As expected, the CP Ti powder had the lowest AoR and was categorised as very free flowing, with the Blend 2 BE powder being free flowing. The PA Ti-6Al-4V, Al, and Blend 1 MA had fair to passable flow, and the MA and V powders were deemed as cohesive. These results correlate well to the flowability results, indicating that the AoR is a good indication of flowability.

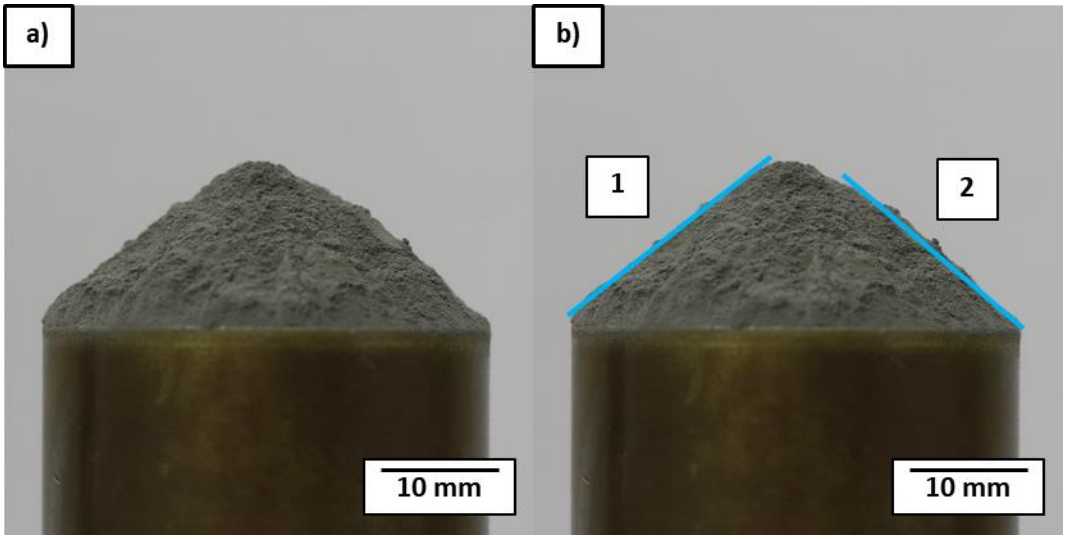

Figure 39: AoR measurements of PA Ti-6Al-4V powder

4.11 Powder Blending Quality

The apparent densities of both powder blends, after various blending times, are presented in Figure 40. The AD of the Blend 1 MA powder increased with blending until 15 minutes where the AD was seen to decrease again. The AD of the Blend 2 BE powder was variable but had a general decreasing trend with increasing blending time. The downwards trend of Blend 2 BE is expected as the increase in mixing increases the Van der Waals forces, inter-particle friction, and mechanical interlocking. This can be attributed to the irregular morphologies and smaller size of the alloying elements [5].

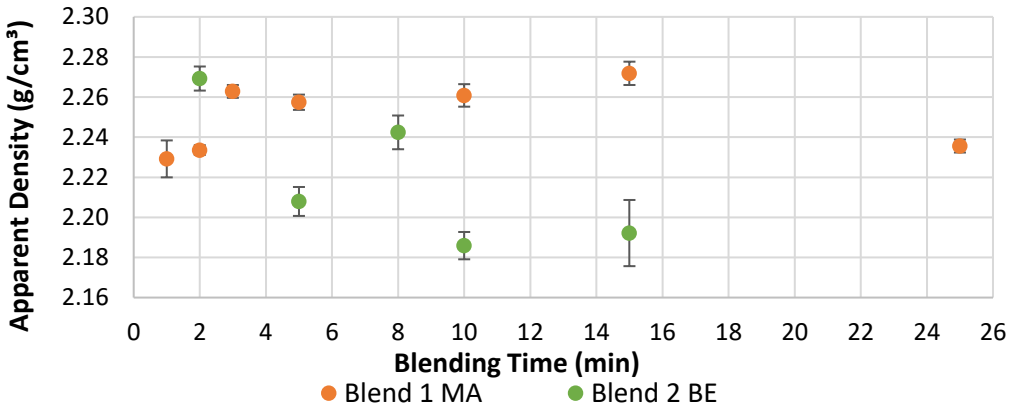

Figure 40: AoR of both blends at various blending times. Error bars indicating the standard sample error

The flowability of the Blend 1 MA powder at various blending times is presented in Figure 41. The flowability, reported up until three minutes of blending, was measured using the Hall flowmeter, after which the flowability result was consistently “no-flow” for subsequent blending times. The Carney flowmeter was used to repeat the test up to 25 minutes of blending, with flowability measured across the entire blending period. The flowability of the Blend 1 MA powder had a general trend of decreasing flowability with an increase in blending time.

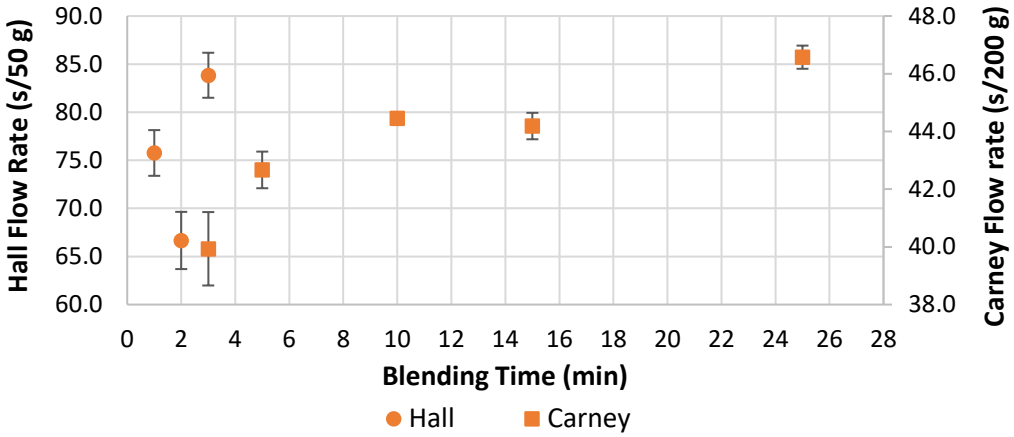

Figure 41: Flowability of Blend 1 MA at various blending times. Error bars indicating the standard sample error

The skeletal density of Blend 2 BE at various locations after 20 minutes of blending is summarised in Table 25. Only minor differences were seen between each sample which indicates that the blend was sufficiently mixed, and the alloying elements were well distributed. The average skeletal density is slightly higher than the calculated theoretical density seen in Table 20, and has a very low standard sample error of 0.02 g/cm^3.

Table 25: Skeletal density results of Blend 2 BE

Powder	Sample	Mass (g)	Volume (cm^3)	Skeletal Density (g/cm^3)
Blend 2 BE	1	9.09	2.06 ± 0.00	4.43 ± 0.00
	2	7.19	1.62 ± 0.00	4.44 ± 0.00
	3	8.89	2.01 ± 0.00	4.43 ± 0.00
	4	9.25	2.08 ± 0.00	4.45 ± 0.00
	5	9.84	2.21 ± 0.00	4.46 ± 0.00
		Ave:		4.44 ± 0.02

The AoR of the Blend 1 MA powder at various blending times is reported in Figure 42. The AoR was seen to increase with an increase in blending time until a relatively constant value was obtained after five minutes of blending.

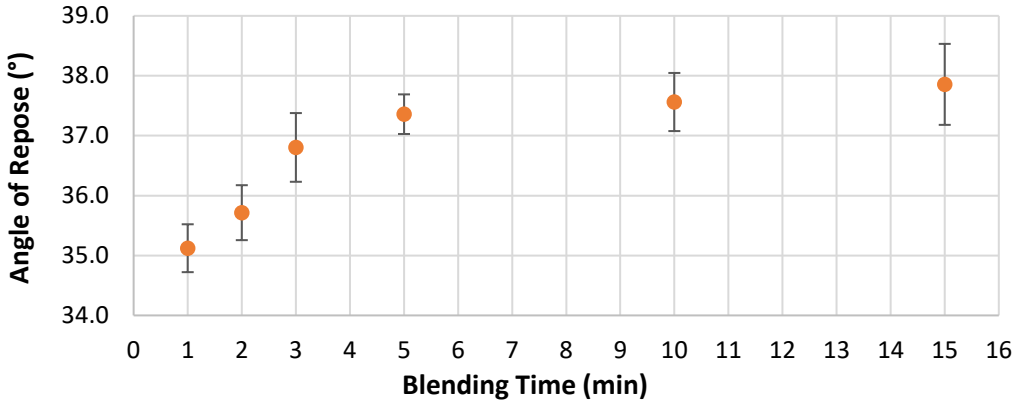

Figure 42: Angle of repose of Blend 1 MA at various blending times. Error bars indicating the standard sample error

4.12 Spreadability Results

The results of the spreadability metrics of percent coverage and spread density, and the elemental blending distribution are presented in this section.

4.12.1 Percent Coverage

The percent coverage results of the non-dried powders at various layer heights are presented in Figure 43. The general trend of all powders is that percent coverage increases with increasing layer height. The CP Ti and Blend 1 MA performed the best, having a percent coverage of around 80 % for a layer height of 100 µm and a percent coverage of 85 % for a layer height of 150 µm. The MA, V, and Blend 2 BE all performed poorly. The PA Ti-6Al-4V showed an improvement around 100 µm and the Al improved drastically at a layer height of 150 µm. The percent coverage images can be found in Appendix C.7.

The comparison of the dried and non-dried powders, of the PA Ti-6Al-4V, Blend 1 MA and Blend 2 BE, is illustrated through Figure 44. Blend 1 MA hardly improved its percent coverage with drying, but the PA Ti-6Al-4V and Blend 2 BE powders improved significantly. The percent coverage images of Figure 62 vs. Figure 63 for the PA Ti-6Al-4V powder, and Figure 70 vs. Figure 71 for the Blend 2 BE powder, confirm these results. According to the AoR and flowability results, the Blend 2 BE powder should have better spreadability than the PA Ti-6Al-4V and the Blend 1 MA powder, however, this was only the case at 60 µm, and only outperforming the Blend 1 MA powder at 80 and 150 µm.

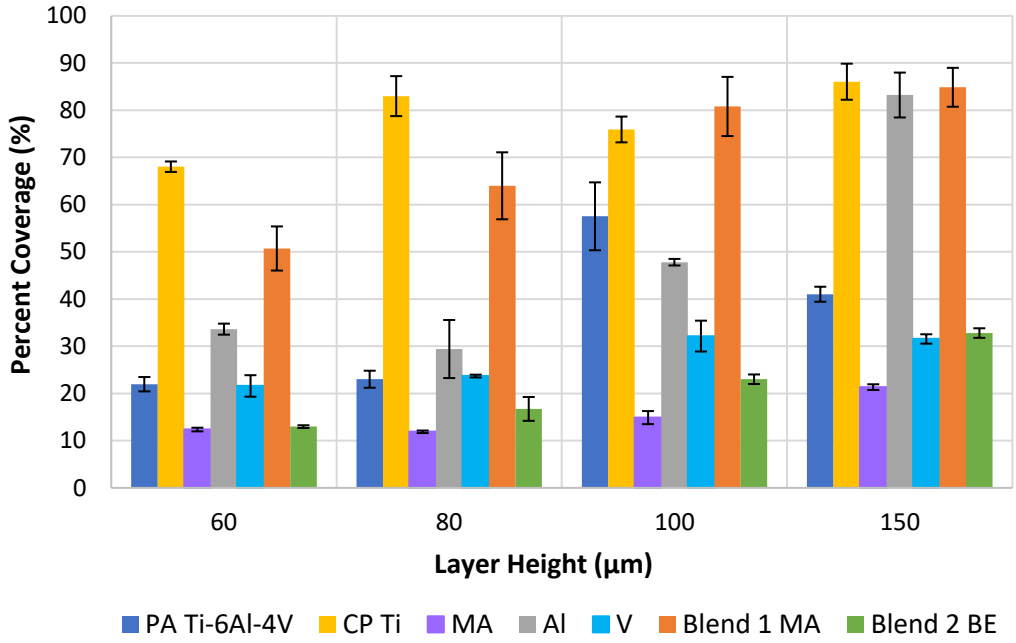

Figure 43: Percent coverage vs. layer height, non-dried powders. Each result shown is the average of two tests with the range indicated by the error bar

The key takeaway from Figure 44 is that all three powders performed similarly at all layer heights after drying. This indicates that the MA and elemental blending of Blend 1 MA and Blend 2 BE, was successful in terms of spreading capability, when compared to the highly spherical PA Ti-6Al-4V, regardless of having constituent powders with irregular morphologies.

Long streaks were seen in the spread powder after the spreadability tests for both Blend 1 MA and Blend 2 BE powders after drying, as shown in Figure 69 and Figure 71, respectively. This can be attributed to particle jamming, as illustrated in Figure 13b, due to poorly orientated elongated powder particles of the MA for Blend 1 MA, Figure 51a, and the Al for Blend 2 BE, Figure 52b-d, as well as large V particles for the Blend 2 BE, Figure 53a. No streaks were present in the spreadability tests for the PA Ti-6Al-4V after drying. This is attributed to the highly spherical powder particles and the narrow PSD span of the PA Ti-6Al-4V powder.

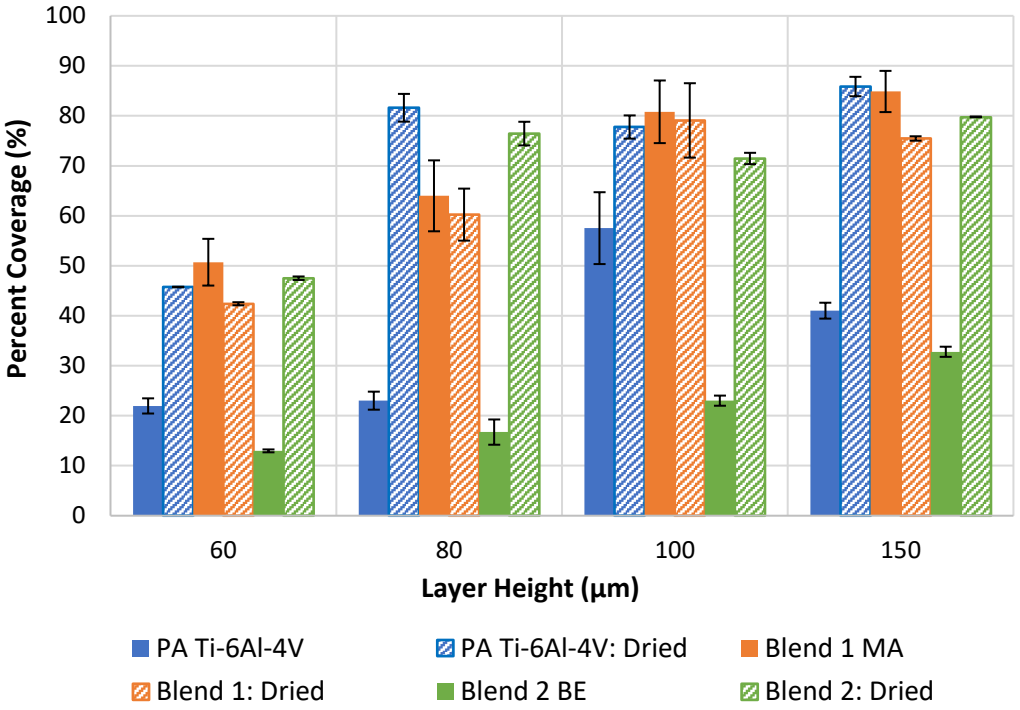

Figure 44: Percent coverage vs. layer height, comparison of dried and non-dried powders. Each result shown is the average of two tests with the range indicated by the error bar

4.12.2 Spreadability – Spread Density

The spread density results of the spreadability tests for non-dried powders are presented in Figure 45. The CP Ti had the highest spread density which can be attributed to its high AD, good flowability, low AoR, and high percent coverage. The spread density of the Al, V, Blend 1 MA, and Blend 2 BE powders increase marginally with increasing layer height, while that of the MA powder stayed relatively constant.

The relative density comparison of the spread and apparent density of the powders is presented in Figure 46. Although this figure is comparing the AD of dried powders to the spread density of non-dried powders, when testing, there was only a marginal increase in AD resulting from drying. The AD is seen to be a poor indication of spread density for all the powders with the exception of the CP Ti, which obtained better packing from the spreading motion.

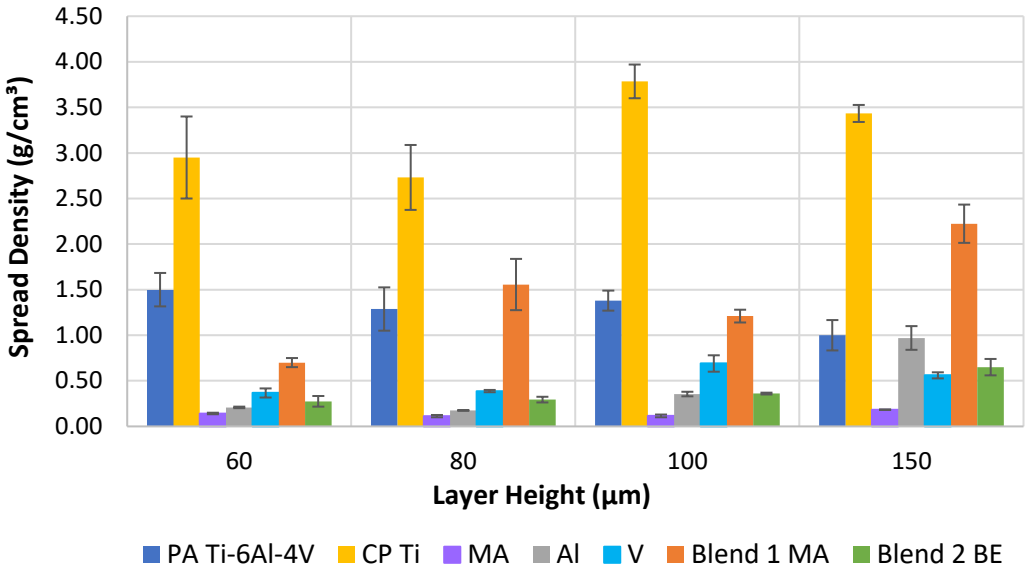

Figure 45: Spread density vs. layer height, non-dried powders. Each result shown is the average of two tests with the range indicated by the error bar

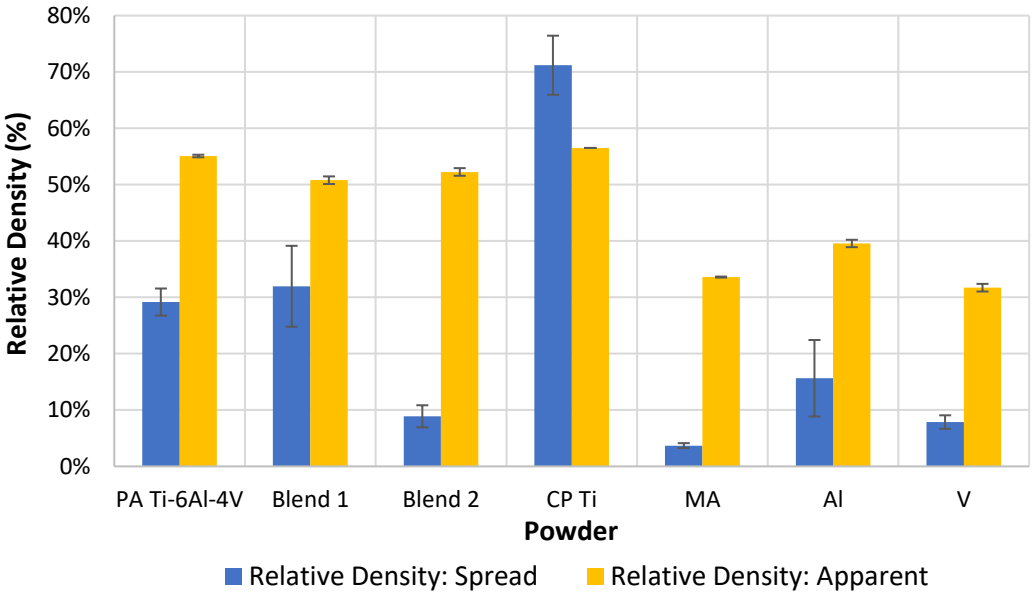

Figure 46: Comparison of relative density from apparent density and spread density of all the powders. Each result shown is the average of two tests with the range indicated by the error bar

4.12.3 Spreadability – Powder Blending Distribution

Sample EDS maps of Blend 1 MA and Blend 2 BE at two different magnifications are presented in Figure 47 and Figure 48, respectively. The elemental maps for Blend 1 MA, were generated from position 2 in Figure 27a, and the elemental maps for Blend 2 BE, Figure 48, were generated from position 4 in Figure 27b. The elemental distributions in weight percent of all positions in Figure 27 have been summarised in Table 26.

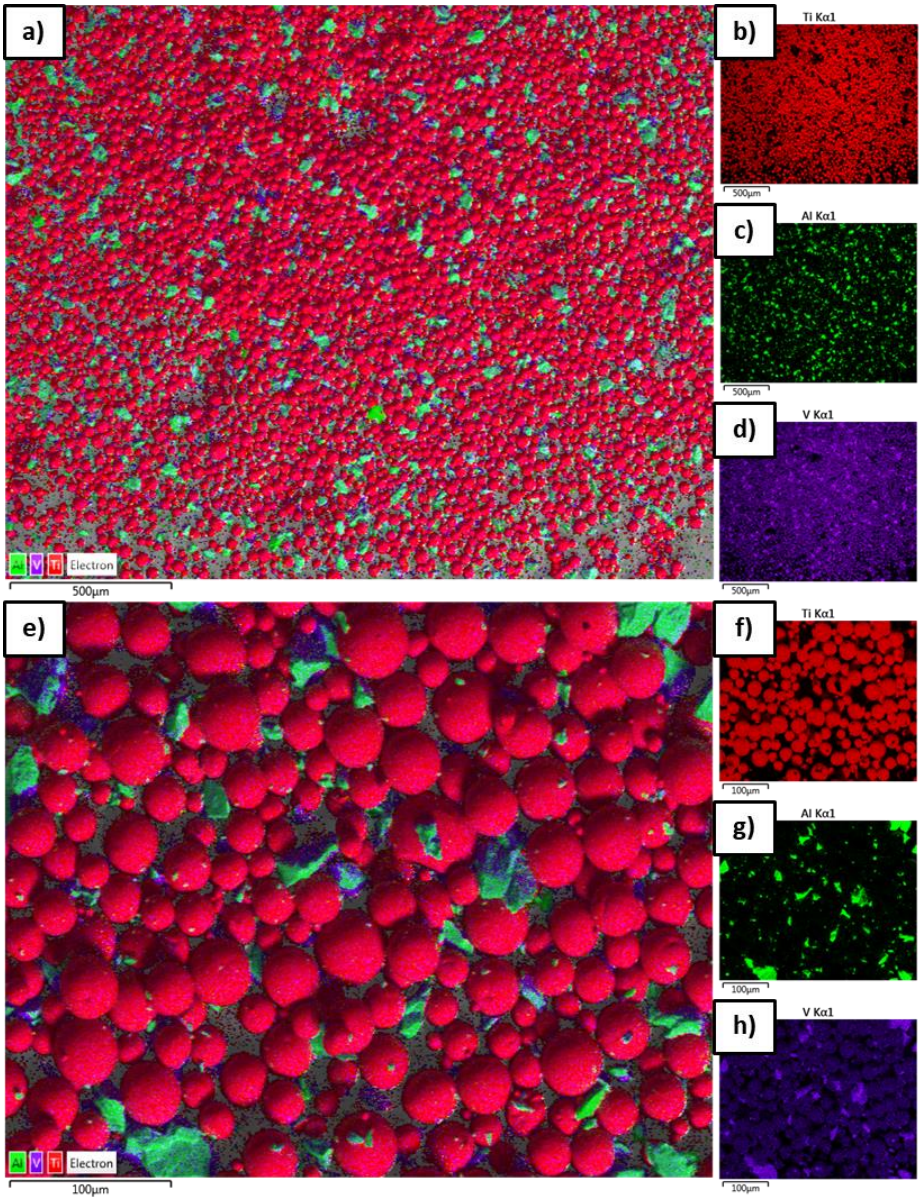

Figure 47: EDS maps of the Blend 1 MA distribution and associated elemental maps with scalebars of a-d) 500 µm and e-h) 100 µm

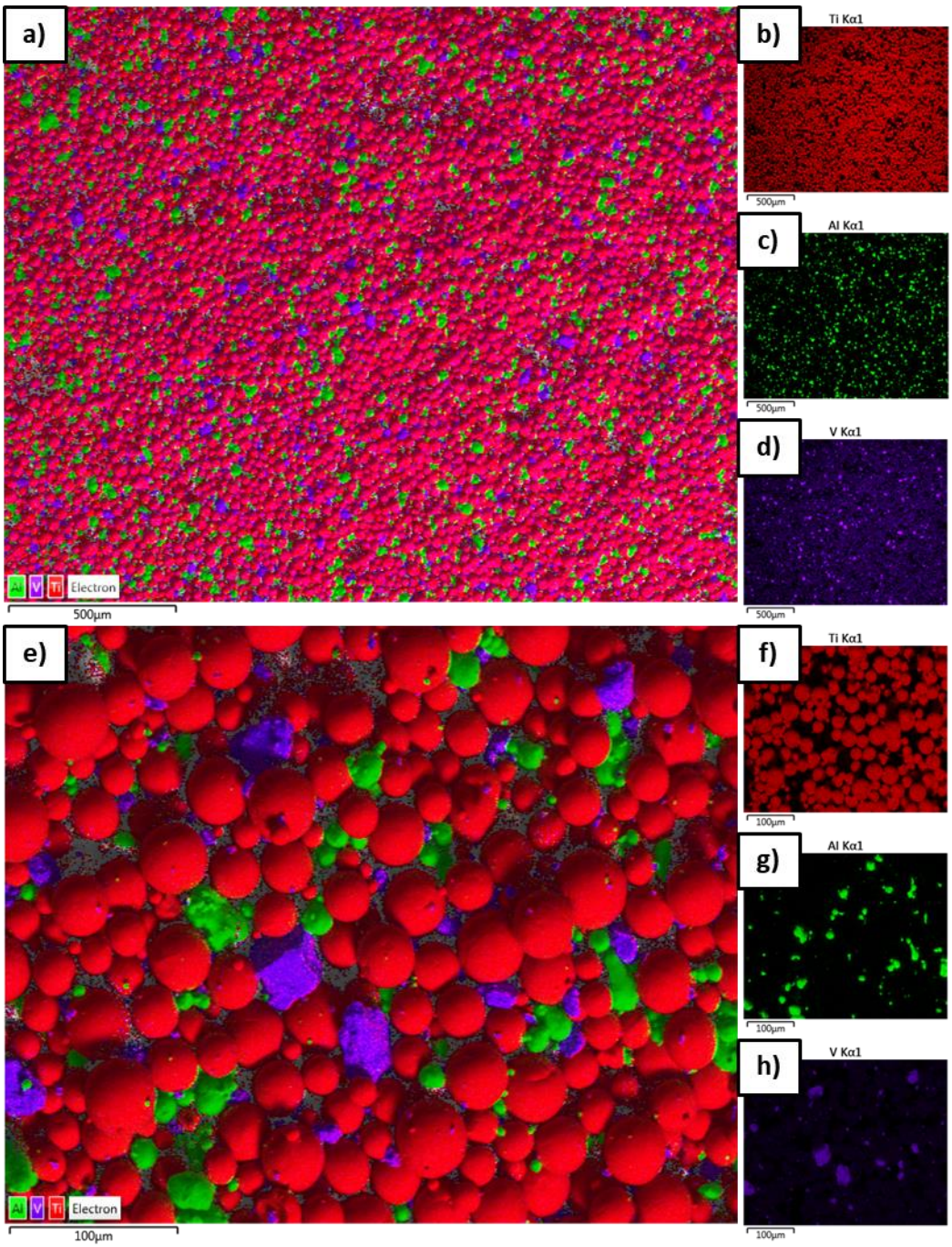

Figure 48: EDS maps of the Blend 2 BE distribution and associated elemental maps with scalebars of a-d) 500 µm and e-h) 100 µm

The elemental distributions should in theory be in the blending ratio of 90:6:4 (Ti:Al:V). The reason why the alloying elements are higher is due to two reasons. This first is that the peaks of titanium and vanadium are very similar, which can be seen by the titanium powder particles being misidentified as vanadium powder

particles in the single vanadium EDS maps of Figure 47d,h and Figure 48d,h. The second reason is due to the morphology of the alloying powders. When the pin stubs were pressed against the powder spread layer, any irregular powder particles would favour the flatter orientation, having a larger surface area. The spherical CP Ti powder particles will have the same surface area regardless of orientation.

Regardless of these inaccuracies, to determine whether the alloying elements were well distributed throughout the blend, the differences between each sample are of importance. The low standard sample error of the elemental compositions of both blends was below 0.45 %, which indicates that the alloying elements were well distributed throughout the blends.

Table 26: Elemental distributions in weight % from EDS maps

Powder	Sample	Scalebar (µm)	Weight %		
			Ti	Al	V
Blend 1 MA	1	500	82.52	10.29	7.19
		100	81.62	10.49	7.89
	2	500	82.78	10.24	6.99
		100	86.30	8.04	5.67
	3	500	80.19	11.74	8.07
		100	78.99	12.49	8.52
	Ave:		82.07 ± 0.42	10.55 ± 0.25	7.39 ± 0.17
Blend 2 BE	4	500	82.41	12.59	5.00
		100	80.44	12.84	6.72
	5	500	79.36	15.25	5.39
		100	80.28	14.92	4.80
	6	500	77.99	16.63	5.38
		100	77.80	17.92	4.28
	Ave:		79.71 ± 0.29	15.03 ± 0.35	5.26 ± 0.14

5 Techno-economic Analysis

A techno-economic analysis on the suitability of MA and elemental blending, in comparison to PA powders, in LPBF systems is outlined in this section. The costs, benefits, risks, uncertainties, and timeframes of this technology is assessed.

5.1 Costs

The costs associated with using MA and elemental blending as opposed to PA powders, is purely based on the material costs as the manufacturing costs are constant. For simplicity, all costs were converted to Rands, with €/R = 19.50, $/R = 16.50, and £/R = 21.50. For simplicity shipping and handling costs have been excluded but are significantly higher when internationally importing due to hazardous material transportation.

Metal powders were purchased in 2017 and the pure material costs per kg are reported. Several quotes from various companies were generated by the Materials Engineering Department and the average costs per kg were reported. These prices have been summarised in Table 27 and rounded to the nearest rand. The calculated costs of Blend 1 MA and Blend 2 BE have also been included.

Table 27: Metal powder cost analysis

Powder						
PA Ti-6Al-4V	CP Ti	MA	Al	V	Blend 1 MA	Blend 2 BE
2017						
R4 125	R3,795	R1,823	R422	R13,365	R3,598	R3,975
2020						
R13 254	R14,762	-	R4,250	R81,406	R13,468	R16,797

In 2017, the cost to produce Blend 1 MA or Blend 2 BE powder was slightly less than the cost of the PA Ti-6Al-4V powder. However, in 2020, it was more expensive to produce the powder blends. The high cost in 2020 was largely attributed to the high average cost of the vanadium powder. This cost may be reduced but with the sacrifice of powder quality. The cost of MA or elemental blending may become competitive if locally sourced CP Ti, Al, MA, and V are made available having the same quality as international suppliers.

The cost to design, build, or source a suitable powder mixing device is also a consideration. Although this will only be a once off and relatively small cost, the

cost associated to blend the powders in term of operator time can be significant when dealing with powders in large quantities.

5.2 Benefits

Ultimately the main benefit of using MA or elemental blending is not the cost saving under current market conditions, but rather the flexibility of alloying composition. Currently, PA powders are limited to the alloying compositions determined by the supplier. The benefit of being able to change the alloying content or adding additional elements to a powder blend can lead to new research and potentially superior alloys through LPBF.

5.3 Risks and Uncertainties

It has been shown in this study that even though irregular shaped alloying powders were used, which is against the LPBF standard, these powder blends have similar powder characteristics to their PA counterpart. Therefore, from a powder characterisation standpoint, MA and elemental powder blends can be used for LPBF.

The recyclability of the powder blends is largely uncertain and requires further investigation. Considering that powder is sieved prior to the re-use cycle, the individual powders are likely to separate and for the powder blend to no longer retain a homogenous distribution. An additional re-blending step after sieving will probably be required.

The risk however lies in the actual LPBF process. Process parameters have been tuned by the manufacturer to be well suited to common powder alloys. When MA and elemental blends are being used, these process parameters must be optimised to obtain a good print quality. Another issue is that individual elements have very different physical properties, which is likely to hinder the success of the LPBF process. These are aspects that will be addressed Mr. Ramosena, the MTech (Mechanical Engineering) student at CUT, conducting the DMLS® study on the blends.

5.4 Timeframes

The timeframe of this technology is largely dependent on the success of DMLS® of the powder blends. If deemed successful, the blends from this study may be

immediately employed for further research as well as future research into other blends.

For this technology to replace PA powders from a manufacturer's standpoint, the blending process must be optimised for the relevant alloy and scaled up for industry. The LPBF process parameters must also be optimised for the success of these blends, which may be determined by the LPBF supplier. If a company deems the cost savings significant, this technology could take around five years to be implemented.

6 Conclusions and Recommendations

In this study, two novel powder blends of Ti-6Al-4V for use in LPBF, more specifically DMLS®, were investigated. The two blends were: Blend 1 MA, a master-alloy blend, consisting of CP Ti-10MA, and Blend 2 BE, an elemental blend, consisting of CP Ti-6Al-4V.

This study successfully characterised the powders in terms of the standard powder characterisation metrics of: chemical composition; powder crystal structure, powder microstructure, morphology, PSD, theoretical, skeletal and AD; flowability; and AoR. A custom designed spreadability test rig was successfully commissioned to obtain relatively novel metrics of percent coverage and spread density. It is recommended that further work focusses on investigating the microstructure of the aluminium and vanadium powders by identifying a feasible etching procedure and utilising SEM imaging instead of OM.

It was noted that moisture has a significant adverse effect on the flowability and spreadability of a powder. Moisture tends to build up on powder particles when stored for long periods of time, and flowability and spreadability can be significantly improved with air drying. Although the benefits of air drying are clear, the oxidation effects on the powders are unknown and should be further investigated. The main limitation with this type of testing is that the equipment availability is limited in South Africa with no oxygen analysis capabilities at SU. Additionally, it is usually conducted at NECSA and involves lengthy waiting periods.

An investigation into the different PSD techniques of laser diffraction and XCT scanning was conducted. This revealed that laser diffraction has significant limitations when analysing the PSDs of irregular shaped powder particles as this technique assumes particles to be spherical and generally overestimates the size of powder particles.

The effect of powder blending time on various powder characterisation metrics of flowability, AD, and AoR, was investigated. It was found that with increased blending time, the flowability and AD decreases, and the AoR increases. This indicates that blended powders become more cohesive with increased blending.

The quality of the powder blending distribution was studied through skeletal density sampling and EDS mapping of a single spread powder layer using the

spreadability test rig. Both techniques indicated that the alloying elements were well distributed throughout the blends and the mixing times were sufficient.

The spreadability test rig was successful in obtaining the desired metrics of percent coverage and spread density but could be upgraded to determine additional metrics and improve its performance and repeatability through various upgrades. With some additional testing, numerical models may be developed to predict the spreadability properties of a powder based on readily available powder characterisation techniques. The spreadability test rig performed well considering the low cost of manufacturing. The recommended improvements to the rig are as follows:

1. A powder dispenser may be designed to deposit the powder evenly at the start of the build plate. One consideration is that each powder has a different AD so this would need to be factored into the design, allowing a uniform heap to be created, regardless of the powder AD and mass of powder used.
2. The stability of the crossbeam may be increased by adding a dual drive system or converting the guide rods to linear guide rails. Slight vibrations due to single drive can be seen in the horizontal lines of the spread powder layer in Figure 63c.
3. An easily adjustable speed function may be incorporated into the Arduino code with the addition of a variable resistor to set the speed. This would require the Arduino to be reprogrammed as well as resoldering the prototyping board. The effect of the recoater speed on the spreadability of the powders may subsequently be tested.
4. The crossbeam may be adjusted to accommodate various recoating blades. This can take the form of a machined clamp to hold the recoater blade in place, which is the current standard in LPBF machines. The effect of various recoating blades on the spreadability of the powders may be investigated. Additionally, a laser light scanner (LLS) could be incorporated into the crossbeam, similarly to the work done by Bester [126].
5. The build plate could be adjusted to have automatic height adjustment and bed levelling. This can be achieved by employing the same drive system of a build plate in a LPBF system. This would require a full redesign of the mechanical components.
6. The build plate was specified in the drawings to have an Ra of 12.5 µm but

was much smoother having an Ra of 1.14 µm, as discussed in Section 3.4.1. The surface roughness of the build plate should be as smooth as possible but greater than the wavelength of the laser, typically in the range of 1 µm, to prevent the laser reflecting on itself. However, the roughness value of the build plate was potentially too smooth and caused the powder to slip. The roughness could be increased by rough sanding or using sandblasting media.

7. The electronics could be converted into a more permanent PCB board to eliminate the large electronics housing and complex wiring setup. The Arduino could also be replaced using this method.

A techno-economic analysis was conducted on the suitability of MA and elemental blending for use in LPBF. It was revealed that the cost savings of this technology are marginal, but the flexibility of alloying ratios is highly valuable and can be used for future research. It is recommended that the recyclability of blended powder be investigated and to what extent sieving influences the separation of the individual elemental powders in the blend.

It was ultimately found that the traditional and novel powder characteristics of the Blend 1 MA and the Blend 2 BE were comparable to that of high-quality plasma atomised PA Ti-6Al-4V powder, with the morphology, PSD, flowability, and AoR having the most significant influence on the spreadability properties of the powder. This indicates that powders that: are more spherical, have a narrow PSD span, are highly flowable, and have a low AoR, have a better spreadability. Finally, this implies that from a powder characterisation standpoint, MA and elemental blending of Ti-6Al-4V can be used in LPBF, regardless of having constituent powders with irregular morphologies.

7 References

[1] Shipley, H. *et al.* 2018. Optimisation of process parameters to address fundamental challenges during selective laser melting of Ti-6Al-4V: A review. *Int. J. Mach. Tools Manuf.* 128: 1–20.

[2] Jia, M., Alshammari, Y., Yang, F., and Bolzoni, L. 2020. Effect of heat treatment on the microstructure and mechanical properties of blended elemental Ti–6Al–4V produced by powder forging. *Mater. Sci. Eng. A*. 791.

[3] Lin, D. *et al.* 2017. Rheological and thermal debinding properties of blended elemental Ti-6Al-4V powder injection molding feedstock. *Powder Technol.* 311: 357–363.

[4] Sabban, R., Bahl, S., Chatterjee, K., and Suwas, S. 2019. Globularization using heat treatment in additively manufactured Ti-6Al-4V for high strength and toughness. *Acta Mater.* 162: 239–254.

[5] Tan, J. H., Wong, W. L. E., and Dalgarno, K. W. 2017. An overview of powder granulometry on feedstock and part performance in the selective laser melting process. *Addit. Manuf.* 18: 228–255.

[6] Sutton, A. T., Kriewall, C. S., Leu, M. C., and Newkirk, J. W. 2017. Powder characterisation techniques and effects of powder characteristics on part properties in powder-bed fusion processes. *Virtual Phys. Prototyp.* 12.1: 3–29.

[7] Brika, S. E., Letenneur, M., Dion, C. A., and Brailovski, V. 2020. Influence of particle morphology and size distribution on the powder flowability and laser powder bed fusion manufacturability of Ti-6Al-4V alloy. *Addit. Manuf.* 31.

[8] Sun, D. *et al.* 2019. Selective laser melting of titanium parts: Influence of laser process parameters on macro- and microstructures and tensile property. *Powder Technol.* 342: 371–379.

[9] Khorasani, A. M., Gibson, I., Awan, U. S., and Ghaderi, A. 2019. The effect of SLM process parameters on density, hardness, tensile strength and surface quality of Ti-6Al-4V. *Addit. Manuf.* 25: 176–186.

[10] Zhechao, F. and Hongwei, F. 2018. Study on selective laser melting and heat treatment of Ti-6Al-4V alloy. *Results Phys.* 10: 660–664.

[11] Pleass, C. and Jothi, S. 2018. Influence of powder characteristics and additive manufacturing process parameters on the microstructure and mechanical behaviour of Inconel 625 fabricated by Selective Laser Melting. *Addit. Manuf.* 24: 419–431.

[12] Kahlin, M., Ansell, H., and Moverare, J. J. 2017. Fatigue behaviour of additive manufactured Ti6Al4V, with as-built surfaces, exposed to variable amplitude loading. *Int. J. Fatigue*. 103: 353–362.

[13] Sun, J., Zhu, X., Qiu, L., Wang, F., Yang, Y., and Guo, L. 2019. The microstructure transformation of selective laser melted Ti-6Al-4V alloy. *Mater. Today Commun.* 19: 277–285.

[14] Clayton, R. M. 2013. The use of elemental powder mixes in laser-based additive manufacturing. *Masters Theses*. [Online]. Available: http://scholarsmine.mst.edu/masters_theses/7194.

[15] Zenani, A., du Preez, W. B., Dzogbewu, T. C., and Yadroitsev, I. 2019. Metal Additive Manufacturing of Ti6Al from Blended Elemental Powders, in *International Conference on Competitive Manufacturing*, 181–187.

[16] Ramosena, L. A., Parker, B. S., Dzogbewu, T. C., du Preez, W. B., and Blaine, D. C. 2019. Optimum process parameters for DMLS in-situ alloying of a Ti-10(60Al40V) powder blend, in *Rapid Product Development Association of South Africa (RAPDASA)*, 78–93.

[17] Anderson, I. E., White, E. M. H., and Dehoff, R. 2018. Feedstock powder processing research needs for additive manufacturing development. *Curr. Opin. Solid State Mater. Sci.* 22: 8–15.

[18] Dawes, J., Bowerman, R., and Trepleton, R. 2015. Introduction to the Additive Manufacturing Powder Metallurgy Supply Chain. *Johnson Matthey Technol. Rev.* 59.3: 243–256.

[19] Drake, D. M. 2018. An Approach for Defining the Key Quality Characteristics of Metal Powder for Powder Bed Fusion and Directed Energy Deposition.

[20] Snow, Z. 2018. Understanding powder spreadability in powder bed fusion additive manufacturing. [Online]. Available: https://etda.libraries.psu.edu/files/final_submissions/17825.

[21] German, R. 2005. *Powder metallurgy and particulate materials processing*. Princeton, New Jersey: Metal powder industries federation.

[22] Chen, G., Zhao, S. Y., Tan, P., Wang, J., Xiang, C. S., and Tang, H. P. 2018. A comparative study of Ti-6Al-4V powders for additive manufacturing by gas atomization, plasma rotating electrode process and plasma atomization. *Powder Technol.* 333: 38–46.

[23] Garboczi, E. J. and Hrabe, N. 2020. Particle shape and size analysis for metal powders used for additive manufacturing: Technique description and application to two gas-atomized and plasma-atomized Ti64 powders. *Addit. Manuf.* 31.

[24] Zhong, C., Chen, J., Linnenbrink, S., Gasser, A., Sui, S., and Poprawe, R. 2016. A comparative study of Inconel 718 formed by High Deposition Rate Laser Metal Deposition with GA powder and PREP powder. *Mater. Des.* 107: 386–392.

[25] Carpenter Additive. 2020. Comparison of Plasma and Electrode Inert Gas.

[26] Sun, P. E. I., Fang, Z. Z. A. K., Zhang, Y., and Xia, Y. 2017. Review of the Methods for Production of Spherical Ti and Ti Alloy Powder. *J. Miner. Met. Mater. Soc.* 69.10: 1853–1860.

[27] Wei, W.-H., Wang, L.-Z., Chen, T., Duan, X.-M., and Li, W. 2017. Study on the flow properties of Ti-6Al-4V powders prepared by radio-frequency plasma spheroidization. *Adv. Powder Technol.* 28.9: 2431–2437.

[28] Goso, X. and Kale, A. 2011. Production of titanium metal powder by the HDH

process. *J. South. African Inst. Min. Metall.* 111: 203–210.

[29] Azevedo, C. R. F., Rodrigues, D., and Neto, F. B. 2003. Ti-Al-V powder metallurgy (PM) via the hydrogenation-dehydrogenation (HDH) process. *J. Alloys Compd.* 353.1–2: 217–227.

[30] Asgarian, A. *et al.* 2018. Experimental and compntational analysis of a water spray; application to molten metal atomization, in *Advances in Powder Metallurgy and Particulate Materials, POWDERMET*, June: 126–137.

[31] Moskalyk, R. R. and Alfantazi, A. M. 2003. Processing of vanadium : a review. *Miner. Eng.* 16: 793–805.

[32] Vermaak, M. 2000. Vanadium recovery in the electro-aluminothermic production of ferrovanadium, University of Pretoria.

[33] Peterson, J. R. and Smathers, D. B. 1986. Vanadium : an overview of industrial capacity and other factors. *J. Nucl. Mater.* 143: 1113–1116.

[34] Sutulov, A. and Wang, C. T. 2020. Vanadium processing. Encyclopædia Britannica. [Online]. Available: https://www.britannica.com/technology/vanadium-processing.

[35] Okamoto, H. 2012. Al-V (Aluminum-Vanadium). *J. Phase Equilibria Diffus.* 33.6: 491.

[36] Greetham, G. 2001. Powder Metallurgy - Processing. *Azo Materials*. [Online]. Available: https://www.azom.com/article.aspx?ArticleID=132 [2020, November 12].

[37] Kerns, J. 2016. Powder Metallurgy Processes. *Machine Design*. [Online]. Available: https://www.machinedesign.com/materials/metals/article/21834821/powdermetallurgy-processes [2020, November 12].

[38] Dehghan-Manshadi, A., Bermingham, M. J., Dargusch, M. S., StJohn, D. H., and Qian, M. 2017. Metal injection moulding of titanium and titanium alloys: Challenges and recent development. *Powder Technol.* 319: 289–301.

[39] Gilbert, N. 2012. Hot Isostatic Pressing (HIP) – The Fundamentals, Industrial Applications and Benefits. *Azo Materials*. [Online]. Available: https://www.azom.com/article.aspx?ArticleID=6039 [2020, October 27].

[40] Sames, W. J., List, F. A., Pannala, S., Dehoff, R. R., and Babu, S. S. 2016. The metallurgy and processing science of metal additive manufacturing. *Int. Mater. Rev.* 61.5: 315–360.

[41] FormAlloy. 2020. OEM Solutions. [Online]. Available: https://www.formalloy.com/oem-solutions [2021, February 01].

[42] Zhang, J., Song, B., Wei, Q., Bourell, D., and Shi, Y. 2019. A review of selective laser melting of aluminum alloys: Processing, microstructure, property and developing trends. *J. Mater. Sci. Technol.* 35.2: 270–284.

[43] ASTM F136. 2013. Standard Specification for Wrought Titanium-6Aluminum-4Vanadium ELI (Extra Low Interstitial) Alloy for Surgical Implant Applications (UNS

R56401). *ASTM International*. [Online]. Available: www.astm.org.

[44] Guo, Y., Feng, W., Jerry, L., and Hsi, Y. 2020. Semi-supervised deep learning based framework for assessing manufacturability of cellular structures in direct metal laser sintering process. *J. Intell. Manuf.*

[45] Snow, Z., Martukanitz, R., and Joshi, S. 2019. On the development of powder spreadability metrics and feedstock requirements for powder bed fusion additive manufacturing. *Addit. Manuf.* 28: 78–86.

[46] Clayton, J. and Deffley, R. 2014. Metal Powders for Additive Manufacturing Performance and Consistency Required in Demanding. *Metal-Powder.Net*. .October: 14–17.

[47] Wohlfart, M. 2020. Use-cases of different recoater configurations for DMLS®. *EOS*. [Online]. Available: https://www.linkedin.com/pulse/use-cases-different-recoater-configurations-dmls-michael-wohlfart/.

[48] Liu, S. and Shin, Y. C. 2019. Additive manufacturing of Ti6Al4V alloy: A review. *Mater. Des.* 164.

[49] Kaye, B. H. 1997. Mixing of Powders. in *Handbook of Powder Science & Technology*. New York, NY: Chapman & Hall, 568–585.

[50] Ye, S., Mo, W., Lv, Y., Wang, Z., Kwok, C. T., and Yu, P. 2019. The technological design of geometrically complex Ti-6Al-4V parts by metal injection molding. *Appl. Sci.* 9.7.

[51] Bolzoni, L., Ruiz-Navas, E. M., and Gordo, E. 2015. Feasibility study of the production of biomedical Ti–6Al–4V alloy by powder metallurgy. *Mater. Sci. Eng. C*. 49: 400–407.

[52] Paramore, J. D., Fang, Z. Z., Sun, P., Koopman, M., Chandran, K. S. R., and Dunstan, M. 2015. A powder metallurgy method for manufacturing Ti-6Al-4V with wrought-like microstructures and mechanical properties via hydrogen sintering and phase transformation (HSPT). *Scr. Mater.* 107: 103–106.

[53] Kim, Y., Kim, E. P., Song, Y. B., Lee, S. H., and Kwon, Y. S. 2014. Microstructure and mechanical properties of hot isostatically pressed Ti-6Al-4V alloy. *J. Alloys Compd.* 603: 207–212.

[54] Bolzoni, L., Meléndez, I. M., Ruiz-Navas, E. M., and Gordo, E. 2012. Microstructural evolution and mechanical properties of the Ti-6Al-4V alloy produced by vacuum hot-pressing. *Mater. Sci. Eng. A*. 546: 189–197.

[55] ASTM B348. 2013. Standard Specification for Titanium and Titanium Alloy Bars and Billets. *ASTM International*. [Online]. Available: www.astm.org.

[56] Murr, L. E. *et al.* 2009. Microstructure and mechanical behavior of Ti-6Al-4V produced by rapid-layer manufacturing, for biomedical applications. *J. Mech. Behav. Biomed. Mater.* 2.1: 20–32.

[57] Murphy, T. 2019. Preparation of loose powders for metallography. Email correspondence.

[58] Sun, Y., Aindow, M., and Hebert, R. J. 2018. Comparison of virgin Ti-6Al-4V

powders for additive manufacturing. *Addit. Manuf.* 21: 544–555.

[59] Cordova, L., Bor, T., de Smit, M., Campos, M., and Tinga, T. 2020. Measuring the spreadability of pre-treated and moisturized powders for laser powder bed fusion. *Addit. Manuf.* 32.

[60] Muñiz-Lerma, J. A., Nommeots-Nomm, A., Waters, K. E., and Brochu, M. 2018. A comprehensive approach to powder feedstock characterization for powder bed fusion additive manufacturing: A case study on AlSi7Mg. *Materials (Basel).* 11.12.

[61] Barnes, J., Francqui, F., and Dehoff, R. 2019. Understanding metal powder requirements for Additive Manufacturing: Views from the industry. *Metal Additive Manufacturing Vol. 5 No. 3*. 175–182.

[62] Almangour, B., Grzesiak, D., and Yang, J. 2018. In situ formation of TiC-particle-reinforced stainless steel matrix nanocomposites during ball milling : Feedstock powder preparation for selective laser melting at various energy densities. *Powder Technol.* 326: 467–478.

[63] ASTM B214. 2013. Standard Test Method for Sieve Analysis of Metal Powders. *ASTM International*. West Conshohocken, PA. [Online]. Available: www.astm.org.

[64] du Plessis, A., le Roux, S. G., and Guelpa, A. 2016. The CT Scanner Facility at Stellenbosch University: An open access X-ray computed tomography laboratory. *Nucl. Instruments Methods Phys. Res. B*. 384: 42–49.

[65] Horiba Scientific. 2019. A guidebook to particle size analysis. [Online]. Available: https://static.horiba.com/fileadmin/Horiba/Products/Scientific/Particle_Characterization/Particle_Guidebook_09-2019.pdf.

[66] Webb, P. a. 2001. Volume and Density Determinations for Particle Technologists. *Micromeritics Instrument Corporation*. [Online]. Available: http://www.micromeritics.com/Repository/Files/density_determinations.pdf.

[67] German, R. M. and Park, S. J. 2008. *Mathematical relations in particulate materials processing*. Wiley.

[68] ASTM B527. 2015. Standard Test Method for Tap Density of Metal Powders and Compounds. *ASTM International*. [Online]. Available: www.astm.org.

[69] ASTM B213. 2013. Standard Test Methods for Flow Rate of Metal Powders Using the Hall Flowmeter Funnel. *ASTM International*. [Online]. Available: www.astm.org.

[70] ASTM B964. 2013. Standard Test Methods for Flow Rate of Metal Powders Using the Carney Funnel. *ASTM International*. [Online]. Available: www.astm.org.

[71] Gu, H. *et al.* 2015. Effects of powder variation on the microstructure and tensile strength of Ti-6Al-4V parts fabricated by selective laser melting. *Int. J. Powder Metall.* 51.1: 35–42.

[72] Sun, P., Fang, Z. Z., Xia, Y., Zhang, Y., and Zhou, C. 2016. A novel method for production of spherical Ti-6Al-4V powder for additive manufacturing. *Powder Technol.* 301: 331–335.

[73] Spierings, A. B., Voegtlin, M., Bauer, T., and Wegener, K. 2016. Powder flowability

characterisation methodology for powder-bed-based metal additive manufacturing. *Prog. Addit. Manuf.* 1.1–2: 9–20.

[74] Brisenmark, L. and Lindström, S. 2020. Image based analysis on powder spreadability in powder bed additive manufacturing, KTH.

[75] Beakawi Al-Hashemi, H. M. and Baghabra Al-Amoudi, O. S. 2018. A review on the angle of repose of granular materials. *Powder Technol.* 330: 397–417.

[76] Xu, G. *et al.* 2018. Investigation on characterization of powder flowability using different testing methods. *Exp. Therm. Fluid Sci.* 92: 390–401.

[77] Krantz, M., Zhang, H., and Zhu, J. 2009. Characterization of powder flow: Static and dynamic testing. *Powder Technol.* 194.3: 239–245.

[78] Schulze, D. 2010. Flow properties of powders and bulk solids (fundamentals). *Powder Technol.* 65.1–3: 321–333.

[79] Cundall, P. A. and Strack, O. D. L. 1979. A discrete numerical model for granular assemblies. *Geotechnique*. 29.1: 47–65.

[80] Parteli, E. J. R. and Pöschel, T. 2016. Particle-based simulation of powder application in additive manufacturing. *Powder Technol.* 288: 96–102.

[81] He, Y., Gardy, J., Hassanpour, A., and Bayly, A. E. 2020. A digital-based approach for characterising spread powder layer in additive manufacturing. *Mater. Des.* 196.

[82] Nan, W. and Ghadiri, M. 2019. Numerical simulation of powder flow during spreading in additive manufacturing. *Powder Technol.* 342: 801–807.

[83] Nan, W. *et al.* 2018. Jamming during particle spreading in additive manufacturing. *Powder Technol.* 338: 253–262.

[84] Chen, H., Wei, Q., Zhang, Y., Chen, F., Shi, Y., and Yan, W. 2019. Powder-spreading mechanisms in powder-bed-based additive manufacturing: Experiments and computational modeling. *Acta Mater.* 179: 158–171.

[85] Xin, H., Sun, W. C., and Fish, J. 2018. Discrete element simulations of powder-bed sintering-based additive manufacturing. *Int. J. Mech. Sci.* 149: 373–392.

[86] Haeri, S., Wang, Y., Ghita, O., and Sun, J. 2017. Discrete element simulation and experimental study of powder spreading process in additive manufacturing. *Powder Technol.* 306: 45–54.

[87] Lee, W. H., Zhang, Y., and Zhang, J. 2017. Discrete element modeling of powder flow and laser heating in direct metal laser sintering process. *Powder Technol.* 315: 300–308.

[88] Wang, L., Li, E. L., Shen, H., Zou, R. P., Yu, A. B., and Zhou, Z. Y. 2020. Adhesion effects on spreading of metal powders in selective laser melting. *Powder Technol.* 363: 602–610.

[89] Haeri, S. 2017. Optimisation of blade type spreaders for powder bed preparation in Additive Manufacturing using DEM simulations. *Powder Technol.* 321: 94–104.

[90] Mindt, H. W., Megahed, M., Lavery, N. P., Holmes, M. A., and Brown, S. G. R.

2016. Powder Bed Layer Characteristics: The Overseen First-Order Process Input. *Metall. Mater. Trans. A*. 47.8: 3811–3822.

[91] Desai, P. S. 2019. Spreading Process Maps for Powder-Bed Additive Manufacturing Derived from Physics Model-Based Machine Learning. *Metals (Basel).* 9.11: 1–15.

[92] Meier, C., Weissbach, R., Weinberg, J., Wall, W. A., and Hart, A. J. 2019. Critical influences of particle size and adhesion on the powder layer uniformity in metal additive manufacturing. *J. Mater. Process. Technol.* 266: 484–501.

[93] Meier, C., Weissbach, R., Weinberg, J., Wall, W. A., and John Hart, A. 2019. Modeling and characterization of cohesion in fine metal powders with a focus on additive manufacturing process simulations. *Powder Technol.* 343: 855–866.

[94] Fouda, Y. M. and Bayly, A. E. 2020. A DEM study of powder spreading in additive layer manufacturing. *Granul. Matter*. 22.1: 1–18.

[95] Ahmed, M., Pasha, M., Nan, W., and Ghadiri, M. 2020. A simple method for assessing powder spreadability for additive manufacturing. *Powder Technol.* 367: 671–679.

[96] Otsu, N. 1979. A Threshold Selection Method from Gray-Level Histograms. *IEEE Trans. Syst. Man. Cybern.* 9.1: 62–66.

[97] Escano, L. I. *et al.* 2018. Revealing particle-scale powder spreading dynamics in powder-bed-based additive manufacturing process by high-speed x-ray imaging. *Sci. Rep.* 8.1: 1–11.

[98] Castellanos, A. 2005. The relationship between attractive interparticle forces and bulk behaviour in dry and uncharged fine powders. *Adv. Phys.* 54.4: 263–376.

[99] Ghosh, S., Prasanna, V. L., Sowjanya, B., Srivani, P., and Alagaraja, M. 2013. Inductively coupled plasma - Optical emission spectroscopy : A review. *Asian J. Pharm. Anal.* 3.1.

[100] ELTRA. 2006. ONH - 2000 - Oxygen/Nitrogen/Hydrogen Determinator. [Online]. Available: http://img62.chem17.com/1/20140105/635245541357687720290.pdf.

[101] Brandon, D. and Kaplan, W. D. 2008. *Microstructural Characterization of Materials*. John Wiley & Sons, Ltd.

[102] Callister, W. D. and Rethwisch, D. G. 2014. *Materials science and engineering*. 9th ed. Wiley Online.

[103] ThermoFisher Scientific. 2019. Scanning Electron Microscopy. *ThermoFisher Scientific: Materials Science*. [Online]. Available: https://www.thermofisher.com/za/en/home/materials-science/learning-center/applications/sem-electrons.html.

[104] ASTM B923. 2013. ASTM B923, Standard Test Method for Metal Powder Skeletal Density by Helium or Nitrogen Pycnometry. *ASTM International*. [Online]. Available: www.astm.org.

[105] ASTM B212. 2013. Standard Test Method for Apparent Density of Free-Flowing

Metal Powders Using the Hall Flowmeter Funnel. *ASTM International*. [Online]. Available: www.astm.org.

[106] ASTM B417. 2013. Standard Test Method for Apparent Density of Non-Free-Flowing Metal Powders Using the Carney Funnel. *ASTM International*. [Online]. Available: www.astm.org.

[107] University of Trento. 2019. Materials Analysis Using Diffraction (MAUD). [Online]. Available: http://maud.radiographema.eu/.

[108] Jain, A. *et al.* 2013. The Materials Project: A materials genome approach to accelerating materials innovation. *APL Mater.* 1.1: 11002.

[109] Downs, R. T. and Hall-Wallace, M. 2003. The American Mineralogist Crystal Structure Database. *Am. Mineral.* 88: 247–250.

[110] Gražulis, S. *et al.* 2009. Crystallography Open Database {--} an open-access collection of crystal structures. *J. Appl. Crystallogr.* 42.4: 726–729.

[111] Quirós, M., Gražulis, S., Girdzijauskaitė, S., Merkys, A., and Vaitkus, A. 2018. Using SMILES strings for the description of chemical connectivity in the Crystallography Open Database. *J. Cheminform.* 10.1: 1–17.

[112] Merkys, A., Vaitkus, A., Butkus, J., Okulič-Kazarinas, M., Kairys, V., and Gražulis, S. 2016. COD::CIF::Parser: an error-correcting CIF parser for the Perl language. *J. Appl. Crystallogr.* 49: 292–301.

[113] Gražulis, S. *et al.* 2012. Crystallography Open Database (COD): an open-access collection of crystal structures and platform for world-wide collaboration. *Nucleic Acids Res.* 40.1: 420–427.

[114] Gražulis, S., Merkys, A., Vaitkus, A., and Okulič-Kazarinas, M. 2015. Computing stoichiometric molecular composition from crystal structures. *J. Appl. Crystallogr.* 48.1: 85–91.

[115] Xu, Y., Yamazaki, M., and Villars, P. 2011. Inorganic materials database for exploring the nature of material. *Jpn. J. Appl. Phys.* 50: 1–5.

[116] Struers. 2020. Epofix Resin - Safety Data Sheet. [Online]. Available: https://www.struers.com/en/Search?q=epofix+msds [2020, September 29].

[117] Struers. 2020. Epofix Hardener - Safety Data Sheet. [Online]. Available: https://www.struers.com/-/media/Library/SDS/United-States/Mounting/SDS-EPOFIX-HARDENER-US-EN-M0026.pdf [2020, September 29].

[118] Struers. 2016. Metallographic preparation of titanium. *Application Notes*. [Online]. Available: https://www.struers.com/-/media/Struers-media-library/Materials/Application-reports/Application_Note_Titanium_2015_ENG.pdf [2020, October 26].

[119] Struers. 2016. Metallographic preparation of aluminium and aluminium alloys. *Application Notes*. [Online]. Available: https://www.struers.com/-/media/Struers-media-library/Materials/Application-reports/AN-11_Aluminium_2015_ENG.pdf [2020, October 25].

[120] Micromeritics. 2018. The Definitive Guide to Powder Characterization Exploring

industrial requirements for characterization. [Online]. Available: https://www.micromeritics.com/Powder_Characterization_wp.

[121] Bansal, R., Singh, J. K., Singh, V., Singh, D. D. N., and Das, P. 2017. Optimization of Oxidation Temperature for Commercially Pure Titanium to Achieve Improved Corrosion Resistance. *J. Mater. Eng. Perform.* 26.3: 969–977.

[122] Sharma, R. K., Singh, M., Kumar, P., and Reddy, G. B. 2015. Oxidation of vanadium metal in oxygen plasma and their characterizations. *AIP Adv.* 5.9.

[123] Coker, E. N. 2013. The oxidation of aluminum at high temperature studied by Thermogravimetric Analysis and Differential Scanning Calorimetry. *Sandia Rep. Sandia Natl. Lab.* .October: 1–22.

[124] Riley, R. E. and Hausner, H. H. 1970. Effect of particle size distribution on the friction in a powder mass. *Int. J. Powder Met*. 6: 17–22.

[125] Esmaily, M., Nooshin Mortazavi, S., Todehfalah, P., and Rashidi, M. 2013. Microstructural characterization and formation of α′ martensite phase in Ti–6Al–4V alloy butt joints produced by friction stir and gas tungsten arc welding processes. *Mater. Des.* 47: 143–150.

[126] Bester, D. 2019. Evaluation of carbon fibre powder scrapers used in metal additive manufacturing. [Online]. Available: https://repository.nwu.ac.za/bitstream/handle/10394/33922/7.1.11.7 4 Bester DC 27177114.pdf?sequence=1.

[127] Friends-of-Fritzing foundation. 2019. Fritzing. [Online]. Available: https://fritzing.org/.

Appendix A Methodology

Additional methodology has been included in this section due to space limitations in the thesis.

A.1 Powder Microstructure

The detailed grinding and polishing procedures to obtain the powder microstructure of loose powders is seen in Table 28.

Table 28: Grinding and polishing steps for OM of loose powders

Powder	Step		PG[1]	FG1[2]	FG2	DG[3]	OP[4]
PA Ti-6Al-4V	Surface		Foil/ Paper	MD-Largo			MD-Chem
	Abrasive	Type	SiC	Diamond			Colloidal silica
		Size	#500	9 µm			0.04 µm
	Suspension/ lubricant		Water	DiaPro Allegro			OP-S
	Force (N)		20	20			20
	Time (min)		Until Plane	2			3
CP Ti	Surface		Foil/ Paper	MD-Largo			MD-Chem
	Abrasive	Type	SiC	Diamond			Colloidal silica
		Size	#500	9 µm			0.04 µm
	Suspension/ lubricant		Water	9 µm			OP-S
	Force (N)		20	20			20
	Time (min)		Until Plane	2			3
MA	Surface		Foil/ Paper	Foil/ Paper	Foil/ Paper	MD-Mol	OP-Chem
	Abrasive	Type	SiC	SiC	SiC	Diamond	Colloidal silica
		Size	#500	#800	#1200	3 µm	0.04 µm

	Suspension/ lubricant		Water	Water	Water	DiaPro Mol R3	OP-S
	Force (N)		20	20	20	20	20
	Time (min)		Until Plane	0.5	0.5	2	1.5
Al	Surface		Foil/ Paper	Foil/ Paper	Foil/ Paper	MD-Mol	OP-Chem
	Abrasive	Type	SiC	SiC	SiC	Diamond	Colloidal silica
		Size	#500	#800	#1200	3 µm	0.04 µm
	Suspension/ lubricant		Water	Water	Water	DiaPro Mol R3	OP-S
	Force (N)		20	20	20	20	20
	Time (min)		Until Plane	0.5	0.5	2	1.5
V	Surface		Foil/ Paper	Foil/ Paper	Foil/ Paper	MD-Mol	OP-Chem
	Abrasive	Type	SiC	SiC	SiC	Diamond	Colloidal silica
		Size	#500	#800	#1200	3 µm	0.04 µm
	Suspension/ lubricant		Water	Water	Water	DiaPro Mol R3	OP-S
	Force (N)		20	20	20	20	20
	Time (min)		Until Plane	0.5	0.5	2	1.5

[1]Plane grinding
[2]Fine grinding
[3]Diamond polishing
[4]Oxide polishing

A.2 Skeletal Density Calibration Report

The calibration report of the pycnometer is shown below.

QUANTACHROME CORPORATION
Upyc 1200e V5.06
Added Volume Calibration Report

Mon Jul 20 09:22:39 2020
User ID: User
Vadded: Small
Flow Purge: 1.0 min.
Target Pressure: 16.0 psig
Type of gas used: N2
Analysis Temperature: 19.7 C
Blank Deviation Achieved: 0.0004 %
Sphere Deviation Achieved: 0.0006 %
Added Volume: 12.8005 cc
Standard Deviation: 0.0001 cc

Run Data

RUN	Blank PA/PB	Sphere PA/PB
1	1.6630	2.0468
2	1.6634	2.0468
3	1.6632	2.0468
4	1.6630	
5	1.6633	
6	1.6633	
7	1.6633	

Appendix B Results

B.1 Morphology

The morphology of the loose powders observed using a SEM can be seen in this section.

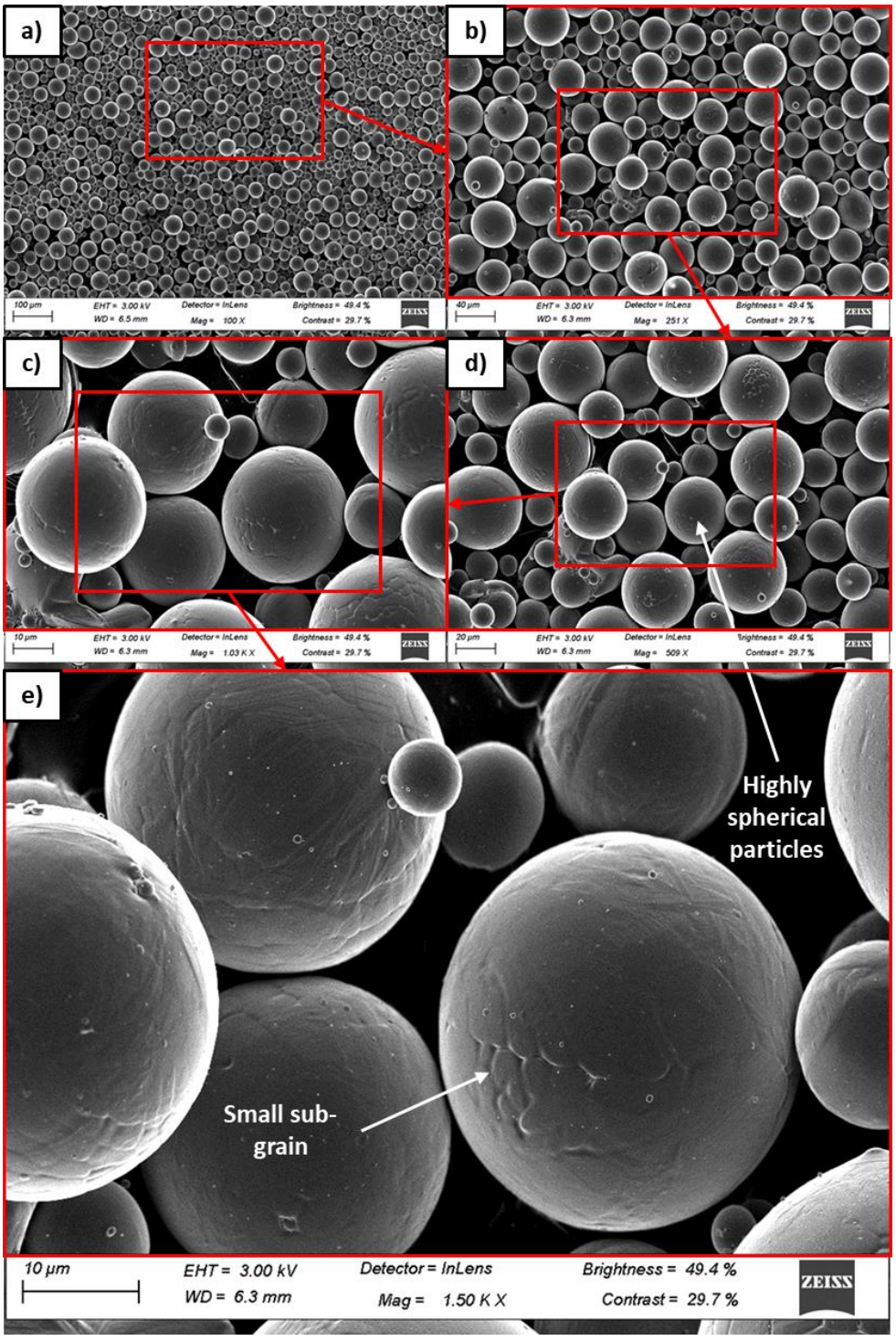

Figure 49: SEM images of PA Ti-6Al-4V powder with scalebars of a) 100 µm, b) 40 µm, c) 10 µm, d) 20 µm, and e) 10 µm

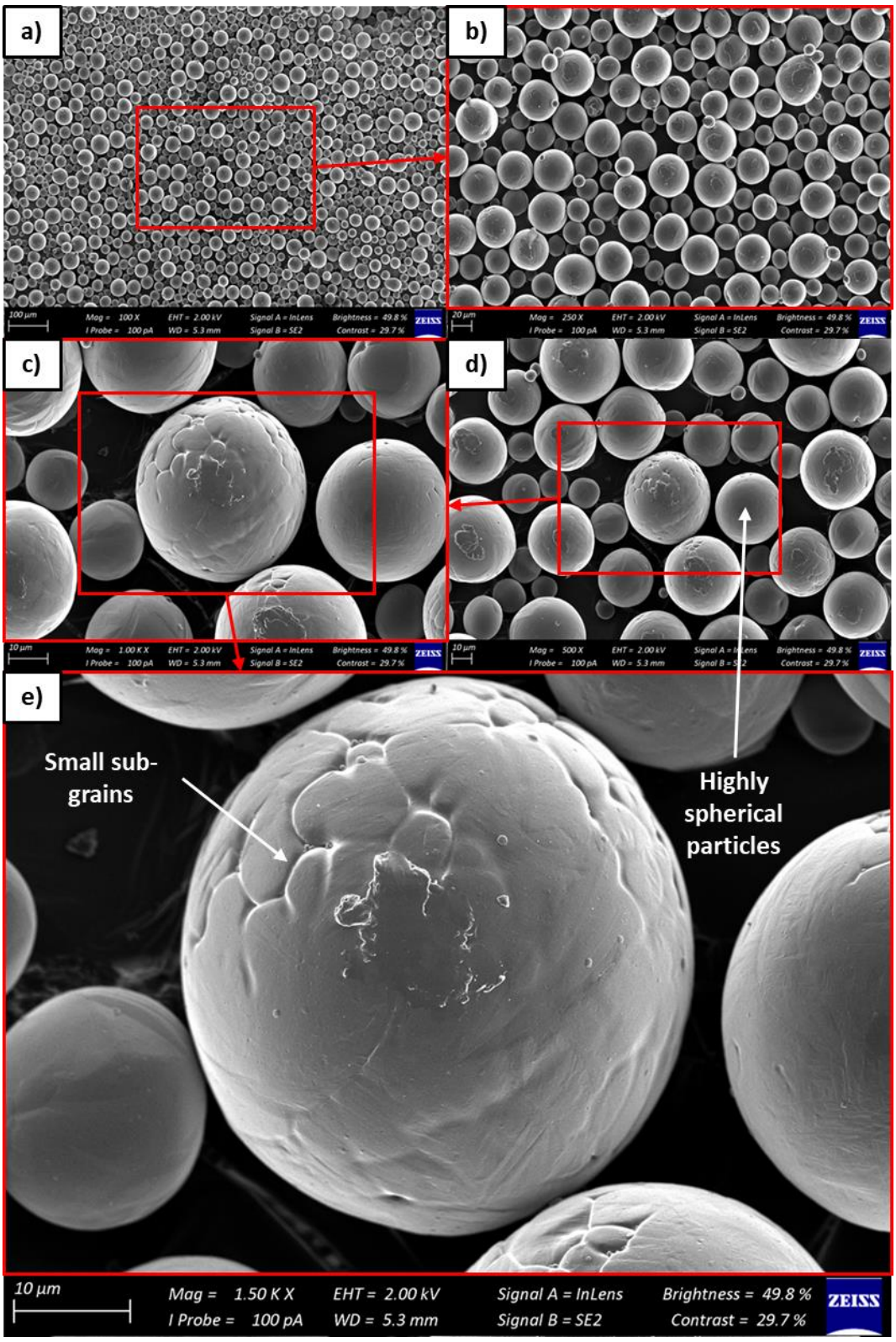

Figure 50: SEM images of CP Ti powder with scalebars of a) 100 µm, b) 20 µm, and c-e) 10 µm

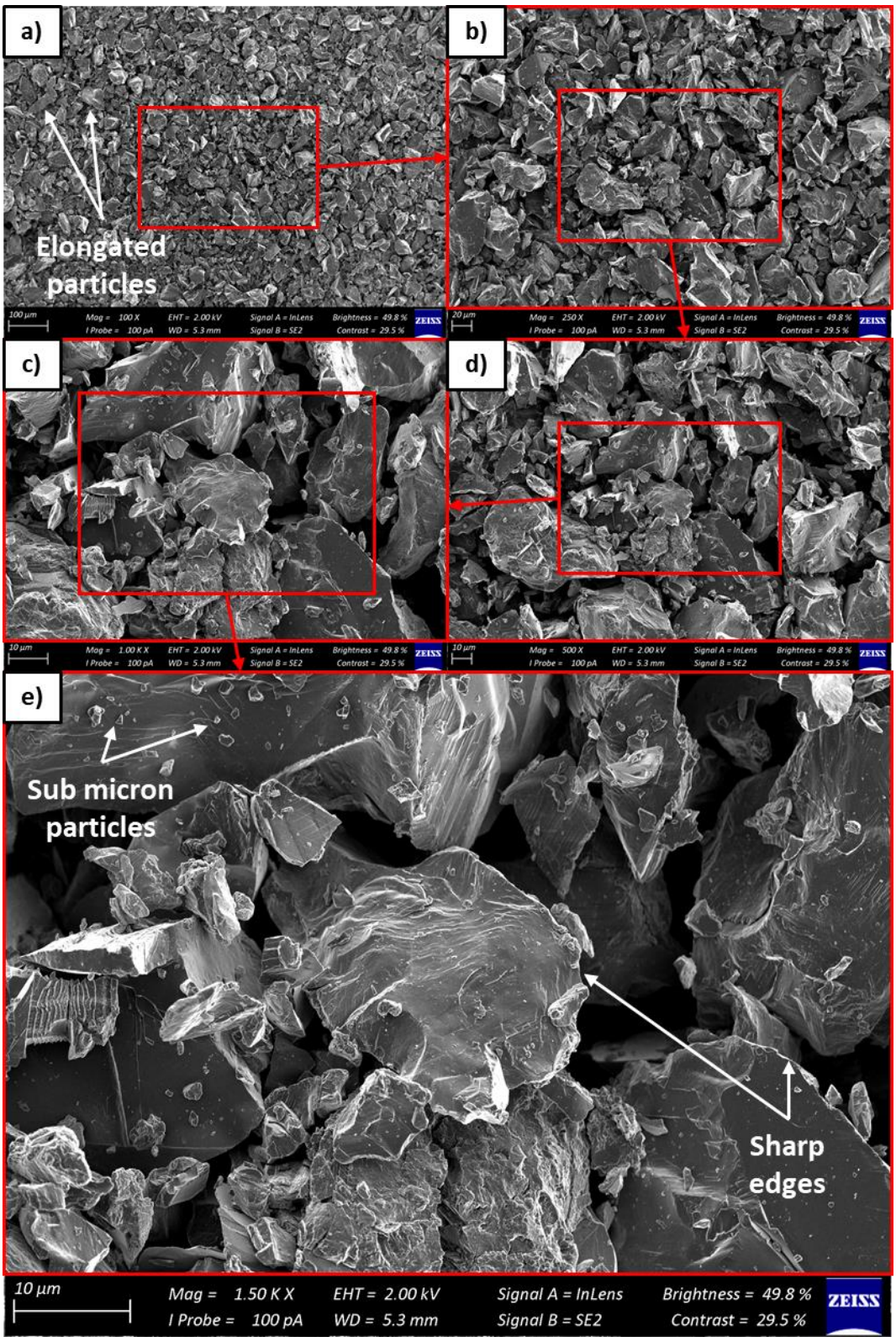

Figure 51: SEM images of MA powder with scalebars of a) 100 µm, b) 20 µm, and c-e) 10 µm

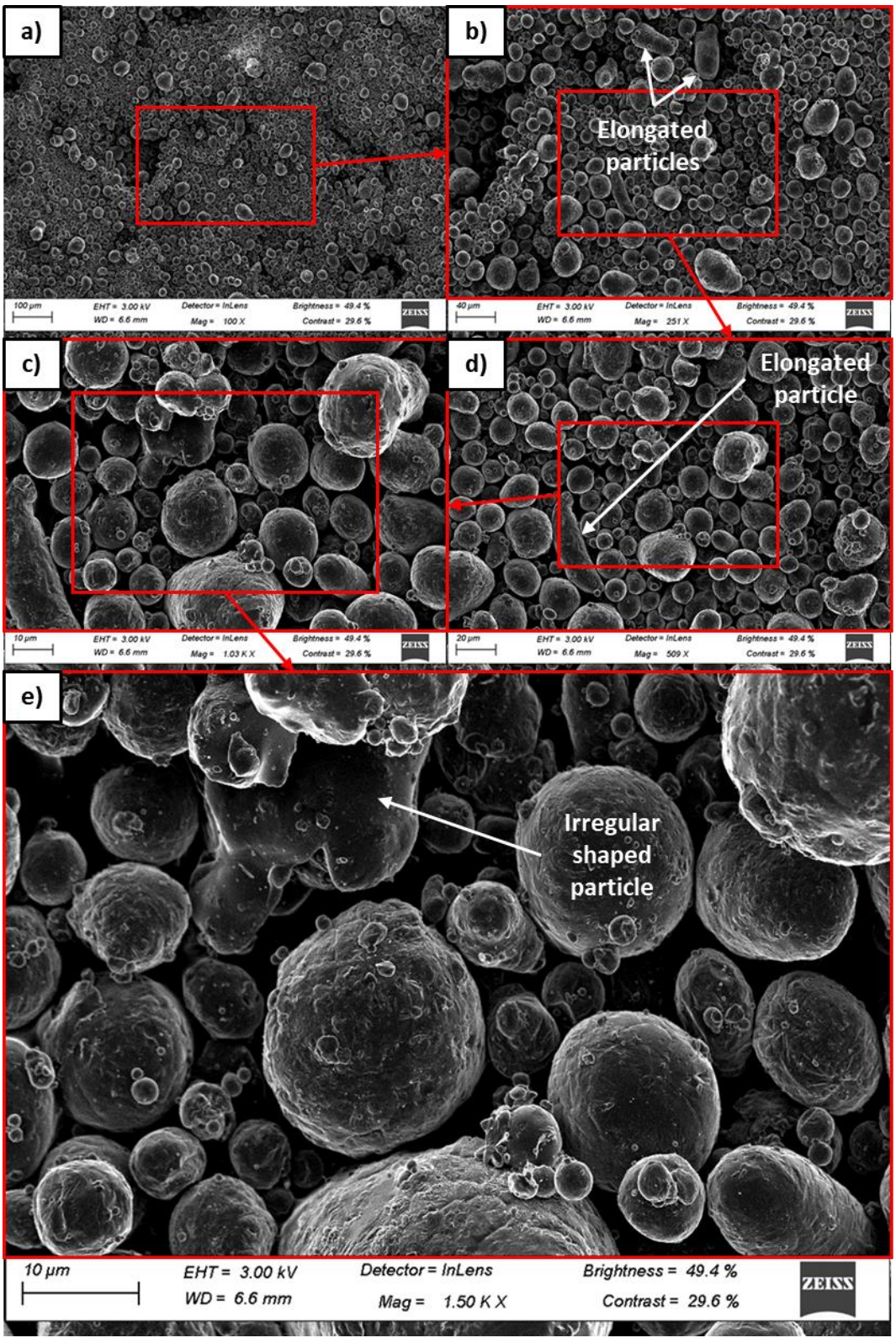

Figure 52: SEM images of Al powder with scalebars of a) 100 µm, b) 40 µm, c) 10 µm, d) 20 µm, and e) 10 µm

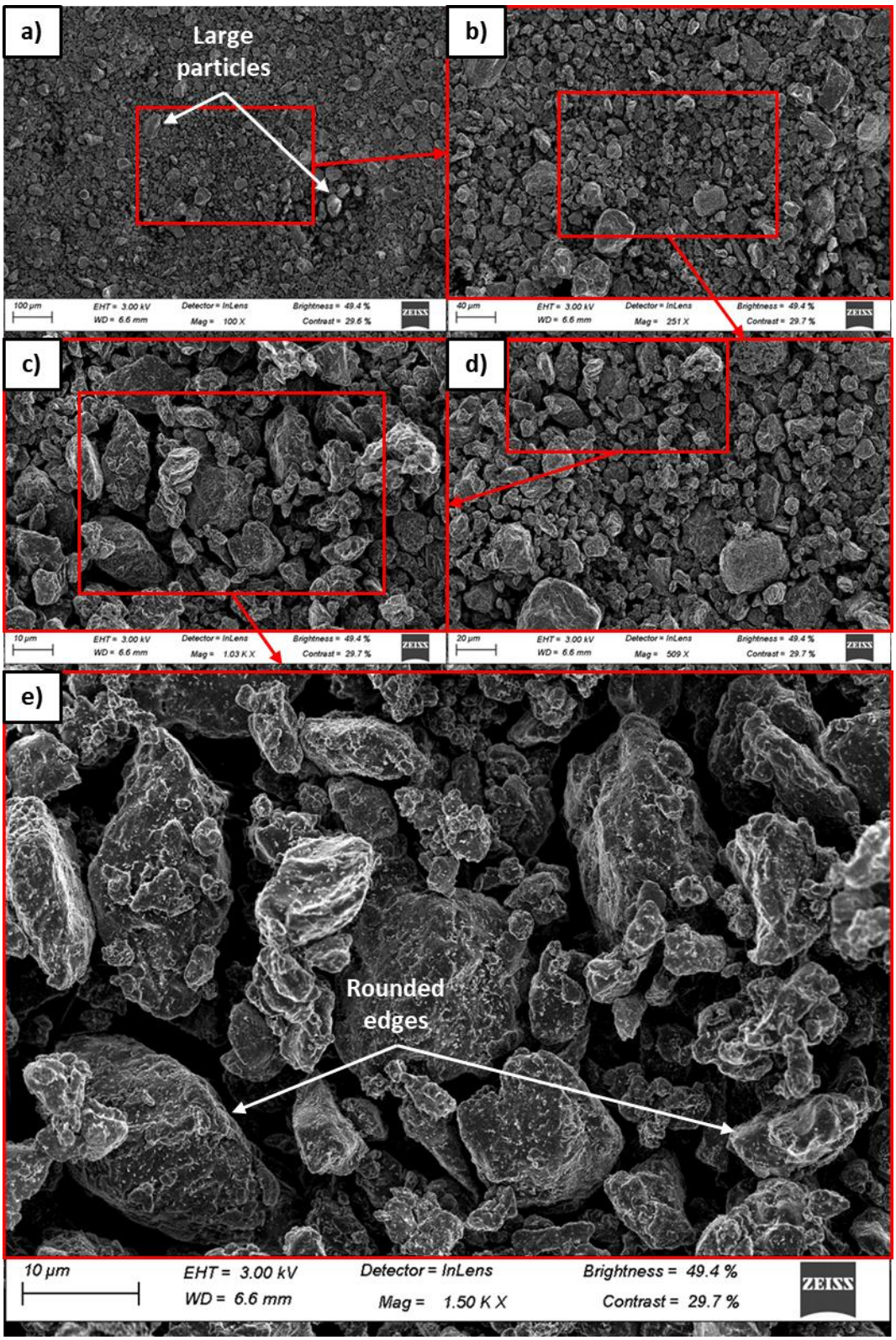

Figure 53: SEM images of V powder with scalebars of a) 100 µm, b) 40 µm, c) 10 µm, d) 20 µm, and e) 10 µm

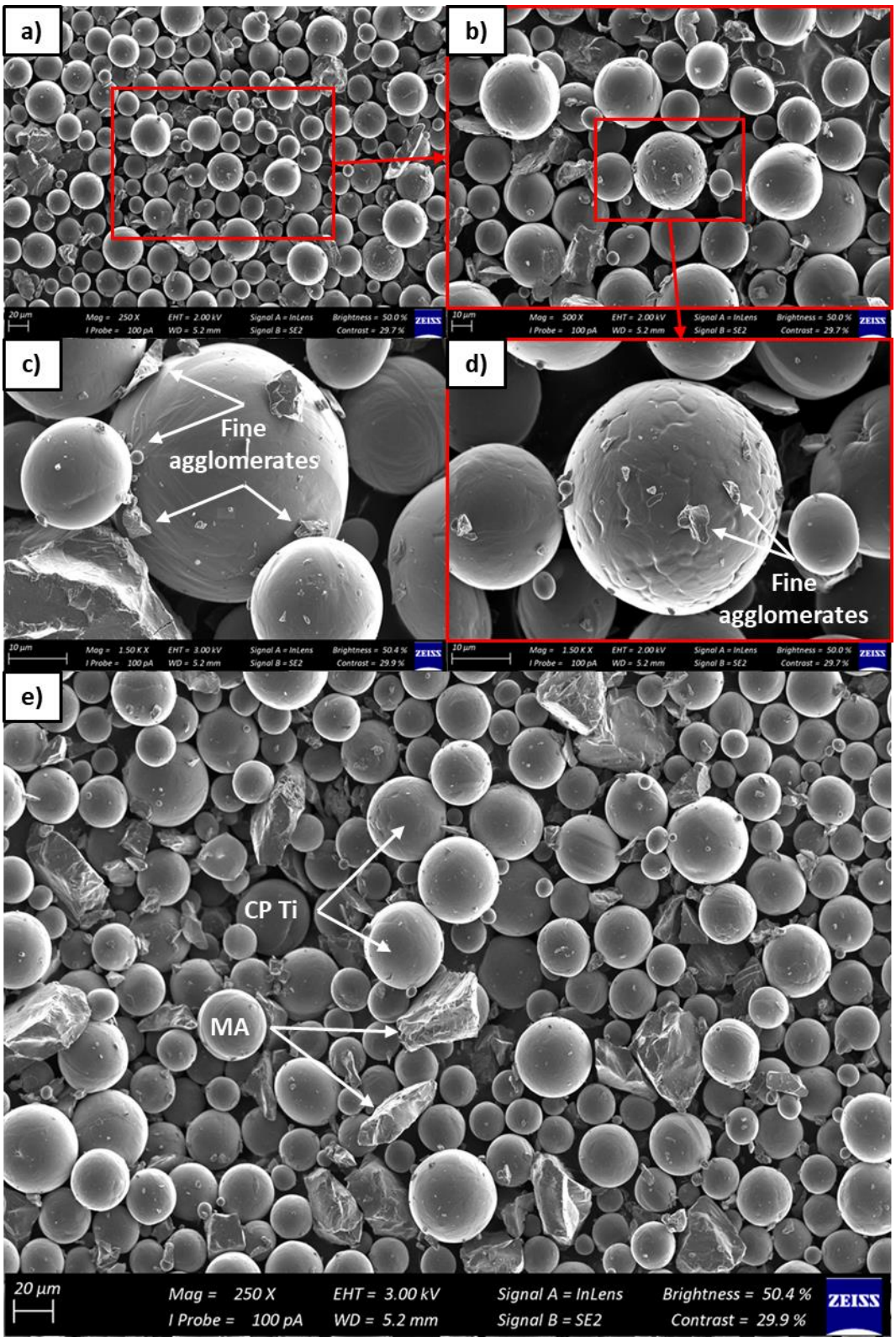

Figure 54: SEM images of powder Blend 1 MA with scalebars of a) 20 µm, b-d) 10 µm, and e) 20 µm

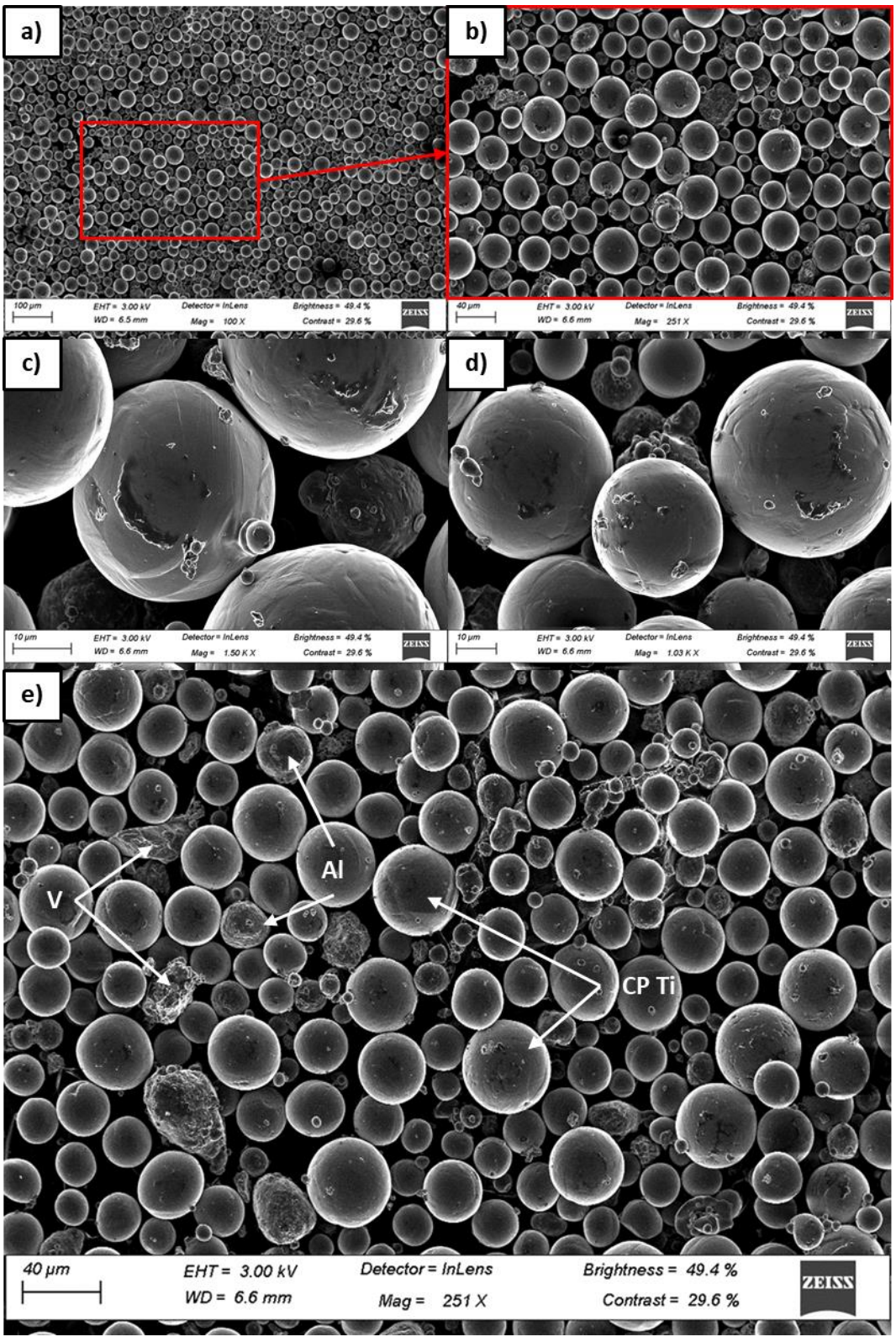

Figure 55: SEM images of powder Blend 2 BE with scalebars of a) 100 µm, b) 40 µm, c-d) 10 µm, and e) 40 µm

B.2 Angle of Repose

The AoR measurements of the CP Ti, MA, Al, V, Blend 1 MA, and Blend 2 MA are shown in this section.

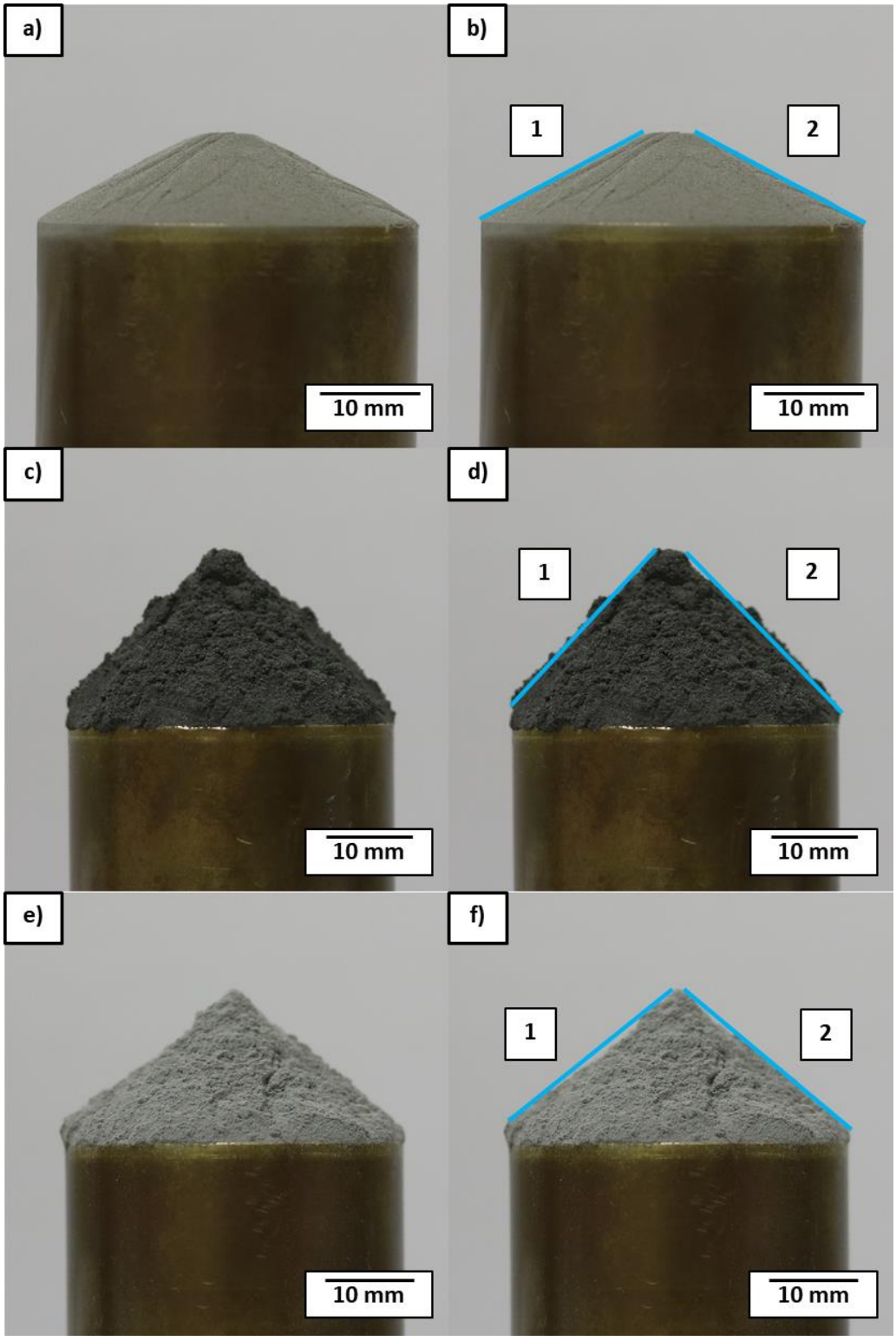

Figure 56: AoR measurements of a-b) CP Ti, c-d) MA, and e-f) Al powder

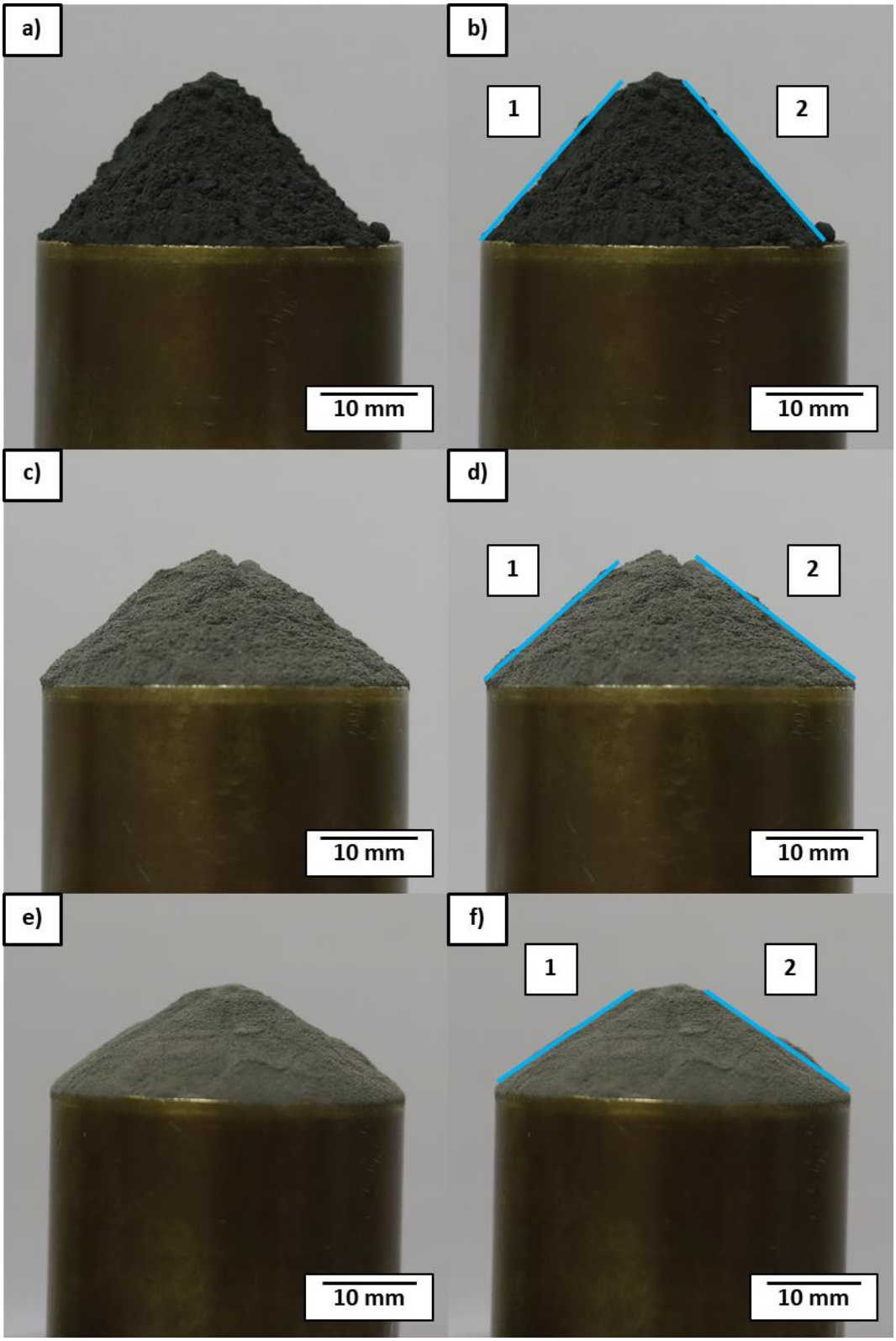

Figure 57: AoR measurements of a-b) V, c-d) Blend 1 MA, and e-f) Blend 2 BE powder

Appendix C Spreadability Test Rig

All resources for the custom designed spreadability test rig are detailed in this section. The sections include: the Arduino code used to control the rig; calculations for the speed of the recoater blade; the rig wiring diagram; details of various electrical components used; the MATLAB code used for the image processing; and the binary image results.

C.1 Arduino Code

```
//Spreadability Test Rig
//Author: Ben Parker
//2 buttons to control a stepper motor. Added limit switches.
//Uploaded to Spread tester on 20/11/2019

const int stepPin = 3; //Stepper Driver
const int dirPin = 2; //Stepper Driver
int forward = 5; //Left Button
int backward = 4; //Right Button
int limit_switch_forward = 6; //Stop forward
int limit_switch_backward = 7; //Stop backward

boolean current_forward = LOW;
boolean last_forward=LOW;
boolean last_backward = LOW;
boolean current_backward = LOW;

void setup() {
  Serial.begin(9600);

  pinMode(stepPin,OUTPUT);  //declare stepper driver comms
  pinMode(dirPin,OUTPUT);
  pinMode(forward, INPUT);  //declare buttons
  pinMode(backward, INPUT);
  pinMode(limit_switch_forward, INPUT); //declare limit switch forward
  pinMode(limit_switch_backward, INPUT); //declare limit switch backward
}

//De-bouncing function for all buttons used to check the state of each
button
boolean debounce(boolean last, int pin)
{
  boolean current = digitalRead(pin);
  if (last != current)
   {
      delay(50);
      current = digitalRead(pin);
   }
  return current;
}

void loop() {
  current_forward = debounce(last_forward, forward);          //Debounce
for forward button
  current_backward = debounce(last_backward, backward);
//Debounce for backward button

  int distance = 3*800; //1 revolution = 800
```

```
  int delay_speed = 300; //300 us = 150 mm/s

  if (last_forward== LOW && current_forward == HIGH) //FORWARD
  {
    digitalWrite(dirPin,LOW); //direction forward

    for (int i = 0; i < distance; i++)
    {
       Serial.println(1);

       digitalWrite(stepPin,HIGH); //move forward
       delayMicroseconds(delay_speed);
       digitalWrite(stepPin,LOW);
       delayMicroseconds(delay_speed);

       if (digitalRead(limit_switch_forward) == LOW)
       {
          Serial.println(3);
          digitalWrite(dirPin,HIGH);
          for (int i = 0; i < 80; i++)
          {
            digitalWrite(stepPin,HIGH); //move backward
            delayMicroseconds(delay_speed*3);
            digitalWrite(stepPin,LOW);
            delayMicroseconds(delay_speed*3);
          }
          break;
       }
    }
  }
  last_forward=current_forward;

  if (last_backward== LOW && current_backward == HIGH) //BACKWARD
  {
    digitalWrite(dirPin,HIGH); //direction backward

    for (int i = 0; i < distance; i++)
    {
       Serial.println(2);

       digitalWrite(stepPin,HIGH); //move backward
       delayMicroseconds(delay_speed);
       digitalWrite(stepPin,LOW);
       delayMicroseconds(delay_speed);

       if (digitalRead(limit_switch_backward) == LOW)
       {
          Serial.println(4);
          digitalWrite(dirPin,LOW);
          for (int i = 0; i < 80; i++)
          {
            digitalWrite(stepPin,HIGH); //move forward
            delayMicroseconds(delay_speed*3);
            digitalWrite(stepPin,LOW);
            delayMicroseconds(delay_speed*3);
          }
          break;
       }
    }
  }
  last_backward=current_backward;
}
```

C.2 Stepper Motor Delay Calculation

The calculations used to determine the delay required for the variable of "delay_speed" in the Arduino code, Section C.1, is shown below.

Motor pulley: Timing pulley GT2 Bore 5mm - 36T

$N := 36$ number of teeth

$p := 2\,mm$ pitch

Required Velocity

$V := 150\,\frac{mm}{s}$

Stepper Driver Resolution

$N_{resolution} := 800$ quarter step resolution

$N_{delay} := 2$ Number of delays in one step - Arduino code

Calculations

$D_{pitch} := \frac{p \cdot N}{\pi} = 22,9183\,mm$ pitch diameter of the pulley

$C := \pi \cdot D_{pitch} = 72\,mm$ circumference of the pitch diameter

Therefore the crossbeam will move 72 mm per rotation

$N_{rotations} := \frac{V}{C} = 2,0833\,Hz$ number of rotations required to move the crossbeam 150 mm

$N_{steps} := N_{resolution} \cdot N_{rotations} = 1666,6667\,Hz$ number of steps required

$delay := \frac{1}{N_{delay} \cdot N_{steps}} = 300\,\mu s$ delay in microseconds

C.3 Spreadability Test Rig – CAD Design

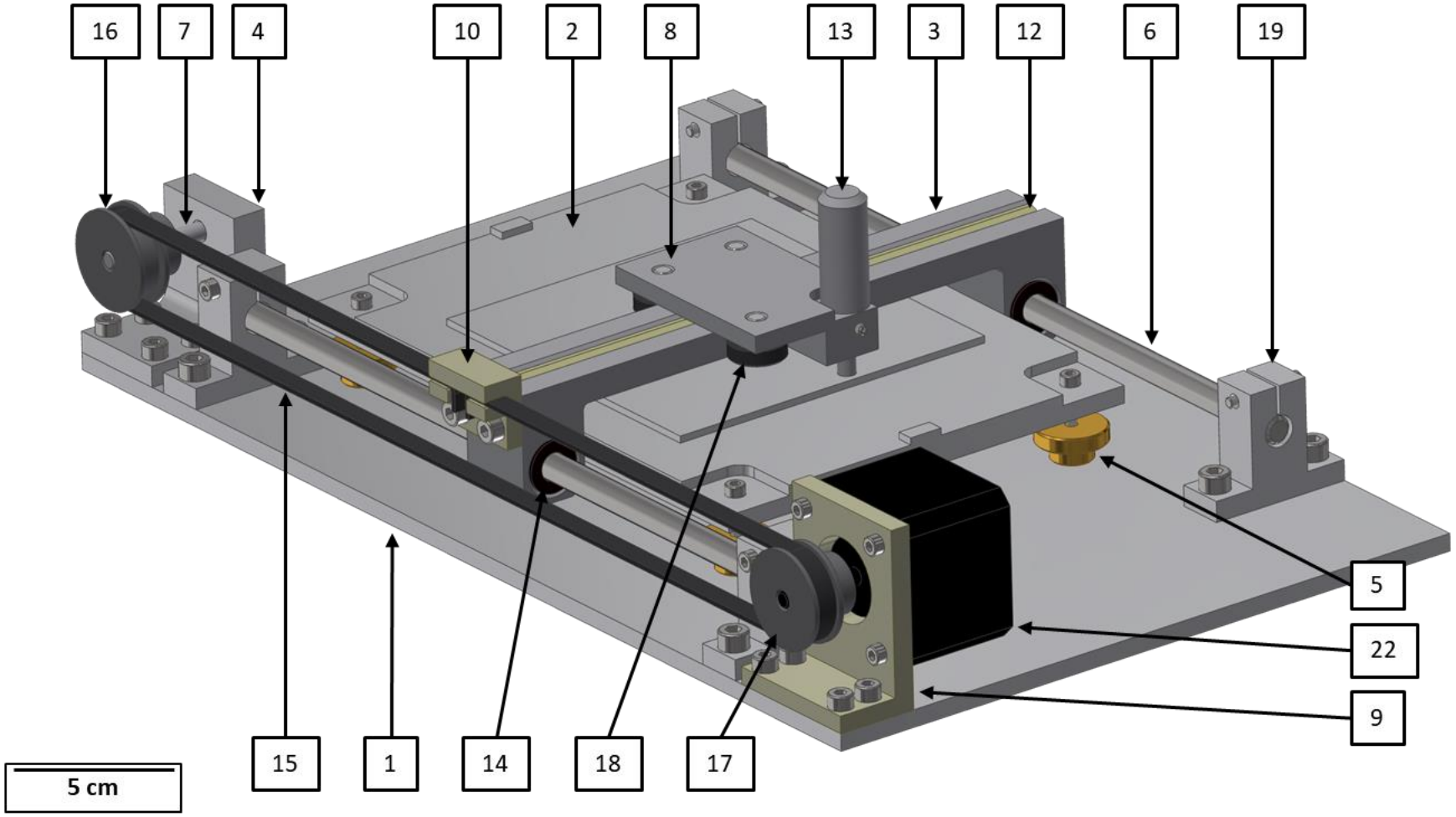

Figure 58: Labelled CAD design of the spreadablity test rig

C.4 Spreadability Test Rig Wiring Diagram

The wiring diagram of the spreadability test rig, generated using Fritzing [127] is seen in Figure 59.

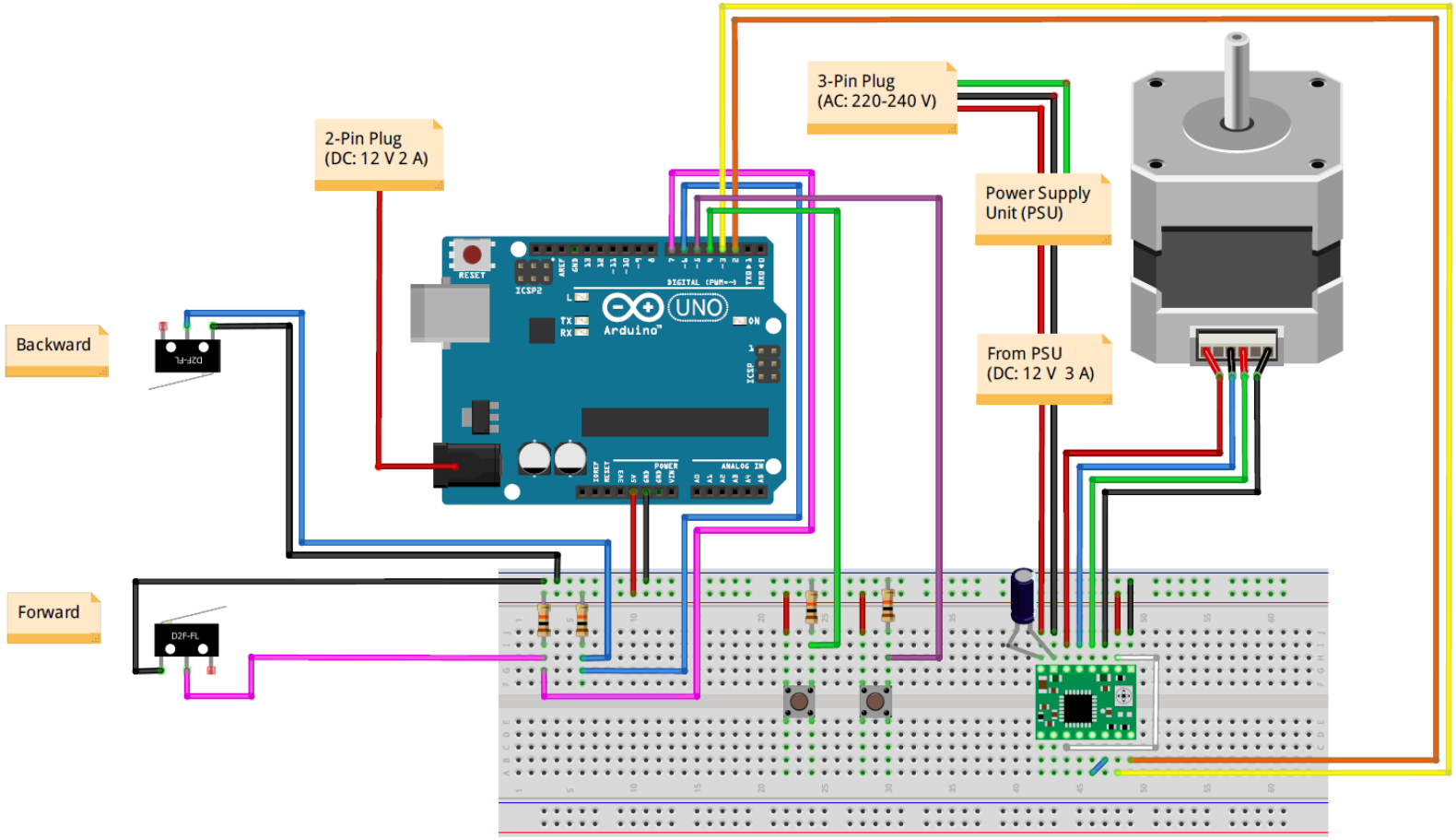

Figure 59: Wiring diagram of the custom built spreadability test rig

C.5 Spreadability Electrical Components

The wiring schematic of the Pololu 1A stepper motor driver, in full-step mode, can be seen in Figure 60.

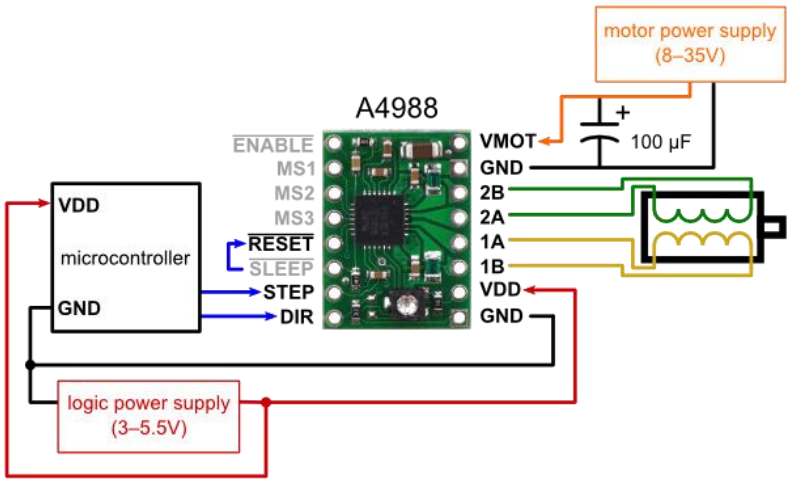

Figure 60: Pololu 1A stepper motor driver wiring schematic

The MS1-3 pins in Figure 60 can be used to enable micro-stepping in the attached stepper motor. The default state is when the MS1-3 pins are disconnected, which results in a full-step resolution. Each pin can be connected to 5V, with different combinations leading to associated micro-stepping resolutions. The summary of these combinations can be seen in Figure 61, with "High" being connected to 5 V and "Low" being disconnected.

MS1	MS2	MS3	Microstep Resolution
Low	Low	Low	Full step
High	Low	Low	Half step
Low	High	Low	Quarter step
High	High	Low	Eighth step
High	High	High	Sixteenth step

Figure 61: Pololu 1A micro-stepping table

Figure 59 can clearly be seen to make use of a quarter step resolution as the MS2 pin is connected to the 5 V power supply. It must be noted that when changing the

micro-stepping of the driver, the associated Arduino code “distance” parameter will have to change.

C.6 Spreadability – Image processing using MATLAB

```
%% Spreadability image thresholding
% Ben Parker, September 2020
clearvars; close all; clc;

%% Import image file
rgb = imread('B1-60-1-cropped.JPG'); %Image filename

%% Display image file
figure
imshow(rgb)

%% Convert image file to grayscale
gray = rgb2gray(rgb);
figure
imshow(gray)

%% Convert image to binary
%Global imbinarize
BW = imbinarize(gray,'global'); %This is used for the
majority of images

%%Global imbinarize: used when global fails to convert to
binary accurately
tol = 0.6; %Sensitivity tolerance for imbinarize
%BW =
imbinarize(gray,'adaptive','ForegroundPolarity','bright','Se
nsitivity',tol);

%% Display binary images
figure  %Pure binary image to be saved to file
imshow(BW)

figure %Side by side grayscale image and binary conversion
for comparison of fit
subplot(1,2,1), imshow(gray)
subplot(1,2,2), imshow(BW)

%% Percent coverage calculation
total_pixels = numel(BW); %Total number of pixels in the
image
powder_pixels = sum(BW(:) == 0); %Number of black pixels
coverage = (powder_pixels/total_pixels)* 100 %Ratio of black
pixels over total = percent coverage
```

C.7 Spreadability Test Rig – Percent Coverage Results

The percent coverage test results from the spreadability test rig are displayed in this section. Two overhead images of the 10x10 cm build plate were captured at each layer height and the layer heights were 60, 80, 100, and 150 µm.

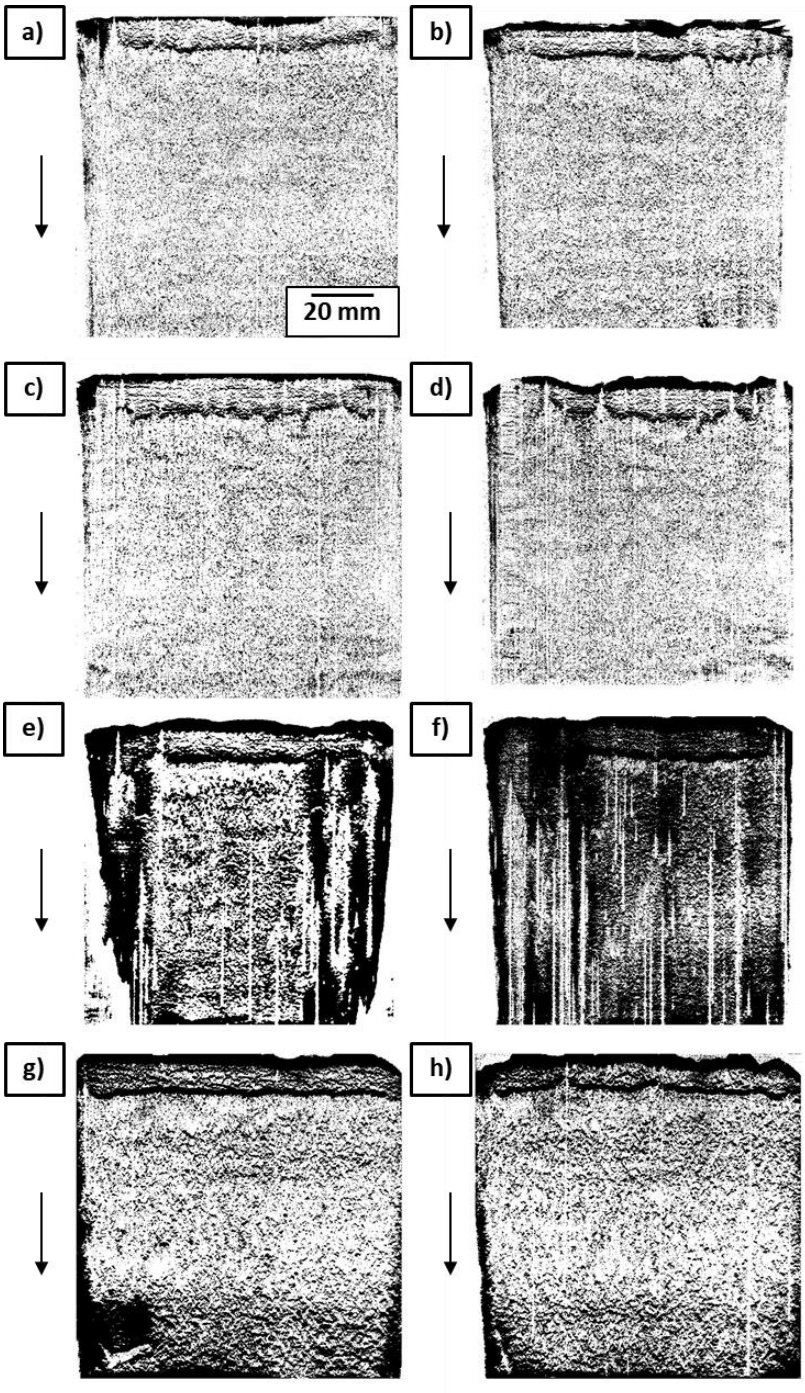

Figure 62: PA Ti-6Al-4V powder spread layer height of a-b) 60 µm, c-d) 80 µm, e-f) 100 µm, g-h) 150 µm

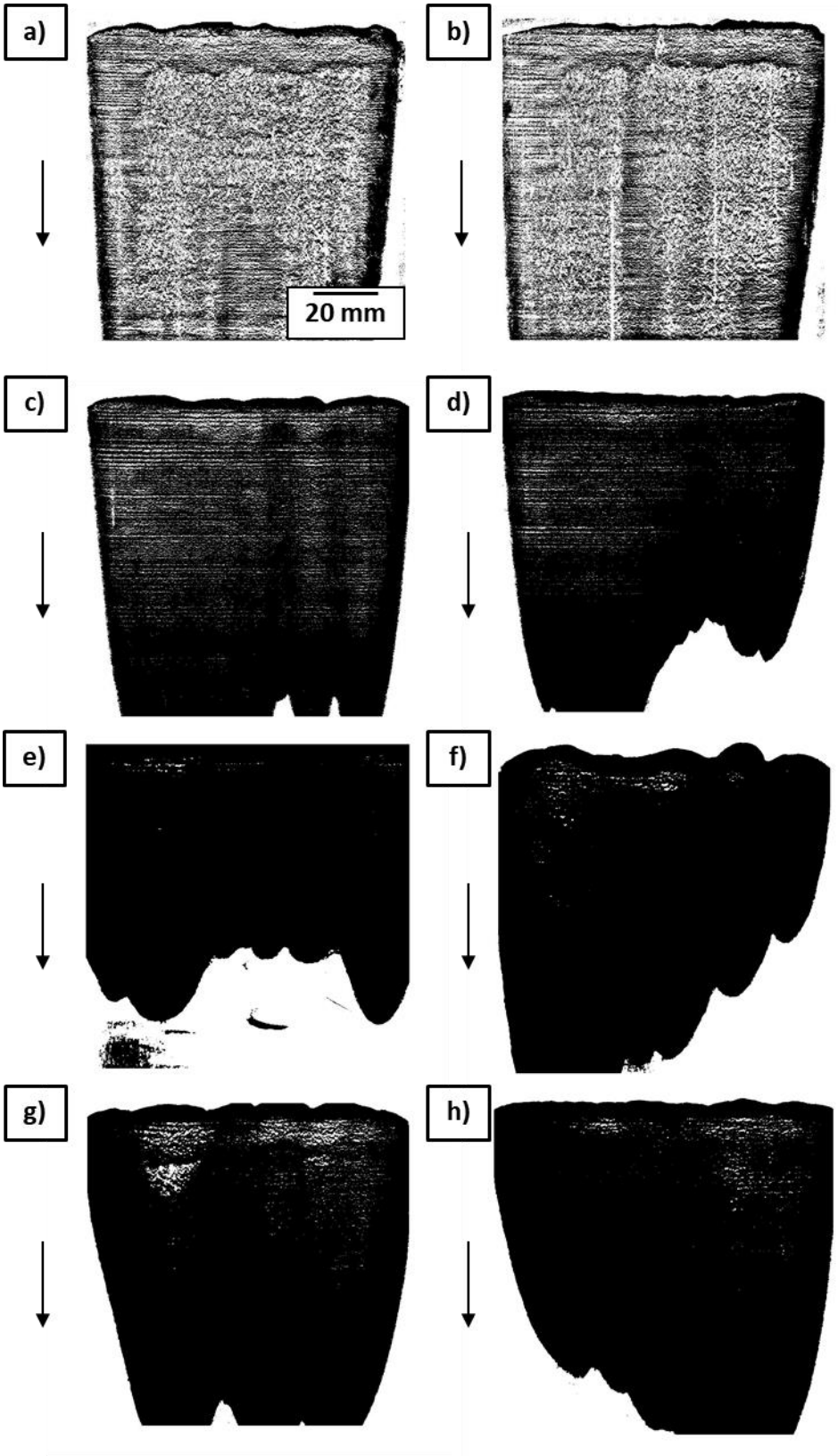

Figure 63: Dried PA Ti-6Al-4V powder spread layer height of a-b) 60 µm, c-d) 80 µm, e-f) 100 µm, g-h) 150 µm

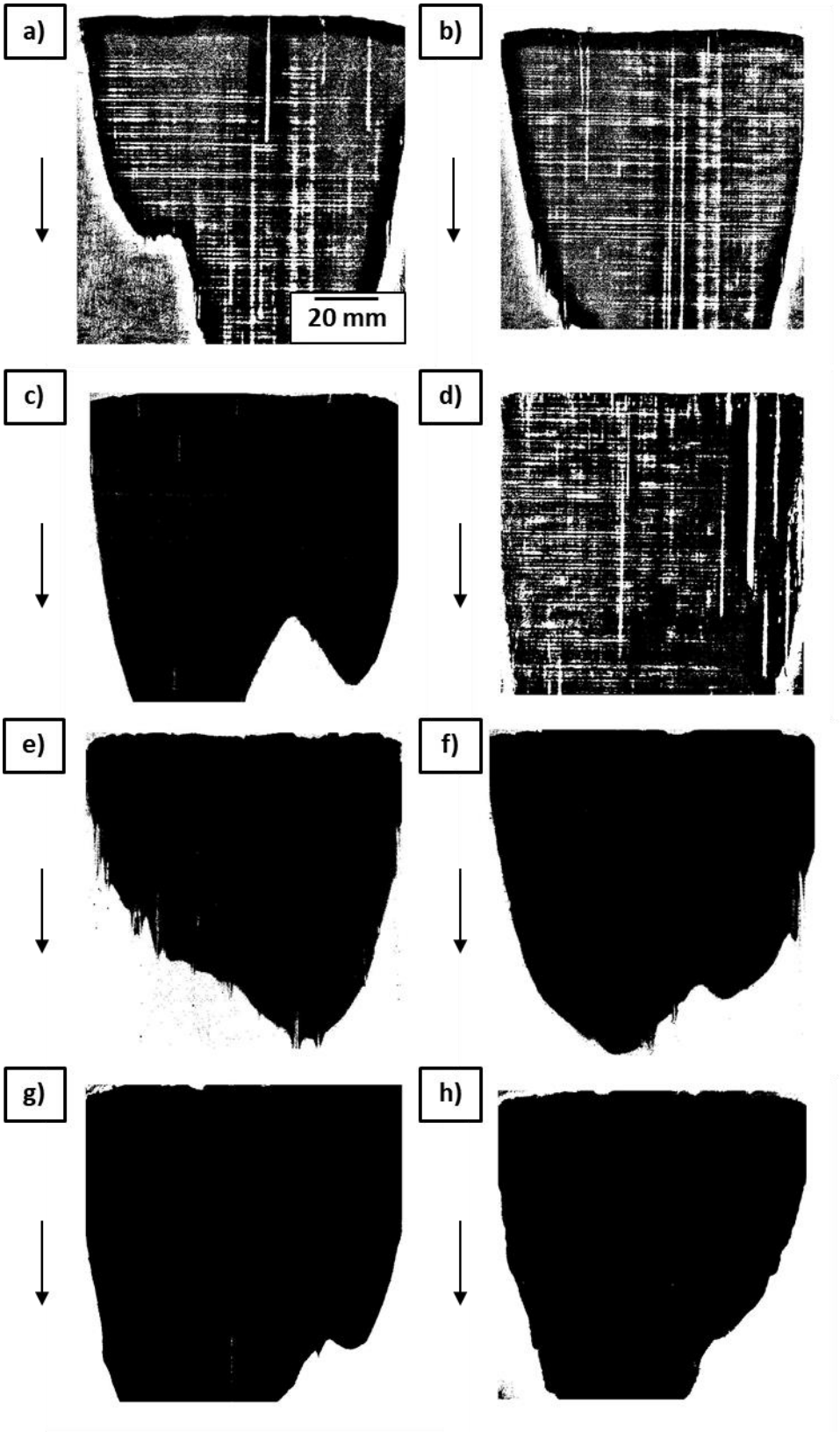

Figure 64: CP Ti powder spread layer height of a-b) 60 µm, c-d) 80 µm, e-f) 100 µm, g-h) 150 µm

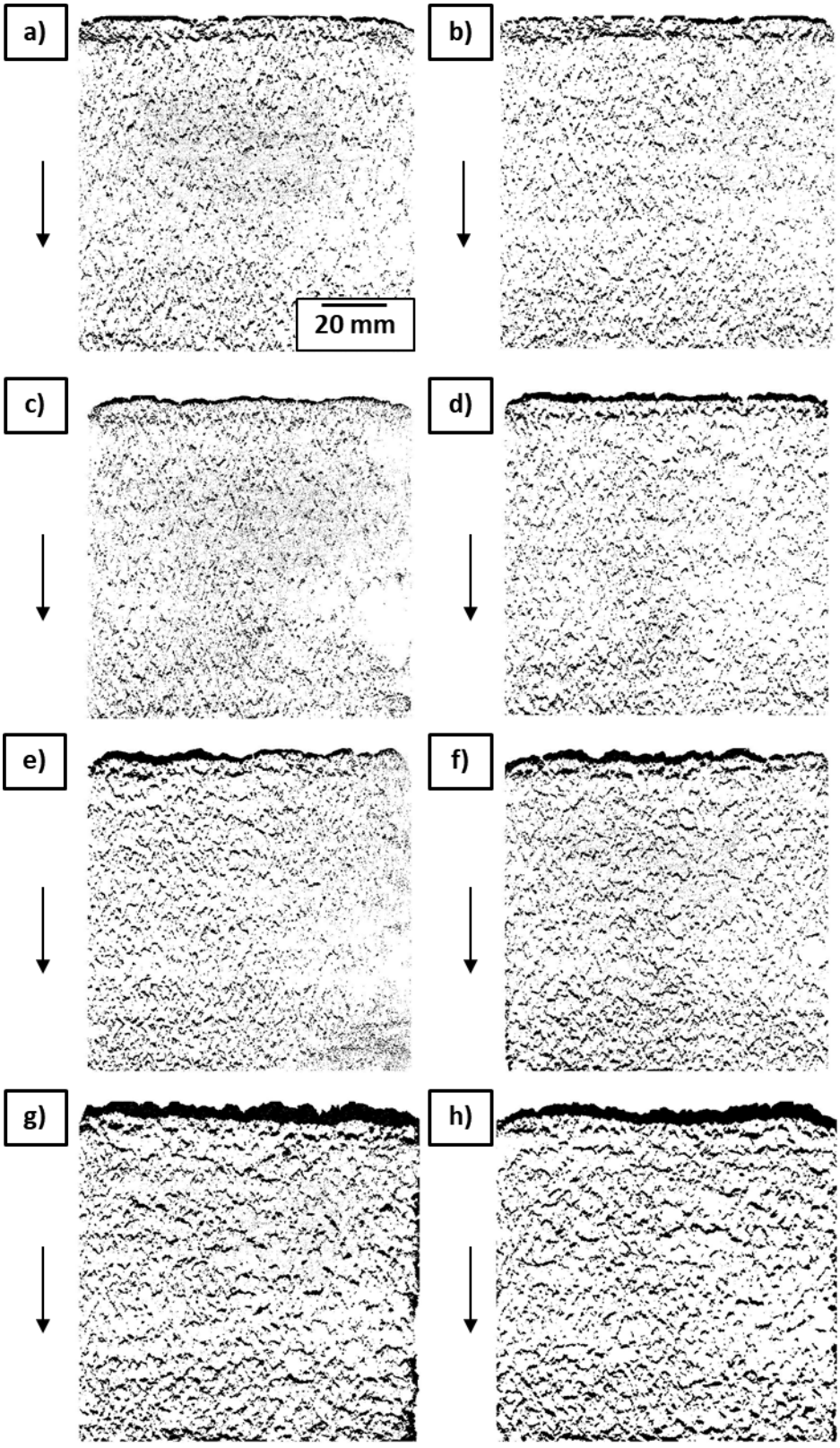

Figure 65: MA powder spread layer height of a-b) 60 µm, c-d) 80 µm, e-f) 100 µm, g-h) 150 µm

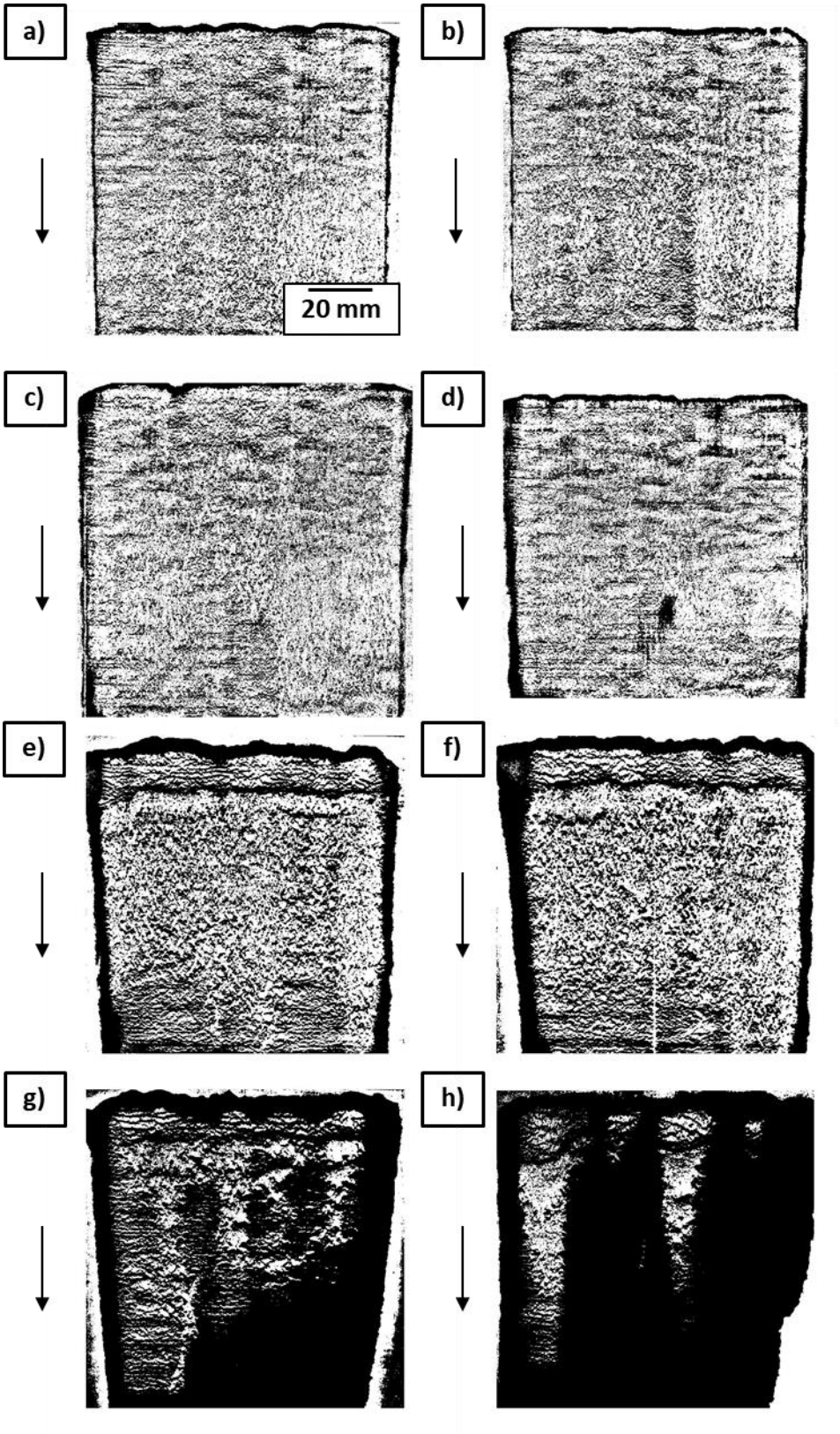

Figure 66: Al powder spread layer height of a-b) 60 µm, c-d) 80 µm, e-f) 100 µm, g-h) 150 µm

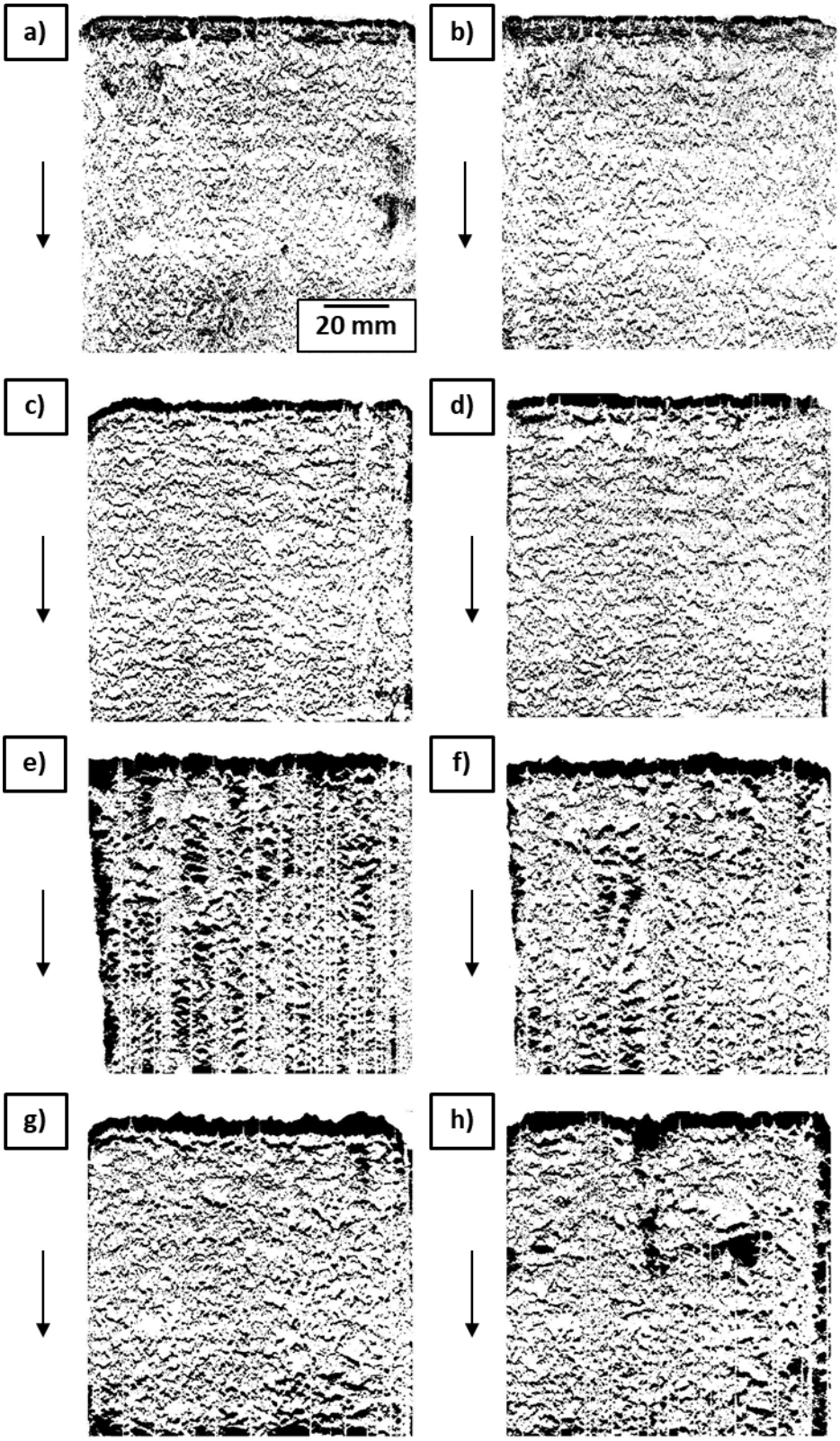

Figure 67: V powder spread layer height of a-b) 60 µm, c-d) 80 µm, e-f) 100 µm, g-h) 150 µm

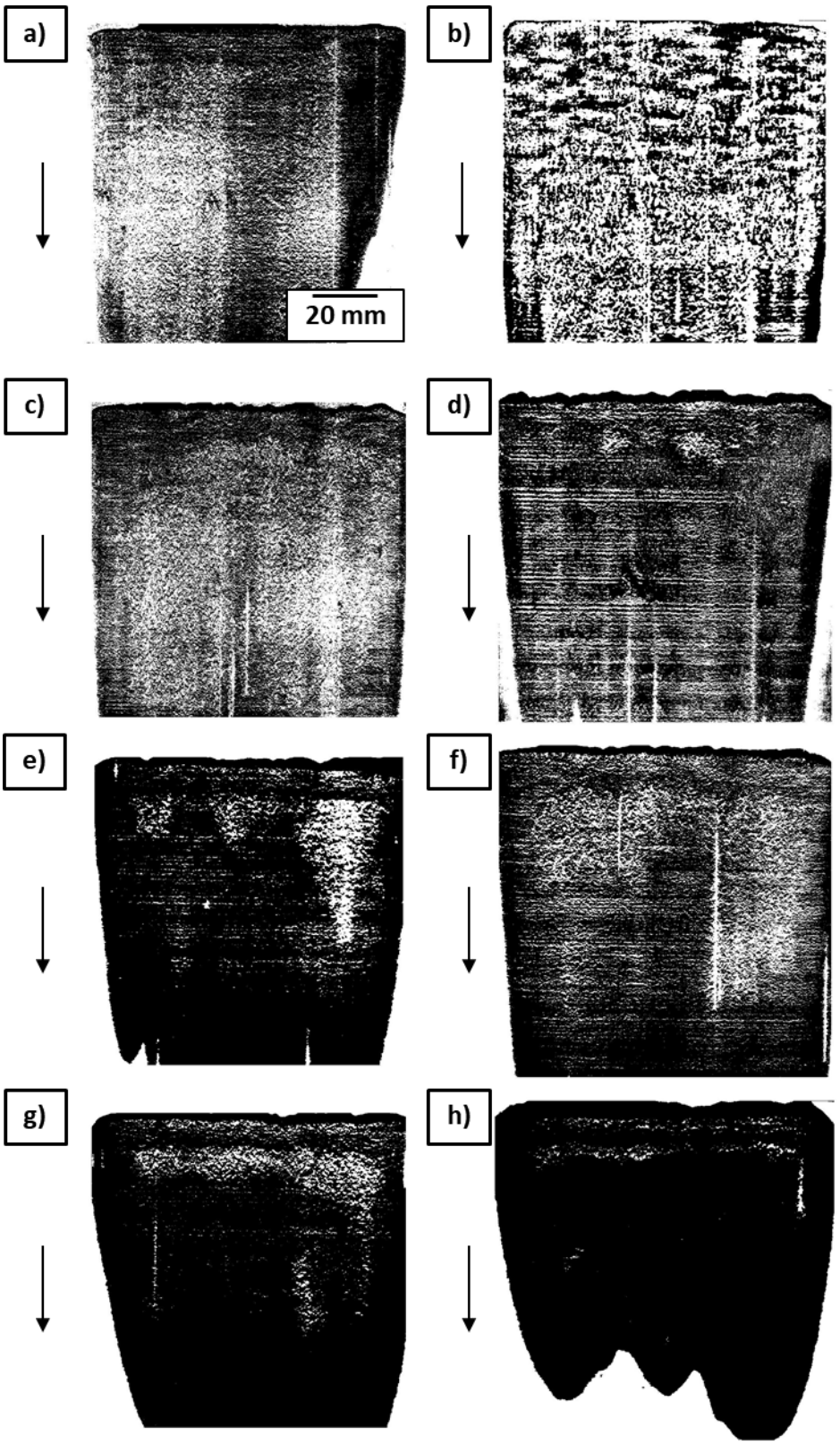

Figure 68: Blend 1 MA powder spread layer height of a-b) 60 µm, c-d) 80 µm, e-f) 100 µm, g-h) 150 µm

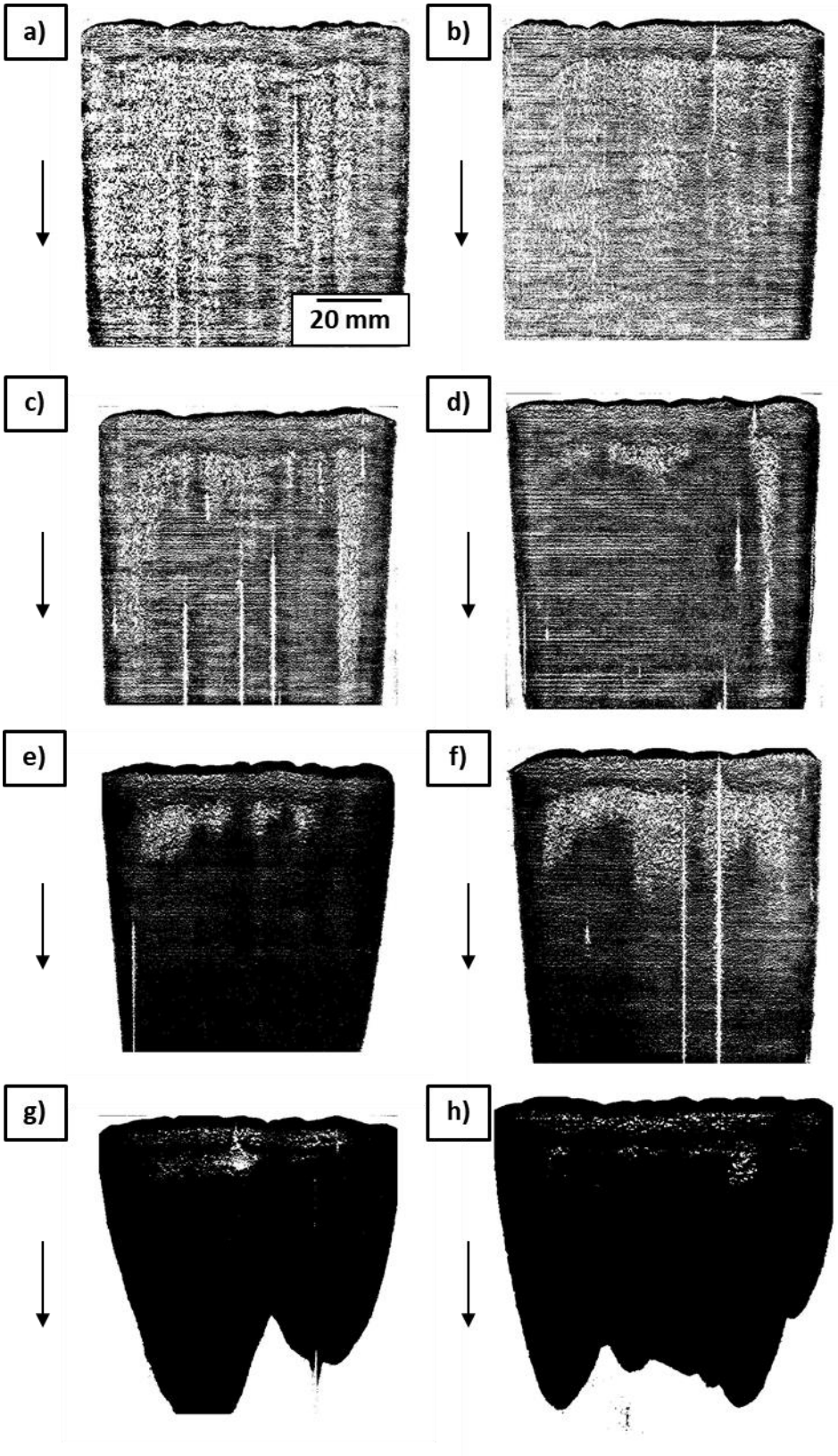

Figure 69: Dried Blend 1 MA powder spread layer height of a-b) 60 µm, c-d) 80 µm, e-f) 100 µm, g-h) 150 µm

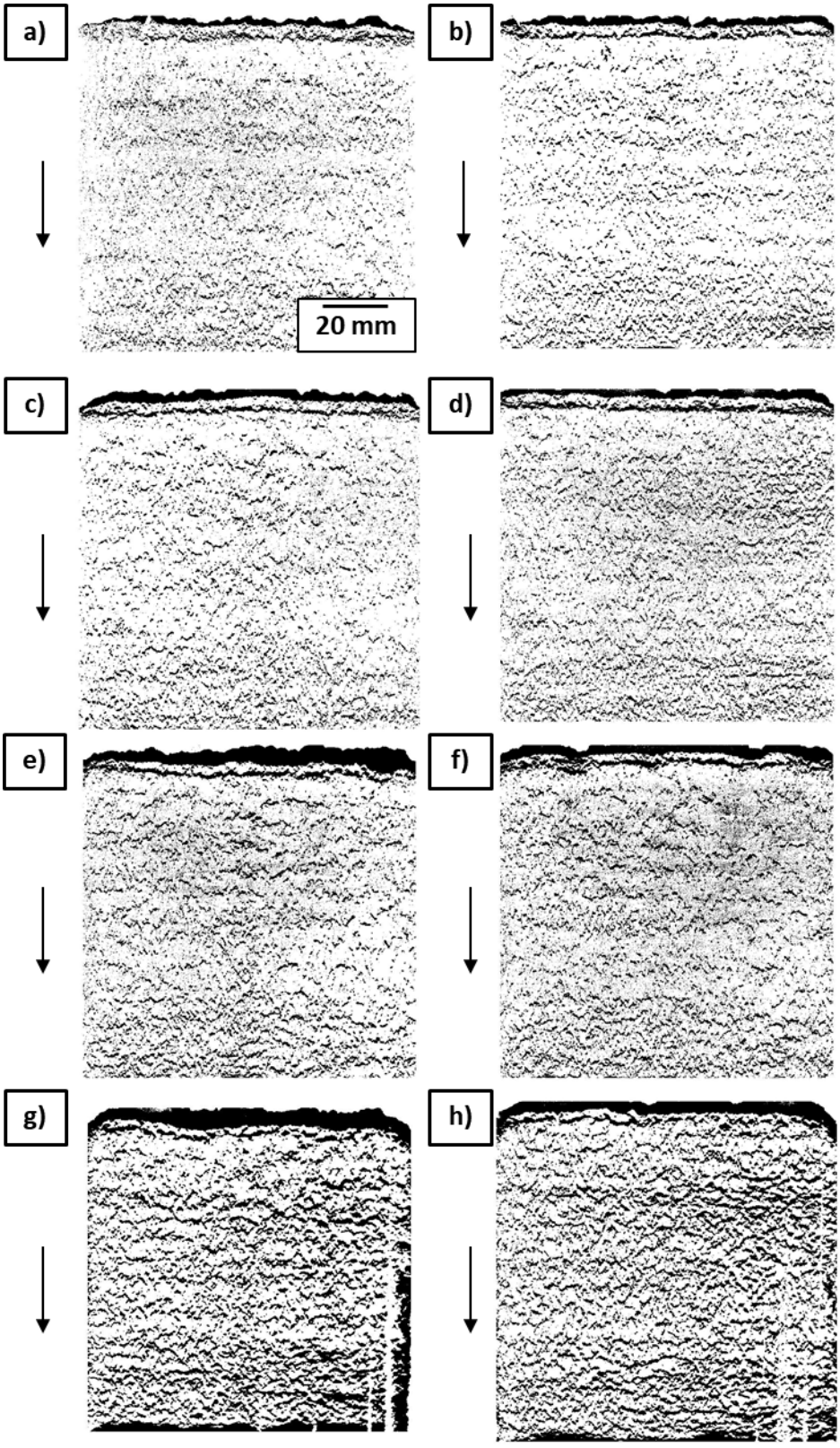

Figure 70: Blend 2 BE powder spread layer height of a-b) 60 µm, c-d) 80 µm, e-f) 100 µm, g-h) 150 µm

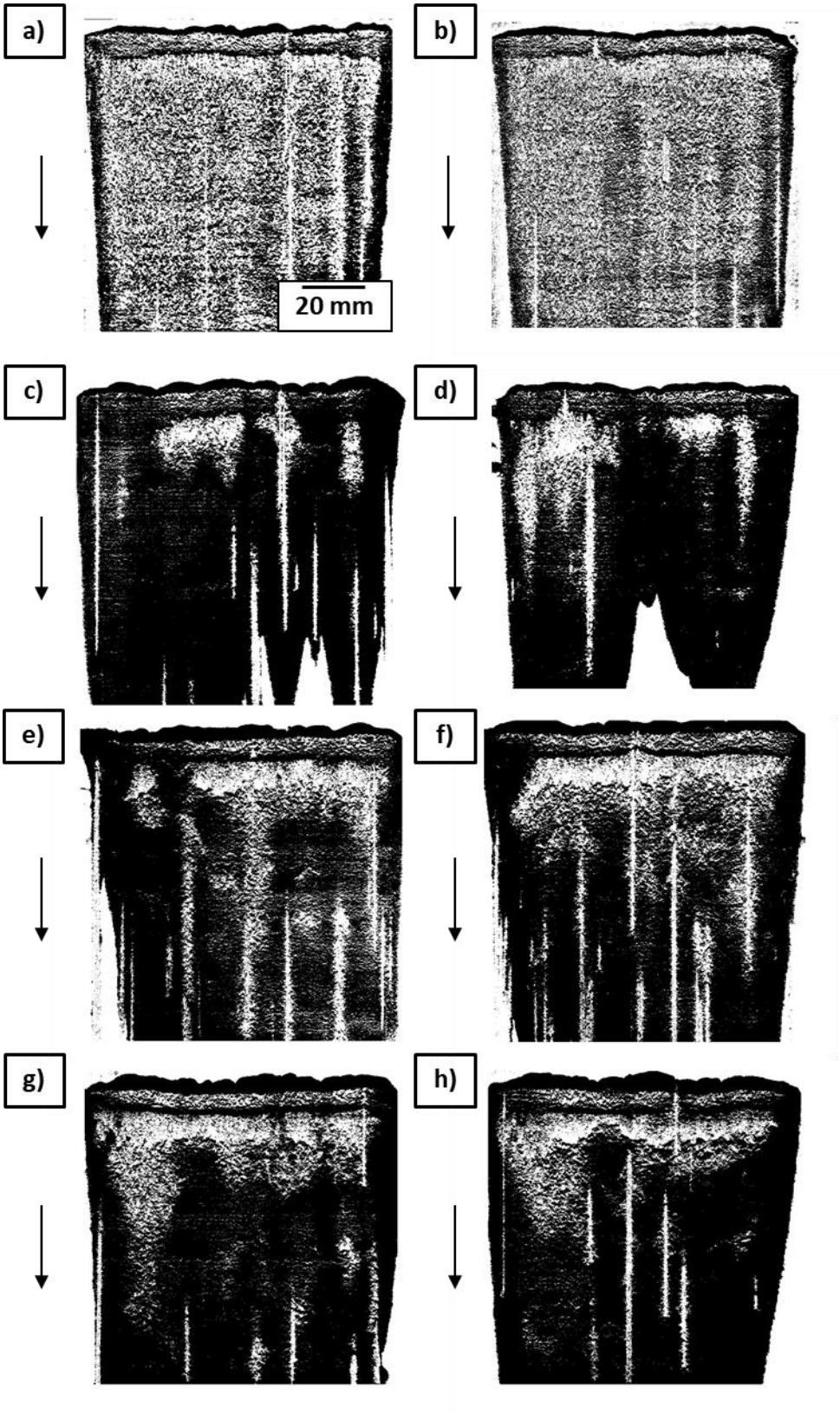

Figure 71: Dried Blend 2 BE powder spread layer height of a-b) 60 µm, c-d) 80 µm, e-f) 100 µm, g-h) 150 µm

Appendix D Testing

The testing documentation for tests conducted externally is found below.

D.1 NECSA ICP-OES and O_2 & N_2 Combustion

Testing completed by NECSA using ICP-OES and O_2 & N_2 Combustion to determine the chemical composition of the master-alloy (60Al-40V) and the CP Ti.

PO Box 582
Pretoria
0001

Analytical & Calibration Services (ACS)

Test Report

necsa
We're in your world

Elias Motsoaledi Street Extension (Church Street West)
R104 Pelindaba

Laboratory Reference Number:		PS2020-0074/1
Quotation Reference Number:		PQ2019-0325 (Ver 1)
Client Order Number:		E238580
Client:	**Contact:**	WB du Preez
	Company:	Central University of Technology, Free State (CUT)
	Address:	Room 228, ZR Mahabane
		20 President Brand Street
	Telephone:	051 507 3556
	Fax:	051 507 3254
Dates:	**Received:**	2020-01-20
	Analysed:	2020-02-24
	Reported:	2020-02-24
Remarks:		

Analysts & Authorisers

Analyst(s):	
LTT Motaung (Thato)	Technical Signatory
S Sibiya (Simanga)	Technical Signatory

Checked by:	
LTT Motaung (Thato)	Technical Signatory
S Sibiya (Simanga)	Technical Signatory

Test Report

Sample ID: PS2020-0074X001 **Sample Name:** MA-AL-V

Determination	Result	Units	Method Used	Uncertainty
Aluminium (Al)	54.8	%_m/m	ICP-OES Analysis - FULL Report	
Iron (Fe)	0.64	%_m/m	ICP-OES Analysis - FULL Report	
Titanium (Ti)	<0.10	%_m/m	ICP-OES Analysis - FULL Report	
Vanadium (V)	43.4	%_m/m	ICP-OES Analysis - FULL Report	
Oxygen	0.18	%(m/m)	O2 & N2 - Combustion	
Nitrogen	21	mg/kg (ppm)	O2 & N2 - Combustion	

Sample ID: PS2020-0074X002 **Sample Name:** Ti

Determination	Result	Units	Method Used	Uncertainty
Aluminium (Al)	<0.10	%_m/m	ICP-OES Analysis - FULL Report	
Iron (Fe)	0.12	%_m/m	ICP-OES Analysis - FULL Report	
Titanium (Ti)	99.3	%_m/m	ICP-OES Analysis - FULL Report	
Vanadium (V)	<0.10	%_m/m	ICP-OES Analysis - FULL Report	
Oxygen	165	mg/kg (ppm)	O2 & N2 - Combustion	
Nitrogen	381	mg/kg (ppm)	O2 & N2 - Combustion	

End of Report

Appendix E X-ray Computed Tomography Scanning Results

The XCT scanning results of the Vanadium powder in an epoxy matrix is seen in this section.

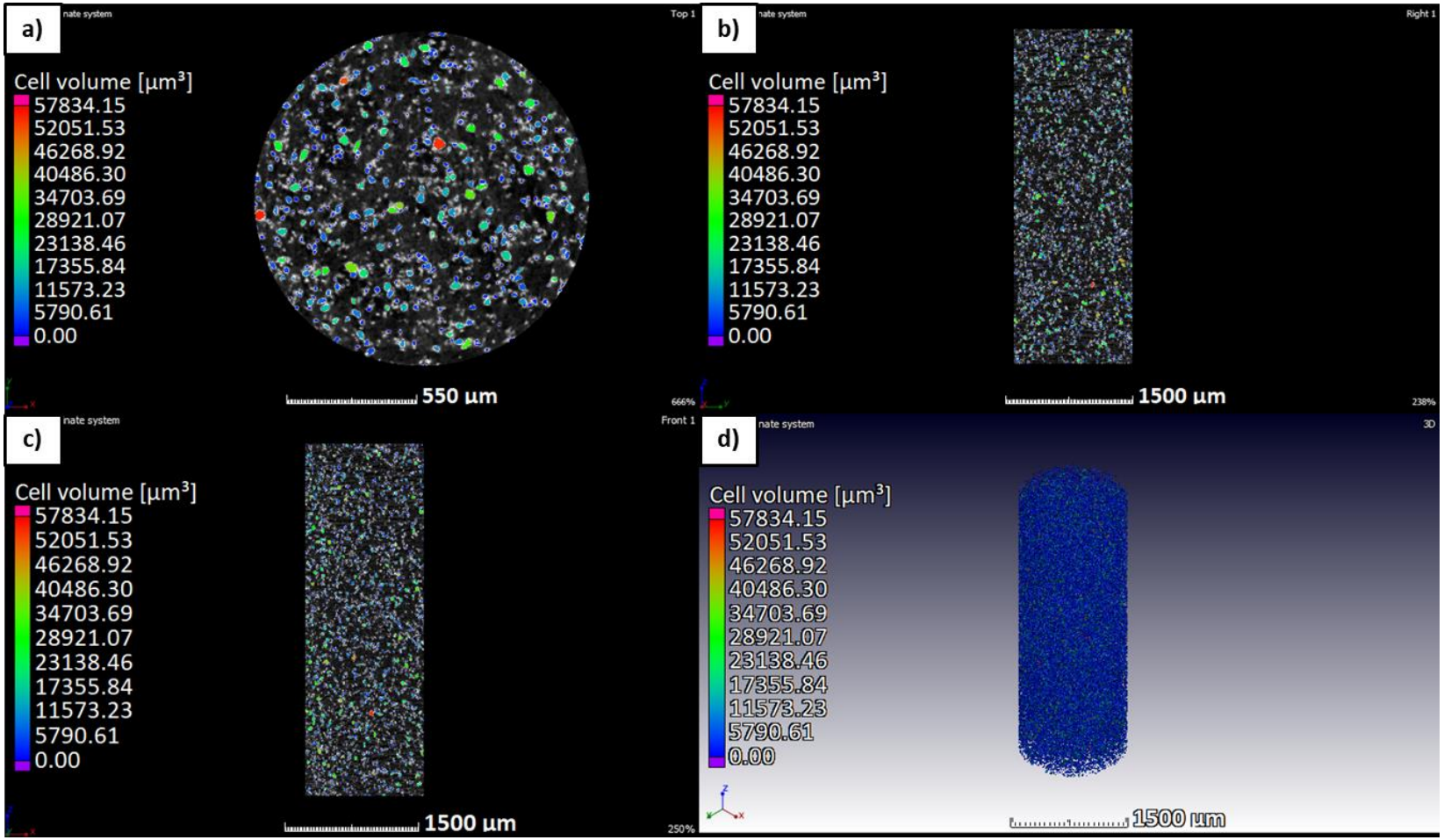

Figure 72: XCT scan images of Vanadium powder in an epoxy matrix according to cell volume with views of a) top, b) right, c) front, and d) 3D Volume

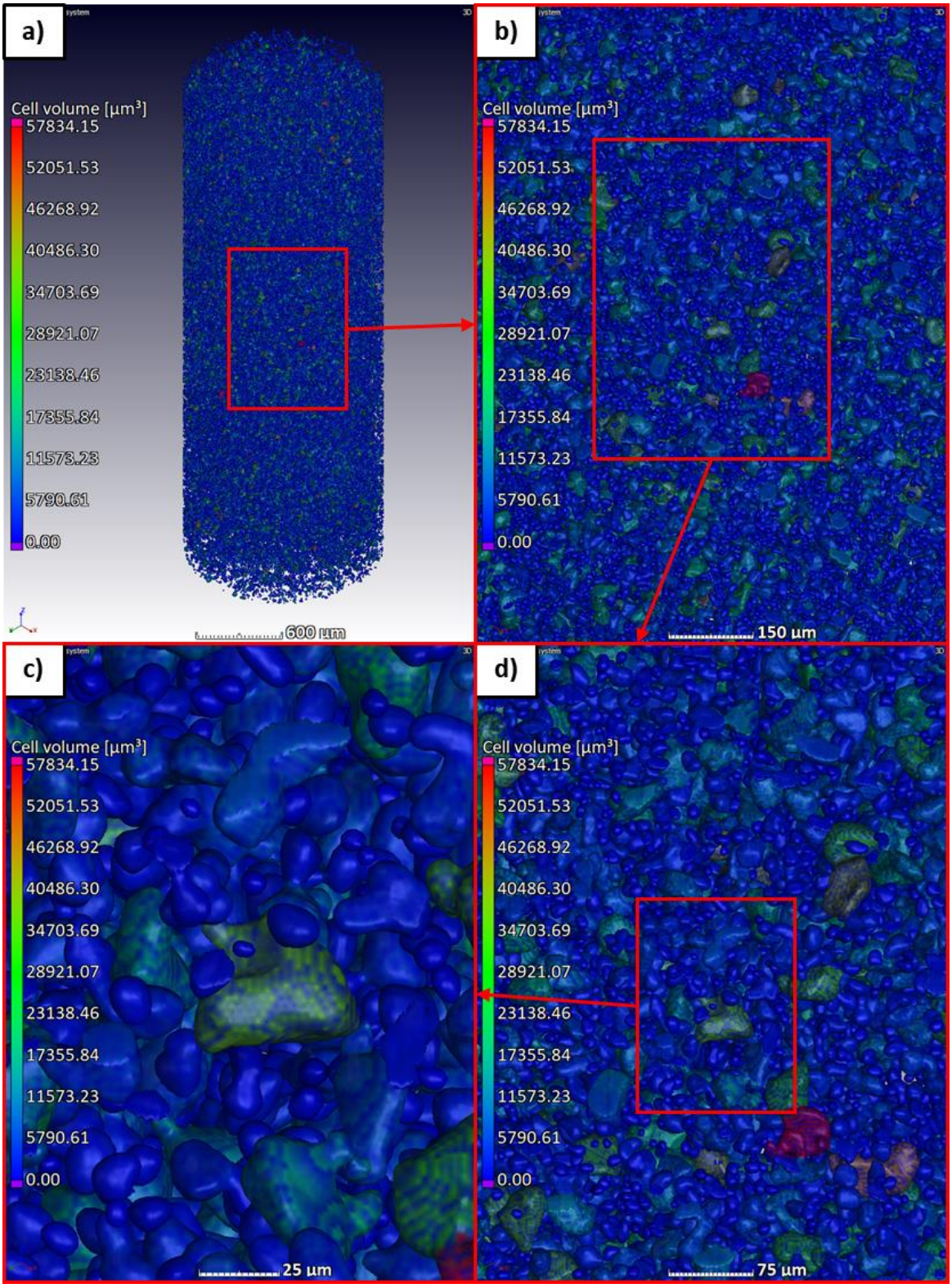

Figure 73: 3D Volume representation of Vanadium powder in an epoxy matrix according to cell volume at various magnifications